



NAVAL POSTGRADUATE SCHOOL

MONTEREY, CALIFORNIA

THESIS

**TEMPORAL AND SPATIAL VARIABILITY OF
BLACK SEA HYDRODYNAMICS AND CHLOROPHYLL:
A CONCENTRATION WITH CONNECTION TO WIND
FORCING**

by

Emre Gulher

March 2013

Thesis Advisor:
Second Reader:

Peter C. Chu
Ming-Jer Huang

Approved for public release; distribution is unlimited

THIS PAGE INTENTIONALLY LEFT BLANK

REPORT DOCUMENTATION PAGE			<i>Form Approved OMB No. 0704-0188</i>	
Public reporting burden for this collection of information is estimated to average 1 hour per response, including the time for reviewing instruction, searching existing data sources, gathering and maintaining the data needed, and completing and reviewing the collection of information. Send comments regarding this burden estimate or any other aspect of this collection of information, including suggestions for reducing this burden, to Washington headquarters Services, Directorate for Information Operations and Reports, 1215 Jefferson Davis Highway, Suite 1204, Arlington, VA 22202-4302, and to the Office of Management and Budget, Paperwork Reduction Project (0704-0188) Washington DC 20503.				
1. AGENCY USE ONLY (Leave blank)		2. REPORT DATE March 2013	3. REPORT TYPE AND DATES COVERED Master's Thesis	
4. TITLE AND SUBTITLE TEMPORAL AND SPATIAL VARIABILITY OF BLACK SEA HYDRODYNAMICS AND CHLOROPHYLL: A CONCENTRATION WITH CONNECTION TO WIND FORCING			5. FUNDING NUMBERS	
6. AUTHOR(S) Emre Gulher				
7. PERFORMING ORGANIZATION NAME(S) AND ADDRESS(ES) Naval Postgraduate School Monterey, CA 93943-5000			8. PERFORMING ORGANIZATION REPORT NUMBER	
9. SPONSORING /MONITORING AGENCY NAME(S) AND ADDRESS(ES) N/A			10. SPONSORING/MONITORING AGENCY REPORT NUMBER	
11. SUPPLEMENTARY NOTES The views expressed in this thesis are those of the author and do not reflect the official policy or position of the Department of Defense or the U.S. Government. IRB Protocol number ____ N/A ____.				
12a. DISTRIBUTION / AVAILABILITY STATEMENT Approved for public release; distribution is unlimited			12b. DISTRIBUTION CODE	
13. ABSTRACT (maximum 200 words) Spatial and temporal variability of the Black Sea surface circulation with the link to chlorophyll-a concentration and surface winds is investigated using Satellite data from Archiving, Validation, and Interpretation of Satellite Oceanographic data (AVISO), Sea-viewing Wide Field-of-view Sensor (SeaWiFS), and Quick Scatterometer (QuikSCAT) with the Self-Organizing Maps (SOMs). Six spatial patterns with temporal variability were identified for the surface currents: Pattern-1 (Sevastopol Cyclonic and Batumi Dipole Eddies, 21%), Pattern-2 (Cyclonic RIM Current and Anti-cyclonic Batumi Eddy, 16%), Pattern-3 (Anti-cyclonic Sevastopol and Batumi Eddies, 17%), Pattern-4 (Cyclonic RIM Current and Cyclonic Batumi Eddy, 21%), Pattern-5 (Anti-cyclonic RIM Current and Batumi Dipole Eddies, 15%), Pattern-6 (Anti-cyclonic RIM Current and Multi Eddies, 10%). It is found the change of the bi-modal characteristics in 2000-2009 with the fall bloom being more significant than the spring bloom. The surface circulation Pattern-4 (cyclonic RIM current and Batumi eddy) is associated with the occurrence of the fall bloom. Evident connection of negative NAO and negative ENSO to the Pattern-4 circulation implies the large-scale atmospheric effect. Possible connection of these patterns to the climatological indices, such as the North Atlantic Oscillation (NAO) and the East Atlantic/West Russian (EAWR), oscillation are also discussed.				
14. SUBJECT TERMS The Self -Organizing Map (SOM); Archiving, Validation and Interpretation of Satellite Oceanographic data (AVISO); Quick Scatterometer (QuikSCAT); Sea-Viewing Wide Field-of-View Sensor (SeaWiFS); North Atlantic Oscillation (NAO); East Atlantic/West Russian (EAWR).			15. NUMBER OF PAGES 161	
			16. PRICE CODE	
17. SECURITY CLASSIFICATION OF REPORT Unclassified	18. SECURITY CLASSIFICATION OF THIS PAGE Unclassified	19. SECURITY CLASSIFICATION OF ABSTRACT Unclassified	20. LIMITATION OF ABSTRACT UU	

THIS PAGE INTENTIONALLY LEFT BLANK

Approved for public release; distribution is unlimited

**TEMPORAL AND SPATIAL VARIABILITY OF
BLACK SEA HYDRODYNAMICS AND CHLOROPHYLL: A
CONCENTRATION WITH CONNECTION TO WIND FORCING**

Emre Gulher
Lieutenant Junior Grade, Turkish Navy
B.S., Turkish Naval Academy, 2006

Submitted in partial fulfillment of the
requirements for the degree of

**MASTER OF SCIENCE IN METEOROLOGY AND PHYSICAL
OCEANOGRAPHY**

from the

**NAVAL POSTGRADUATE SCHOOL
March 2013**

Author: Emre Gulher

Approved by: Peter C. Chu
Thesis Advisor

Ming-Jer Huang
Second Reader

Peter C. Chu
Chair, Department of Oceanography

THIS PAGE INTENTIONALLY LEFT BLANK

ABSTRACT

Spatial and temporal variability of the Black Sea surface circulation with the link to chlorophyll-a concentration and surface winds is investigated using Satellite data from Archiving, Validation, and Interpretation of Satellite Oceanographic data (AVISO), Sea-viewing Wide Field-of-view Sensor (SeaWiFS), and Quick Scatterometer (QuikSCAT) with the Self-Organizing Maps (SOMs). Six spatial patterns with temporal variability were identified for the surface currents: Pattern-1 (Sevastopol Cyclonic and Batumi Dipole Eddies, 21%), Pattern-2 (Cyclonic RIM Current and Anti-cyclonic Batumi Eddy, 16%), Pattern-3 (Anti-cyclonic Sevastopol and Batumi Eddies, 17%), Pattern-4 (Cyclonic RIM Current and Cyclonic Batumi Eddy, 21%), Pattern-5 (Anti-cyclonic RIM Current and Batumi Dipole Eddies, 15%), Pattern-6 (Anti-cyclonic RIM Current and Multi Eddies, 10%). It is found the change of the bi-modal characteristics in 2000-2009 with the fall bloom being more significant than the spring bloom. The surface circulation Pattern-4 (cyclonic RIM current and Batumi eddy) is associated with the occurrence of the fall bloom. Evident connection of negative NAO and negative ENSO to the Pattern-4 circulation implies the large-scale atmospheric effect. Possible connection of these patterns to the climatological indices, such as the North Atlantic Oscillation (NAO) and the East Atlantic/West Russian (EAWR), oscillation are also discussed.

THIS PAGE INTENTIONALLY LEFT BLANK

TABLE OF CONTENTS

I.	INTRODUCTION.....	1
A.	THE BLACK SEA	1
B.	OBJECTIVE	4
C.	SELF-ORGANIZING MAP	4
D.	THESIS ORGANIZATION.....	6
II.	THE DYNAMICS OF THE BLACK SEA	9
A.	INTRODUCTION.....	9
B.	SURFACE CURRENTS.....	9
C.	WIND FIELD	13
1.	BORA WINDS	14
2.	KATABATIC WINDS.....	15
3.	FOEHN WINDS.....	16
D.	TEMPERATURE AND SALINITY	19
E.	CHLOROPHYLL-A.....	24
III.	DATA SOURCES	31
A.	AVISO.....	31
1.	ALTIMETRY	31
a.	<i>History</i>	<i>31</i>
b.	<i>Principle</i>	<i>33</i>
c.	<i>Multi-Satellites</i>	<i>34</i>
2.	MISSIONS	35
3.	DATA	38
B.	SEAWIFS.....	39
1.	OBJECTIVES	40
2.	ORGANIZATION	41
3.	DATA COLLECTION	42
4.	SPACECRAFT AND SENSOR.....	43
C.	QUIKSCAT	45
1.	SCATTEROMETRY.....	45
a.	<i>Introduction.....</i>	<i>45</i>
b.	<i>History</i>	<i>46</i>
2.	MISSION	47
IV.	METHODOLOGY	51
A.	INTRODUCTION TO NEURAL NETWORKS	51
B.	THE SELF-ORGANIZING MAPS.....	53
1.	INTRODUCTION.....	53
2.	STRUCTURE.....	54
3.	ALGORITHM.....	55
4.	DAVIES – BOULDIN INDEX.....	61
5.	TOOLBOX FOR MATLAB	62
C.	COMPARISON WITH OTHER CONVENTIONAL METHODS	63

V.	SURFACE CURRENTS.....	65
A.	MONTHLY MEAN SURFACE CURRENTS	65
B.	TEMPORAL AND SPATIAL VARIABILITY	74
1.	SIX PATTERNS.....	74
a.	<i>Pattern 1: Sevastopol Cyclonic and Batumi Dipole Eddies...</i>	74
b.	<i>Pattern 2: Cyclonic RIM Current and Anti-cyclonic Batumi Eddy.....</i>	76
c.	<i>Pattern 3: Anti-cyclonic Sevastopol and Batumi Eddies.....</i>	76
d.	<i>Pattern 4: Cyclonic RIM Current and Batumi Eddy.....</i>	76
e.	<i>Pattern 5: Anti-cyclonic RIM Current and Batumi Dipole Eddies</i>	76
a.	<i>Pattern 6: Anti-cyclonic RIM Current and Multi Eddies.....</i>	78
2.	VORTICITY FEATURES	79
3.	TEMPORAL VARIATION	80
VI.	SURFACE WINDS	87
A.	MONTHLY MEAN WINDS.....	87
B.	TEMPORAL AND SPATIAL VARIABILITY	95
1.	SIX PATTERNS.....	96
a.	<i>Pattern 1: The Northerly Winds and the Cyclonic Curve in the Western Shelf.....</i>	96
b.	<i>Pattern 2: The Easterly Winds and the Anti-cyclonic Curve in the Western Shelf.....</i>	96
c.	<i>Pattern 3: The Dominance of the Strong Northerly Winds ..</i>	96
d.	<i>Pattern 4: The Northwesterly Winds in the West and the Westerly Winds in the East.....</i>	98
e.	<i>Pattern 5: The Dominance of the Strong Northeasterly Winds</i>	98
f.	<i>Pattern 6: The Strong Southwesterly Winds.....</i>	100
2.	TEMPORAL VARIATION	100
VII.	CHLOROPHYLL	109
VIII.	CONCLUSIONS	123
	LIST OF REFERENCES.....	129
	INITIAL DISTRIBUTION LIST	137

LIST OF FIGURES

Figure 1.	The Black Sea and the surrounding countries (Map available from Geography.Org, http://world-geography.org/sea/92-black-sea.html).....	1
Figure 2.	The map showing the current situation in Moldova (Transnistria) conflict (From <i>Wikimedia Commons</i>)	2
Figure 3.	An illustration showing the options for the South Stream pipeline route (From Gazprom)	3
Figure 4.	The schematic pattern of the Black Sea (From Korotaev et al. 2003)	10
Figure 5.	Illustration of the temporal variability of the wind stress from the 5-minute-resolution Black Sea Modular Ocean Model (MOM) (Stanev et al. 2003), along with the matching curve calculated from the European Centre for Medium-Range Weather Forecasts (ECMWF)-reanalyzed data (From Stanev 2005).	13
Figure 6.	A satellite image demonstrating a Bora event taking place over the east coast of the Black Sea on December 15, 2008 at 19:10 UTC (From ESA).....	15
Figure 7.	A satellite image demonstrating the sea surface signatures of a Katabatic wind event taking place over the east coast of the Black Sea on April 30, 2008 at 19:07 UTC (From ESA).....	16
Figure 8.	A satellite image demonstrating the sea surface signatures of a Foehn wind event taking place over the southeast coast of the Black Sea on January 11, 2010 at 07:31 UTC (From ESA).....	17
Figure 9.	Monthly averaged climatological wind fields. The arrow scale equals 1 m/s. (From Peneva and Stips 2004)	18
Figure 10.	Monthly averaged mixed-layer temperature of the Black Sea obtained through the climatological run of General Estuarine Transport Model (GETM) (From Peneva and Stips 2004).....	21
Figure 11.	Monthly averaged mixed-layer salinity of the Black Sea obtained through the climatological run of General Estuarine Transport Model (GETM) (From Peneva and Stips 2004).....	22
Figure 12.	Illustration of the temporal variability of the thermal buoyancy flux from the 5-minute-resolution Black Sea Modular Ocean Model (MOM) (Stanev et al. 2003), along with the matching curve calculated from the European Centre for Medium-Range Weather Forecasts (ECMWF)-reanalyzed data (From Stanev 2005).	23
Figure 13.	Illustration of the temporal variability of the haline buoyancy flux from the 5-minute-resolution Black Sea Modular Ocean Model (MOM) (From Stanev 2005).	23
Figure 14.	The average monthly distributions of chlorophyll-a (mg/m^3) found in the CZCS data for the first 6-month period (From Kopelevich et al. 2002).....	26
Figure 15.	The average monthly distributions of chlorophyll-a (mg/m^3) found in the CZCS data for the second 6-month period (From Kopelevich et al. 2002)....	27
Figure 16.	A Topex/Poseidon cycle compared to 100 years of in situ data (From http://www.aviso.oceanobs.com/en/altimetry/history.html)	32

Figure 17.	The concepts and systems that contribute to the altimetry measurement (From Cnes)	34
Figure 18.	Comparison of the details of images collected from a single satellite and multi-satellites (From CLS/Cnes)	34
Figure 19.	Altimetry measurement accuracy evolution since the first mission (From Cnes)	36
Figure 20.	An example of the images collected by SeaWiFS Project (From NASA/GSFC)	39
Figure 21.	A photograph of the scanner assembly used in SeaWiFS (From http://oceancolor.gsfc.nasa.gov/seawifs/background/figures/brochure_fig1.gif)	40
Figure 22.	Major elements of SeaWiFS Project (From http://oceancolor.gsfc.nasa.gov/seawifs/background/figures/brochure_fig3.gif) 41	
Figure 23.	Launch diagram of SeaWiFS (From http://oceancolor.gsfc.nasa.gov/seawifs/seastar/seawifs_launch_diagram.jpeg) 44	
Figure 24.	Principle of Scatterometer (From NOAA)	45
Figure 25.	Hurricane Dora viewed from QuikSCAT (From JPL/NASA)	48
Figure 26.	Illustration of the structure of a SOM (From Maung 2012)	54
Figure 27.	A two-dimensional illustration that shows the same type of connection of each node with the input vectors. Note that there is no connection among the nodes (Available from http://www.saedsayad.com/clustering_som.htm)	56
Figure 28.	An illustration that shows the initialization step of each node's weights (From http://www.saedsayad.com/clustering_som.htm)	56
Figure 29.	An illustration of the process utilized by Equation 2a (From Guthikonda 2005)	58
Figure 30.	An illustration of the process of updating BMU along with its neighbors towards the "x," which in this case is the input sample (From Vesanto et al. 2000)	59
Figure 31.	An illustration of the differences among the four neighborhood functions. They are, from left to right, "bubble," "gaussian," "cutgass," and "ep." The first row is a one-dimensional representation, whereas the second row is two-dimensional (From Vesanto et al. 2000)	60
Figure 32.	An illustration of the differences among the three functions of learning rate. <i>inv</i> is represented as a dashed curve, <i>power</i> is represented as a dot-dashed curve, and <i>linear</i> is represented as solid line (From Vesanto et al. 2000).	61
Figure 33.	An illustration of the table format of the data (From Vesanto et al. 2000)	62
Figure 34.	The climatological average of the surface currents for January	66
Figure 35.	The climatological average of the surface currents for February	66
Figure 36.	The climatological average of the surface currents for March	68
Figure 37.	The climatological average of the surface currents for April	69
Figure 38.	The climatological average of the surface currents for May	69

Figure 39.	The climatological average of the surface currents for June	70
Figure 40.	The climatological average of the surface currents for July	70
Figure 41.	The climatological average of the surface currents for August	71
Figure 42.	The climatological average of the surface currents for September.....	71
Figure 43.	The climatological average of the surface currents for October.....	72
Figure 44.	The climatological average of the surface currents for November.....	72
Figure 45.	The climatological average of the surface currents for December	73
Figure 46.	The Davies-Bouldin index results concerning the geostrophic velocity data set	74
Figure 47.	The first pattern of the surface currents and its percentage	75
Figure 48.	The second pattern of the surface currents and its percentage.....	75
Figure 49.	The third pattern of the surface currents and its percentage	77
Figure 50.	The fourth pattern of the surface currents and its percentage.....	77
Figure 51.	The fifth pattern of the surface currents and its percentage.....	78
Figure 52.	The sixth pattern of the surface currents and its percentage.....	79
Figure 53.	Horizontally averaged East and West (a) relative vorticity, and (b) enstrophy anomaly values of the six patterns of the surface currents.....	80
Figure 54.	Monthly percentage of the six patterns of the surface currents	81
Figure 55.	The inter-annual variability of the six patterns of the surface currents	83
Figure 56.	Evolution of the duration and the frequency of the six patterns of the surface currents shown in Figures 47 - 52. For instance, the SOM Pattern 2 lasted for approximately 3 months and dominated the period between 2002 and 2003 when no other patterns occurred.	83
Figure 57.	Comparison between the inter-annual variability of the six patterns of the surface currents and the EAWR index.....	84
Figure 58.	Comparison between the inter-annual variability of the six patterns of the surface currents and the NAO index	84
Figure 59.	Comparison between the inter-annual variability of the six patterns of the surface currents and the ENSO index	85
Figure 60.	Distribution for each pattern of the surface currents between positive (red) and negative (blue) phases of the teleconnection indices. The areas with darker colors represent the strong phases for which the index's absolute value is greater than a standard deviation. Monthly average values of the climate are obtained through the NOAA Climate Prediction Center (Available at http://www.cpc.ncep.noaa.gov/data/teledoc/telecontents.shtml).	86
Figure 61.	The climatological average of the winds for January	88
Figure 62.	The climatological average of the winds for February	89
Figure 63.	The climatological average of the winds for March	89
Figure 64.	The climatological average of the winds for April	90
Figure 65.	The climatological average of the winds for May	91
Figure 66.	The climatological average of the winds for June	92
Figure 67.	The climatological average of the winds for July	92
Figure 68.	The climatological average of the winds for August.....	93
Figure 69.	The climatological average of the winds for September	93

Figure 70.	The climatological average of the winds for October.....	94
Figure 71.	The climatological average of the winds for November.....	94
Figure 72.	The climatological average of the winds for December	95
Figure 73.	The Davies-Bouldin index results concerning the wind data set.....	95
Figure 74.	The first pattern of the winds and its percentage	97
Figure 75.	The second pattern of the winds and its percentage	97
Figure 76.	The third pattern of the winds and its percentage	98
Figure 77.	The fourth pattern of the winds and its percentage.....	99
Figure 78.	The fifth pattern of the winds and its percentage.....	99
Figure 79.	The sixth pattern of the winds and its percentage.....	100
Figure 80.	Monthly percentage of the six wind patterns.....	102
Figure 81.	The inter-annual variability of the six wind patterns	103
Figure 82.	Evolution of the duration and the frequency of the six patterns of the winds shown in Figures 74-79. For instance, the SOM Pattern 3 lasted more than 6 months and dominated approximately 2 months between years 2008 and 2009 with more than 50%.....	103
Figure 83.	Comparison between the inter-annual variability of the six wind patterns and the EAWR index	104
Figure 84.	Comparison between the inter-annual variability of the six wind patterns and the NAO index	104
Figure 85.	Comparison between the inter-annual variability of the six wind patterns and the ENSO index.....	105
Figure 86.	Monthly anomalies of the components of zonal and meridional winds. The six wind patterns provided by the SOM analysis are distinguished by the large circles. The smaller circles, on the other hand, depict the basin scale averages for all the months from January 2000 to January 2009.	106
Figure 87.	Distribution for each pattern of the surface currents between positive (red) and negative (blue) phases of the teleconnection indices. The areas with darker colors represent the strong phases for which the index's absolute value is greater than a standard deviation. Monthly average values of the climate are obtained through the NOAA Climate Prediction Center (Available at http://www.cpc.ncep.noaa.gov/data/teledoc/telecontents.shtml).	107
Figure 88.	The climatological average of the chlorophyll-a concentration for January .	110
Figure 89.	The climatological average of the chlorophyll-a concentration for February	111
Figure 90.	The climatological average of the chlorophyll-a concentration for March ...	111
Figure 91.	The climatological average of the chlorophyll-a concentration for April	112
Figure 92.	The climatological average of the chlorophyll-a concentration for May	112
Figure 93.	The climatological average of the chlorophyll-a concentration for June	113
Figure 94.	The climatological average of the chlorophyll-a concentration for July	113
Figure 95.	The climatological average of the chlorophyll-a concentration for August ..	114
Figure 96.	The climatological average of the chlorophyll-a concentration for September	114
Figure 97.	The climatological average of the chlorophyll-a concentration for October.	115

Figure 98.	The climatological average of the chlorophyll-a concentration for November.....	115
Figure 99.	The climatological average of the chlorophyll-a concentration for December	116
Figure 100.	The climatological average of the chlorophyll-a concentration from 2000 to 2009	116
Figure 101.	(a) Horizontally averaged East and West relative vorticities, with (b) chlorophyll-a concentration superimposed. Small circles represent the monthly anomalies of the basin scale averaged zonal component of the vorticity of the surface currents from 2000 to 2009. Larger circles indicate the recurrent spatial patterns identified by the SOM analysis that are illustrated in Figures 46 – 51. The basin average chlorophyll-a anomaly is superimposed.	118
Figure 102.	Temporal evolution of the chlorophyll-a concentrations from 1999 – 2009. In order to assess the correlation with the surface currents, the bars represent the contribution of the recurrent patterns for each three-month period.	118
Figure 103.	In the right panel, small circles represent the monthly anomalies of the basin scale averaged meridional and zonal components of the winds from 2000 to 2009. Larger circles indicate the recurrent spatial patterns identified by the SOM analysis that are illustrated in Figures 74 – 79. The basin average chlorophyll anomaly is superimposed.....	119
Figure 104.	Temporal evolution of the chlorophyll-a concentrations from 1999 – 2009. In order to assess the correlation with the surface winds, the bars represent the contribution of the recurrent patterns for each three-month period.	120
Figure 105.	Sensitivity of the temporal interruption on chlorophyll-a concentration using (1) all data, (2) all data except April, and (3) all data except August (from Chu et al. 2005).....	121
Figure 106.	Distribution of observational stations: (a) winter, (b) spring, (c) summer, and (d) fall (from Chu et al. 2005).	121

THIS PAGE INTENTIONALLY LEFT BLANK

LIST OF TABLES

Table 1.	A few examples of the SOM applications in oceanography (From Liu and Weisberg 2011).....	6
Table 2.	Specifications of the Satellites Used in the Past Missions of AVISO	35
Table 3.	Specifications of the Satellites being Used in the Current Missions of AVISO	36
Table 4.	Specifications of the Satellites Planned to be Used in the Future Missions of AVISO	37
Table 5.	Mission Characteristics of SeaWiFS	44
Table 6.	Mission Partners of QuikSCAT	49
Table 7.	Main six steps of the algorithm of the SOM.....	55
Table 8.	The percentages of the six patterns of the surface currents with respect to the large-scale teleconnection indices. For example, when the ENSO index is positive, Pattern 2 has the highest possibility to form among the six patterns at 25%. Yet, when the ENSO index is negative, pattern 6 has the smallest possibility of occurring at only 8%.....	85
Table 9.	The percentages of the six wind patterns with respect to the large-scale phenomena. For example, when the NAO index is positive, Pattern 3 has the highest possibility to form among the six patterns at 32%. On the other hand, when the EAWR index is positive, Pattern 2 has the smallest possibility of occurring at 7%.....	105
Table 10.	The percentages of the six wind patterns with respect to the six patterns of the surface currents. For example, when Pattern 3 of the winds occurs, Pattern 2 of the surface currents has the highest possibility to form at 5.54%. On the other hand, when Pattern 1 of the winds occurs, Pattern 4 has the smallest possibility of occurring at 0.43%.....	106
Table 11.	Distribution of the occurrence rates of the surface current patterns with respect to the spring and fall blooms of the chlorophyll-a concentrations	119
Table 12.	Distribution of the occurrence rates of the recurrent patterns with respect to the spring and fall blooms of the chlorophyll-a concentrations.....	120

THIS PAGE INTENTIONALLY LEFT BLANK

LIST OF ACRONYMS AND ABBREVIATIONS

ADCP	Acoustic Doppler Current Profiler
ADEOS	Japanese Advanced Earth Observing Satellite
AVISO	Archiving, Validation, and Interpretation of Satellite Oceanographic data
BMU	Best Matching Unit
CLS	Collecte Localisation Satellites
CNES	Centre National d'Etudes Spatiales
CTDP	Conductivity-Temperature-Depth-Oxygen Profiler
CZCS	Coastal Zone Color Scanner
DAAC	Distributed Active Archive Center
DBI	The Davies–Bouldin Index
DT	Delayed Time
Duacs	Data Unification and Altimeter Combination System
EAWR	East Atlantic/West Russian Oscillation
ECMWF	European Centre for Medium-Range Weather Forecasts
EOF	Empirical Orthogonal Function
EOSDIS	Earth Observing System Data and Information System
ERS-1	European Space Agency's Remote Sensing Satellite
ESA	European Space Agency
EU	European Union
EUMETSAT	European Organisation for the Exploitation of METeorological SATellites
GAC	Global Area Coverage

GDR	Geophysical Data Record
GETM	General Estuarine Transport Model
GSFC	Goddard Space Flight Center
GPS	Global Positioning System
HRPT	High-Resolution Picture Transmission
IGDR	Interim Geophysical Data Record
ISRO	Indian Space Research Organization
JPL	Jet Propulsion Laboratory
LAC	Local Area Coverage
MOM	Modular Ocean Model
NAO	North Atlantic Oscillation
NASA	National Aeronautics and Space Administration
NATO	North Atlantic Treaty Organization
NOAA	National Oceanic and Atmospheric Administration
NSCAT	The NASA Scatterometer
NRT	Near Real Time
OSCAT	Oceansat-2 scatterometer
OSD	Optimal spectral decomposition
OV-2	OrbView-2
Po-Daac	Physical Oceanography – Distributed Active Archive Center
PCA	Principal Component Analysis
PDT	Pacific Daylight Time
QuikSCAT	Quick Scatterometer
Ref	Reference

RT	Real Time
SDPS	SeaWiFS Data Processing System
SeaWiFS	Sea-viewing Wide Field-of-view Sensor
SLA	Sea Level Anomaly
SOM	Self – Organizing Map
SPO	SeaWiFS Project Office
SSAS	Seasat-A Satellite Scatterometer
Ssalto	Segment Sol multimissions d'ALTimétrie, d'Orbitographie et de localisation précise
T/P	Topex/Poseidon
Upd	Updated
WFF	WallopsFlight Facility
XOR	Exclusive-or

THIS PAGE INTENTIONALLY LEFT BLANK

ACKNOWLEDGMENTS

I would like to offer my sincere gratitude to my advisor, Distinguished Professor Peter C. Chu, for his encouragement, scientific guidance, and instructions throughout the course of the research. This thesis process wouldn't have been this educational and exciting without his wealth of knowledge and motivation. I want to express my heartfelt appreciation to my second reader Doctor Ming-Jer Huang for his support and sharing his expertise unconditionally.

I would like to acknowledge Mr. Chenwu Fan and Mr. Michael Cook. Your abilities and patience to push me through MATLAB programming made it possible for me to finish my analyses on time and precisely. It was my honor getting to know you both.

I also would like to recognize and express my appreciation for the financial and informative support of the Turkish Navy.

My parents, Fethiye and Ali Cengiz Gulher, have always believed in me and have always been my greatest supporters. Thank you both from the bottom of my heart.

Words do not even do justice for the devotion and love of my wife throughout the time I have spent at NPS. Her patience and encouragement have enabled this thesis. I am so blessed to have her in my life.

This thesis is dedicated to my beloved wife, Mehtap Gulher, and my little angel, Defne Lora Gulher.

THIS PAGE INTENTIONALLY LEFT BLANK

I. INTRODUCTION

A. THE BLACK SEA

The Black Sea is located between Asia Minor and southeastern Europe. It is connected to the Mediterranean Sea through the Bosphorus, the Sea of Marmara, the Dardanelles and the Aegean Sea. If the Sea of Azov is left out, the Black Sea covers approximately 436,400 km². The Black Sea has been pursuing its crucial importance to commerce in the region for ages (<http://www.ceoe.udel.edu/blacksea/geography/index.html>).

Six countries neighbor the main inland sea. Namely: Romania and Bulgaria at the west coast; Ukraine and Russia at the north coast; Georgia at the east coast; and finally Turkey at the south coast. Apart from these neighboring countries, there are 10 other nations that affect the region by the five major rivers, those empty into the Black Sea. The largest one among these five rivers is the Danube River (<http://www.ceoe.udel.edu/blacksea/geography/index.html>).



Figure 1. The Black Sea and the surrounding countries
(Map available from Geography.Org, <http://world-geography.org/sea/92-black-sea.html>)

The strategic importance of the Black Sea region has been increasing significantly, especially since the memberships of Bulgaria and Romania were granted for North Atlantic Treaty Organization (NATO) in 2004, and shortly after for the European Union (EU) in 2007. Due to the fact that The Black Sea became the border region of both NATO and the EU, any issues affecting the geo-economic, geo-political or the geo-strategic status of the region draw attention of both establishments effectively. Examples of the current geo-political and geo-strategic issues are: the frozen conflicts of Moldova (Transnistria) and Georgia (Abkhazia-South Ossetia), both of which are fundamentally based on the ethnicity diversity; Armenia-Azerbaijan (Nagorno-Karabakh) which arose as a result of the tortious occupancy of Azerbaijan soil by the Armenian forces; the resurgence of Russia; organized criminal activity and transnational terrorism (J. Bosbotinis 2013, unpublished manuscript). Therefore, it is clear that expansion of the borders of both NATO and EU confronts both communities with the problems and weaknesses of the Black Sea area as well as its benefits, and challenges the Euro-Atlantic goals in terms of keeping the continent secure, free and wealthy (Ulger 2007).



Figure 2. The map showing the current situation in Moldova (Transnistria) conflict
(From *Wikimedia Commons*)

The geo-economic importance of the Black Sea is expected to rise as oil and gas pipelines from Azerbaijan and Russia centers in the region. Its importance may be even more pronounced, if these resources are integrated with a Pan-European transport system. The increasing trend of the gas demand is expected to continue in the following years. Especially, the estimate of the gas consumption in Europe is at least 600 billion cubic meters after 2020, while domestic production will drop down to half. Therefore, South Stream is determined as a feasible project that will help European countries to overcome the crisis of the lack of energy sources in the horizon, and at the same time it will conserve the energy security (<http://www.gazprom.com/press/news/2010/november/article106074/>). Furthermore, the Black Sea region neighbors Caspian Basin, which is an extremely important region due to its hydrocarbon resources. This proximity increases strategic importance of the Black Sea as the energy security becomes the focus of both NATO and the EU (J. Bosbotinis 2013, unpublished manuscript).



Figure 3. An illustration showing the options for the South Stream pipeline route (From Gazprom)

Russia is the other actor in the same sense, and tries to maintain its dominance in the wider Eurasian post-Soviet space and monopolistic status in terms of energy exports. Russia also pays extreme attention to the region and its issues. Namely: the futures of the North-South Caucasus and Ukraine; expanding borders of NATO and the EU; the increasing trend of US presence. As a result of the common interests in the Black Sea, the region evolves into a core area where a competition between U.S. and Russia takes place. Both actors try to take advantage of the Black Sea and its surrounding by treating it as a gateway to extend their influence; particularly Middle East, Central Asia and South Caucasus areas are of interest for the US; whereas, Mediterranean in addition to these regions for Russia (J. Bosbotinis 2013, unpublished manuscript).

B. OBJECTIVE

The new militarily, politic and economic developments in the Black Sea propels the need of a deeper understanding the nature and the mechanisms of the basin. Hence, the spatial and temporal variation of the Black Sea holds a crucial importance, especially with regard to operational purposes. The main focus of this research is to obtain data sets concerning the three features of the Black Sea (geostrophic velocity anomalies, geostrophic winds, and chlorophyll-a concentration) through various systems, and to analyze them to extract this spatial and temporal variation. To identify a correlation among these patterns of separate data sets and to evidence that one pattern of a data set can affect another from a different data set is intended afterwards. There are number of tools available to achieve this goal. The self-organizing map (SOM) is selected particularly in this study, due to the fact that its accuracy is greatly appreciated and it is not widely used in the Black Sea region.

C. SELF-ORGANIZING MAP

Even though data availability advances steadily, both by in-situ observations and remote-sensing techniques, it doesn't necessarily correspond to the efficient and consistent processing or usage of these data. The estimation is that no more than 5% of the images collected by remote-sensing techniques are either exposed to human eyes or actually processed. Reasons for this may include lack of time or, from a different

perspective, lack of tools that can process a huge amount of data efficiently, while extracting the key features that this thesis is after (Petrou 2004).

The SOM is introduced as an option to abridge this ever widening gap between the available and processed data. SOM (aka, the Kohonen map) is an unsupervised neural network and competitive learning underlies it (Kohonen 1998, 2001). One of the key features of SOM is its capability of preserving the neighborhood relations of the high-dimensional input data while projecting it onto a lower dimensional (preferably two-dimensional) space. Therefore, it is known as a topology-preserving technique. As a result of this topology-preserving technique, patterns that are similar are put into neighboring regions during the mapping process; having these similar patterns closely mapped to one another enables a huge advantage in pattern recognition and the feature extraction processes of the complex data sets. The SOM and its benefits were presented to the oceanography community by Richardson et al. (2003), since then it has been heavily used in miscellaneous projects. Some of these works are listed in Table 1 (Liu and Weisberg 2011).

Table 1. A few examples of the SOM applications in oceanography (From Liu and Weisberg 2011).

Oceanographic data	Regions	References
Oil spill	Galician coast, Europe	Corchado et al. (2008), Mata et al. (2009), Borges et al. (2010)
Maritime data	Europe	Lobo (2009)
Salinity	Columbia River plume	Liu et al. (2009)
Surface winds	Southeast Atlantic	Richardson et al. (2003), Risien et al. (2004)
Satellite measured sea surface height	Southeast Atlantic	Hardman-Mountford et al. (2003)
	Indian Ocean	Iskandar (2009)
	South China Sea	Liu et al. (2008)
Satellite ocean color, chlorophyll	Pacific	Ainsworth (1999), Ainsworth and Jones (1999)
	Southeast Atlantic	Yacoub et al. (2001)
	Southwest Atlantic	Saraceno et al. (2006)
	North Atlantic	Niang et al. (2003), Telszewski et al. (2009)

D. THESIS ORGANIZATION

Chapter II provides a foundation for the Black Sea dynamics. Atmospheric forcing mechanism, surface currents, temperature–salinity properties, and biological environment are touched on.

Chapter III gives information about the data used here in this research, where the data was obtained, how the data was collected, as well as a look at the technology behind the data collection.

Chapter IV details the SOM in terms of foundation. The idea behind this technique, how it works, the mathematics that it is based on, and the toolbox for Matlab will be mentioned briefly.

Chapter V presents the analyses that were applied to the data set of the geostrophic velocity, as well as the results of these analyses. The relation between the geostrophic velocity and the large-scale phenomena are discussed.

Chapter VI presents the analyses and their results regarding the geostrophic wind data set. As in Chapter V, the relation between the geostrophic velocity and the large-scale phenomena are discussed.

Chapter VII focuses on the chlorophyll-a data set and investigates the correlation between chlorophyll-a and geostrophic velocity, chlorophyll-a and geostrophic wind separately.

Chapter VIII, the final chapter, concludes the research by pointing out the findings and manifests any recommendations for further study.

THIS PAGE INTENTIONALLY LEFT BLANK

II. THE DYNAMICS OF THE BLACK SEA

A. INTRODUCTION

The Black Sea is a mid-latitude basin located between 41°N and 46°N . It exchanges water with the Mediterranean Sea through the Strait of Bosphorus. In terms of bathymetry, the Black Sea has a flat abyssal plain at the center, which comprises the maximum depth found (2200 m); and along its coast there is a continental shelf that has various offshore extensions depending on the location. The extension off the western Turkish coast, for instance, is ~ 5 km, whereas it is ~ 200 km off the northwestern coast. The Black Sea is split into two sub-basins by the Crimean Peninsula to the north and the central Turkish coastline to the south. Apart from the Mediterranean Sea, the Black Sea is also fed by large river discharges, specifically by the Danube, the Dnepr, and the Dnestr Rivers which are located on the northwestern shelf. Therefore, the Black Sea houses both the high salinity waters of Mediterranean origin and the low salinity waters of riverine origin. The high salinity waters underlay the low salinity waters. This formation results in a permanent pycnocline, which is formed around 100-150 m beneath the surface and prevents any exchanges between these two waters of different salinity profiles. Deeper waters that are below 500 m are immobile. During the summer time and between 10–40 m, formation of a seasonal thermocline is observed (Oguz et al. 1992).

B. SURFACE CURRENTS

The dominant characteristic of the Black Sea circulation is the basin-wide circulation that is mainly cyclonic. This circulation depends heavily on time and is considered as following the continental slope. This unique characteristic is called the Rim Current and it is 40-80 km wide. It is fundamentally fueled by the mean cyclonic wind pattern in the area and by the intense buoyancy input (Stanev 1990; Oguz et al. 1995; Korotaev et al. 2001). According to the model simulations, apart from the forcing mechanism of the winds, the Rim Current disappears unless the topology data is put into the model (Oguz et al. 1995). Furthermore, if the bottom slope and the course of the coastline are changed along the Turkish and Caucasian coasts, the Rim Current meanders

and features of instability are widely observed, in terms of both time and space (Oguz et al. 1993). Models have also demonstrated that the weakening of the wind stress in the spring and summer results in a drop in the mean current's intensity (Gregoire et al. 2004; Stanev 1990). This drop in the intensity causes intensified meandering of the Rim Current along the Turkish and Caucasian coasts resulting in the creation of large (100-200 km) meanders. The presence of a series of recurrent, near-shore, anti-cyclonic eddies between the Rim Current and the coast, along with a number of cyclonic gyres in the basin's central area, have been confirmed by both satellite data (Oguz et al. 1992; Sur et al. 1994; Stanev et al. 2000; Ginzburg et al. 2000; Korotaev et al. 2001, 2003) and by hydrographic observations (Oguz et al. 1993, 1994; Poulain et al. 2005).

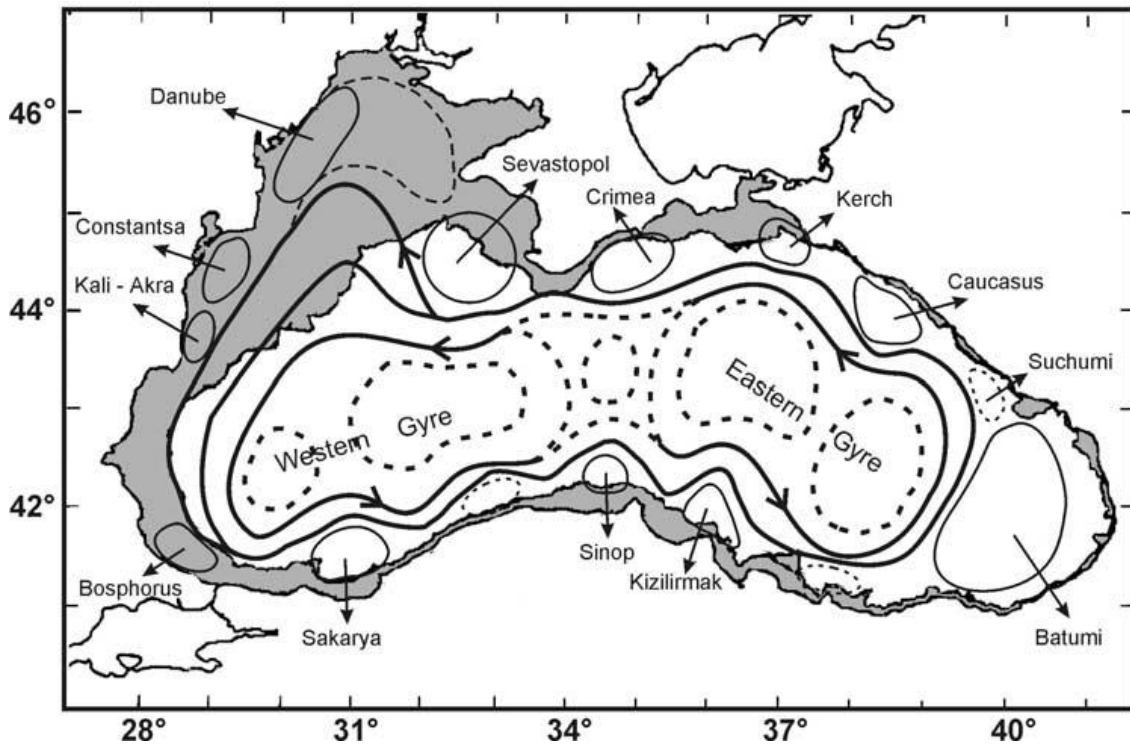


Figure 4. The schematic pattern of the Black Sea (From Korotaev et al. 2003)

Among these near-shore and anti-cyclonic eddies, two persistent eddies are noticeable; namely: the Batumi Eddy and the Sevastopol Eddy. The Batumi Eddy is located off of the southeastern coast and the Sevastopol Eddy is located west of the Crimean Peninsula and over the gentle continental slope. The interior part of the Rim

Current is composed of one of two detached cyclonic gyres. These detached cyclonic gyres consist of either one gyre located in the eastern part of the sea and the other located in the western part of the sea, or a single extended basin-wide cell. At the times it is composed of two separate cyclonic gyres, recurrent mesoscale eddies form in the interior parts of the gyres and they are connected to one another via a recurrent anticyclone known as the Central Basin Eddy (Oguz et al. 1993). The scales of the central gyres and eddies vary from tens to hundreds of kilometers. Additionally, the number, location and morphology of the central gyres and eddies are strongly season-dependent (Poulain et al. 2005). Eddies that vary inter-annually, seasonally, and by mesoscale/synoptic scale, dominate the near-surface circulation of the Black Sea (Oguz et al. 1994; Poulain et al. 2005).

According to Zatsepin et al. (2003), apart from the Rim Current zones and the near-shore, anti-cyclonic eddies also form in the central Black Sea. There is an interaction between these eddies and the Rim Current, which causes mixing of near-shore waters and advection due to reflection from the coast and the two separate jets that it forms. Additionally, there is no correlation between the anticyclones in the eastern part of the central Black Sea that have long life periods and the harshness of the preceding winter. On the other hand, the variability of the wind is a decisive factor affecting the scales of synoptic, seasonal, and inter-annual eddies. Exchanges in the shelf-deep basin of the Black Sea are mainly driven by the eddy dynamics (Zatsepin et al. 2003; Poulain et al. 2005).

The Black Sea eddies are formed in the eastern part of the basin and they propagate to the western part of the basin in the form of Rossby Waves at the speed of $\sim 3\text{cm/s}$. This eddy propagation is strongly affected by the narrow part of the Black Sea located at the south of the Crimean Peninsula (Rachev and Stanev 1997). The more eddies lose their momentum and shrink to smaller scales in the western basin, the more a rise in the dissipation is observed. This process is influenced by topography. Korotaev et al. (2001) examined sea level data that was collected by satellite altimeters and confirmed this westward propagation of phase (Poulain et al. 2005).

Inter-annual variability of the Black Sea circulation is significantly affected by river discharges, local dynamics, and wind forcing's seasonal variability (Stanev et al. 1995; Stanev and Beckers 1999). Mesoscale, seasonal, and inter-annual variability was best described by the observations made by satellite altimeters (Stanev et al. 2000; Korotaev et al. 2001, 2003). According to Stanev et al. (2000), intensification of the general cyclonic circulations occurs in spring and winter, depending on the significant increase in sea level in the near-shore areas. The wind forcing is also pointed out as the major factor that drives the circulation's intensification at the seasonal scale. The Rim Current and large coastal quasi-permanent, anti-cyclonic eddies (the Batumi Eddy, the Sevastopol Eddy, etc.) have the strongest variations at the intra-annual scale. The Batumi Eddy shows clear seasonal variability in terms of circulation such that it demonstrates a pronounced cyclonic circulation during the winter and a weaker cyclonic or an anti-cyclonic circulation during the summer and fall. Unlike the Batumi Eddy case, the variability of the Sevastopol Eddy does not depend on seasons, but rather follows an inter-annual or intra-annual scale (Poulain et al. 2005).

Korotaev et al. (2001) used both TOPEX-POSEIDON and ERS-1 data to explain that, there is a strong variability of the Black Sea circulation due to seasonality. More specifically, the circulation intensifies during the winter and spring, and it weakens during the summer and fall. The period of the most intense mesoscale oscillations is determined to be 120 days. These oscillations are found in the basin's southeastern part. The Rim Current splits and meanders off the Crimean Peninsula in this part of the basin due to the influence of the local bathymetry (Poulain et al. 2005).

The general circulation of the Black Sea is comprised of two-cyclonic gyres during the winter, which convert into a single cell structure which is encompassed by a weaker and wider Rim Current during the summer. The Rim Current demonstrates an intense and complicated mesoscale activity during the summer and fall when the whole circulation structure decomposes into a number of interconnecting eddies (Korotaev et al. 2003; Poulain et al. 2005). The dominance of the anti-cyclonic gyres in the northwestern and southeastern corners of the Black Sea during the summer and fall is confirmed by the model simulations as well. Additionally, the simulations noted that the most pronounced

and persistent coastal anti-cyclonic eddy is the Batumi Eddy, which mostly dominates throughout the period between March and October. These simulations also showed that the conditions during the winter and summer months favor the formation of the Sevastopol Eddy (Poulain et al. 2005).

C. WIND FIELD

The meteorological observations concerning the Black Sea region give clues about the high variability and distinction of the circulation patterns of the atmospheric processes. The main external factor that induces the drift currents is considered as wind stress. Accompanied by coastline, baroclinicity, and bottom relief, wind stress constructs a particular Black Sea circulation under the influence of Earth's rotation (Kordzadze et al. 2007).

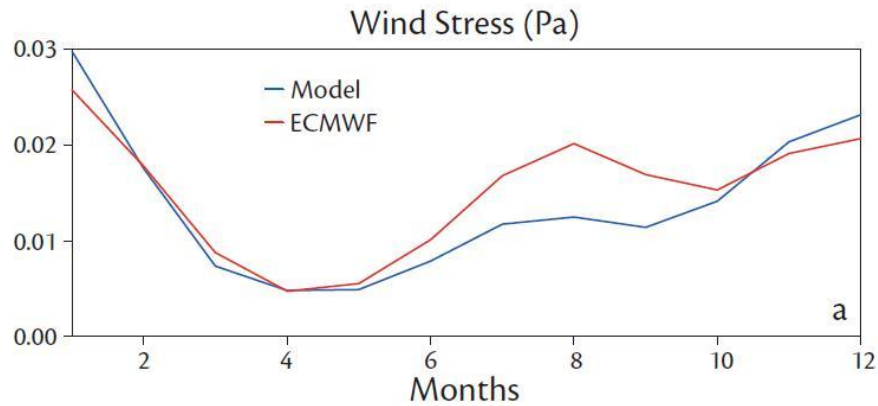


Figure 5. Illustration of the temporal variability of the wind stress from the 5-minute-resolution Black Sea Modular Ocean Model (MOM) (Stanev et al. 2003), along with the matching curve calculated from the European Centre for Medium-Range Weather Forecasts (ECMWF)-reanalyzed data (From Stanev 2005).

Black Sea oceanography aims to investigate the evolution of Black Sea circulation while taking the atmospheric circulation strongly into account. For this purpose, the quantitative circulation aspects of the Black Sea should be put into use as well as the experimental methods (Kordzadze et al. 2007).

The Black Sea's east coast is the region where some notable local wind fields are located due to the coastal mountain range bordering the sea that has irregular height with gaps and valleys. Easterly air flows to the Black Sea through these gaps and valleys. In the Black Sea's southern region, a broad valley called Kolkhida enables this airflow to progress even more westward. The Novorossiyskaya bora, which can exceed the speed of 40 m/s, is the most well-known local east coast wind of the Black Sea (Gusev 1959; Burman 1969; Alpers et al. 2009). This local wind can be very dangerous, particularly for coastal traffic and those participating in harbor activities (Kordzadze et al. 2007).

1. BORA WINDS

When a cold front system passes over a region or when a high pressure gradient occurs and moves the cold air over a coastal mountain range, local down-slope winds are observed and these winds are called Bora winds (Alpers et al. 2010). These winds are found in mountainous coastal regions with heights below 600 m, so that descending cold air warms adiabatically at a relatively small rate. This is the direct opposite condition when compared to Foehn and Chinook winds, where the adiabatic warming rate is notable. These winds are also known as Novorossiyskaya Boras due to the fact that they are mostly observed in the coastal region close to Novorossiysk (Gusev 1959; Burman 1969). At times these winds with notable strength stay over the region for several days, they excite a cyclonic eddy at the southeast of the Tuapse in Russia (Alpers et al. 2010).

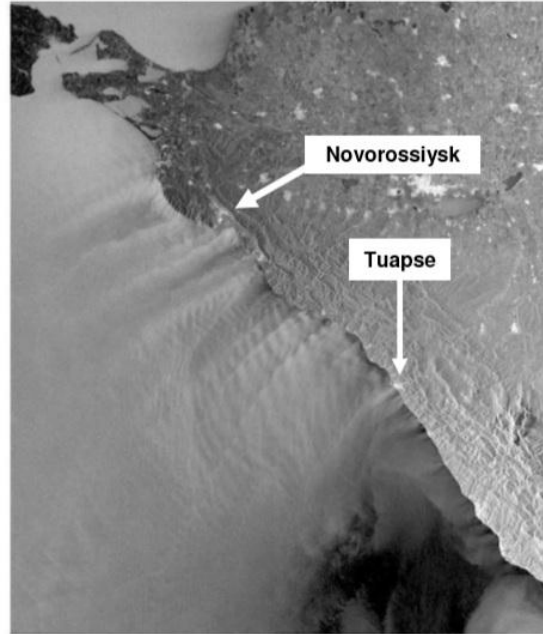


Figure 6. A satellite image demonstrating a Bora event taking place over the east coast of the Black Sea on December 15, 2008 at 19:10 UTC (From ESA)

2. KATABATIC WINDS

Katabatic winds blow following a sloping coastal topography and eventually they reach the surface of the sea. Besides being cold winds, Katabatic winds are observed only in the early morning, in the evening, or at night (Alpers et al. 2010). The inducing mechanism for these types of winds is the cooling rate difference between air near the surface over the land and over the sea. Since air near the surface has a larger cooling rate over the land as opposed to over the sea, the cold air flows downhill. This flow is known as gravity flow. Unless low-level clouds inhibit the cooling process, air is able to cool off notably fast during the evening and night. This fast cooling of the air enables the generation of the Katabatic winds. Since the wind flowing downhill is channeled through coastal valleys, the katabatic winds form a tongue-like shape along the coastline (Alpers et al. 1998; Alpers et al. 2010).

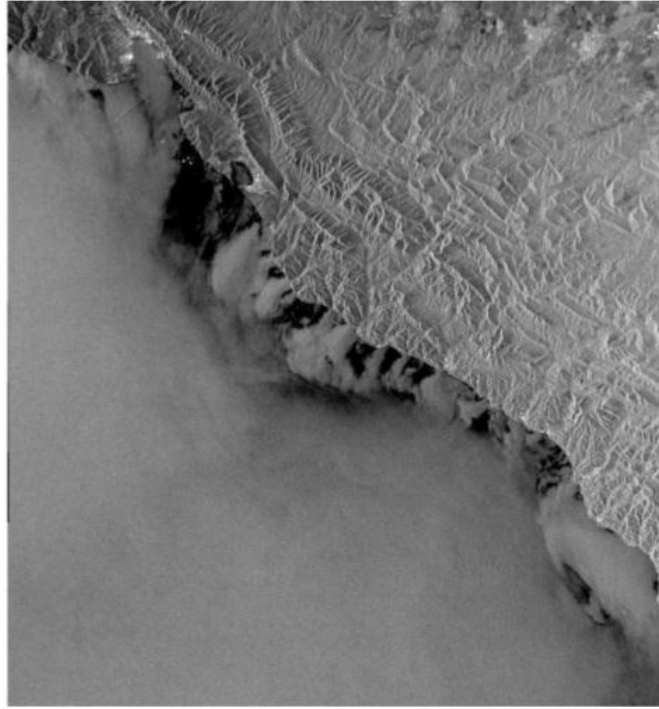


Figure 7. A satellite image demonstrating the sea surface signatures of a Katabatic wind event taking place over the east coast of the Black Sea on April 30, 2008 at 19:07 UTC (From ESA)

3. FOEHN WINDS

The driving mechanism for the warm Foehn winds is descending motion of the airflow. Therefore, they are observed on the lee side of mountain ranges. They are accompanied by ascending temperatures, diffusion of low-level clouds, and descending relative humidity. Apart from the eastern part of the Black Sea, Foehn winds are mostly observed on the north side of the Alps (Alpers et al. 2010).



Figure 8. A satellite image demonstrating the sea surface signatures of a Foehn wind event taking place over the southeast coast of the Black Sea on January 11, 2010 at 07:31 UTC (From ESA)

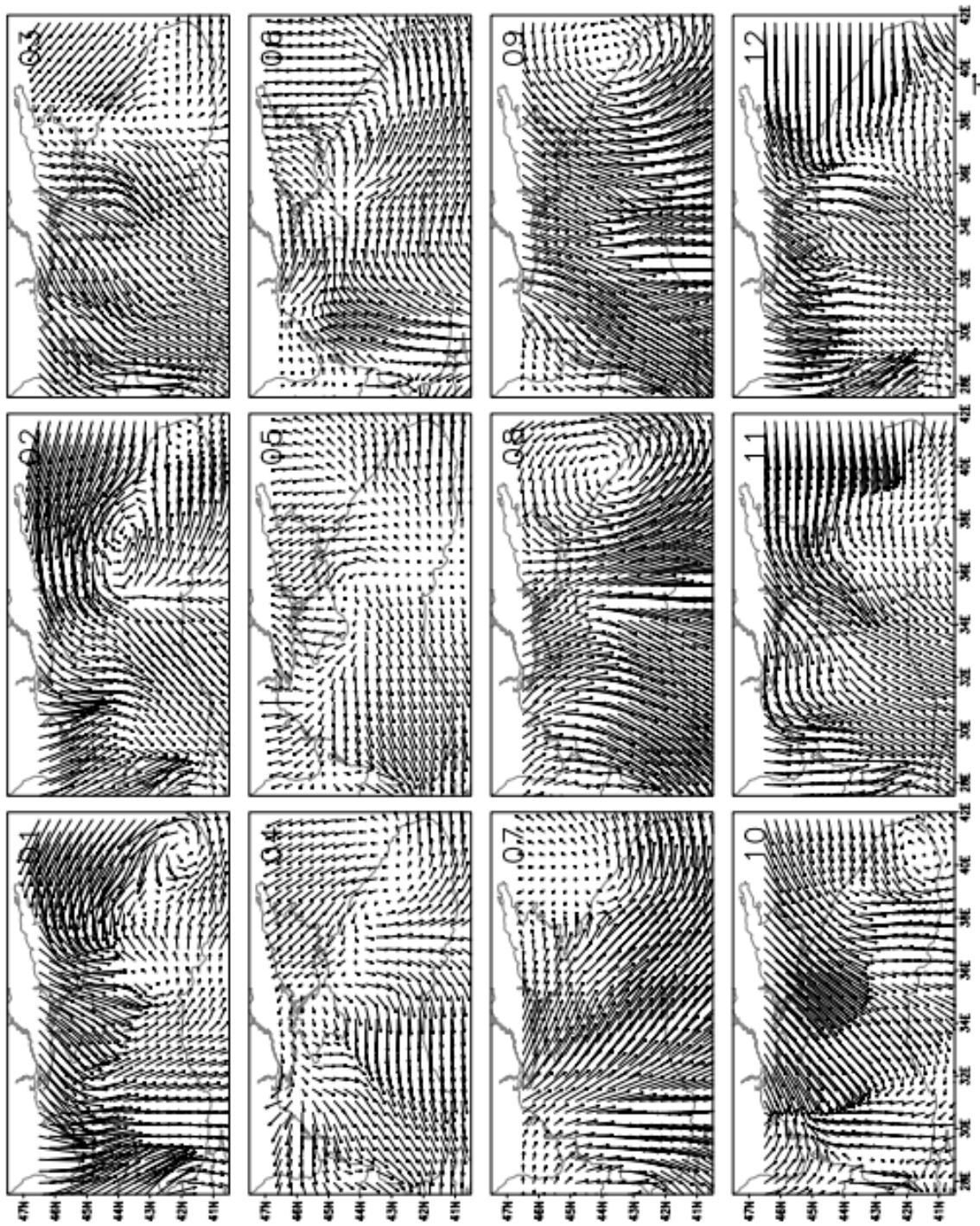


Figure 9. Monthly averaged climatological wind fields. The arrow scale equals 1 m/s.
(From Peneva and Stips 2004)

D. TEMPERATURE AND SALINITY

As a result of the abundance of freshwater sources (e.g., rivers and rainfalls) compared to lost freshwater due to evaporation, the Black Sea holds a positive freshwater balance. More specifically, the evaporation removes around 354 square km of fresh water, whereas freshwater inputs from river outflows and precipitations are approximately 350 square km and occur approximately 230 times each year, respectively. This positive freshwater balance of the Black Sea results in an average of 0.43m gain in sea level in comparison with the Marmara Sea.

The excessive amount of water in favor of the Black Sea runs into the Marmara Sea via the strait of Bosphorus. Therefore the straits comprise two different flows. One of them is the upper flow, which transports the surface water from the Black Sea, and the other is the bottom flow that transports 35‰ of the Mediterranean origin salt water to the Black Sea. The salinity of the surface waters is 17.5 – 18‰. It is relatively low due to the mixing process of the salty waters with the original waters of the basin. In terms of the volume, the bottom flow is approximately 300 cubic km, which is around half of the surface flow.

The surface salinity has seasonal variability. In terms of the vertical distribution of salinity, an increase is observed at 50 m depth; when the depth hits 200 m the increase rate is still remarkable, whereas below 200 m the increase rate is much slower. The salt composition of the waters of the Black Sea resembles the composition of oceans. The Black Sea waters house remarkable measures of nutrients, especially the mixtures of nitrogen and phosphorus that originate in the rivers. Even though the surface waters' temperature shows variability throughout the year, this is not the case for the water column below the surface. For these deeper waters, a rather unique vertical change in temperature is observed. The depths that the minimum temperatures have been observed start from 50–60 m go down to 80–90 m. For the deeper parts of the water column, a slow increase in the temperature is noted until reaching the seabed (~ 2200 m).

The density of the seawater is assessed by the vertical distribution of salinity and temperature values. Due to the unique features the Black Sea introduces, it is comprised

of two diverse water layers: the first measuring from 0 to about 200 m (called the lighter upper layer), and the second layer measuring between 200 m and the seabed (called the heavier lower layer). The weak vertical circulation arises within the waters due to this stratification. The mixing of these distinct layers does not occur efficiently. Furthermore, life in the Black Sea is significantly influenced by this structure (http://www.blackseascene.net/content/content.asp?menu=0040032_000000).

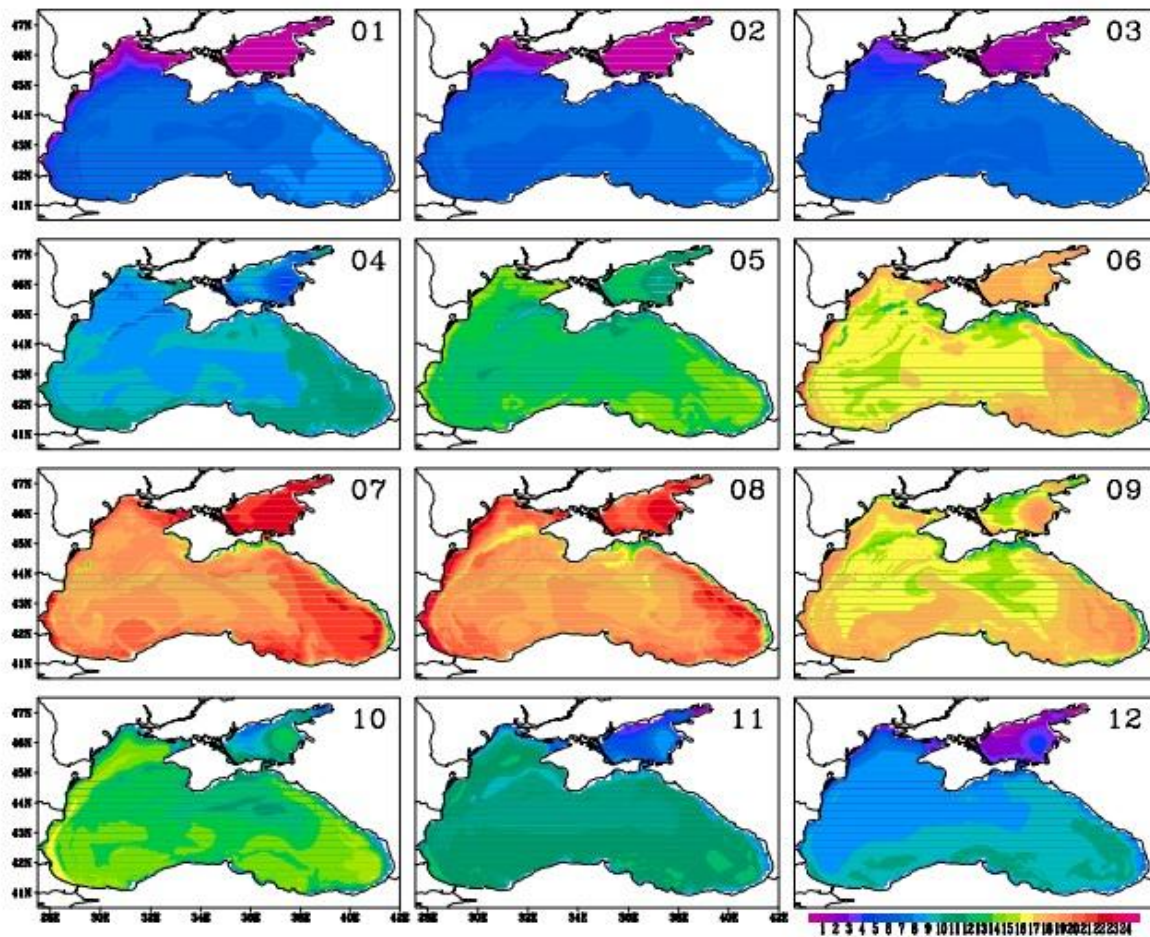


Figure 10. Monthly averaged mixed-layer temperature of the Black Sea obtained through the climatological run of General Estuarine Transport Model (GETM) (From Peneva and Stips 2004)

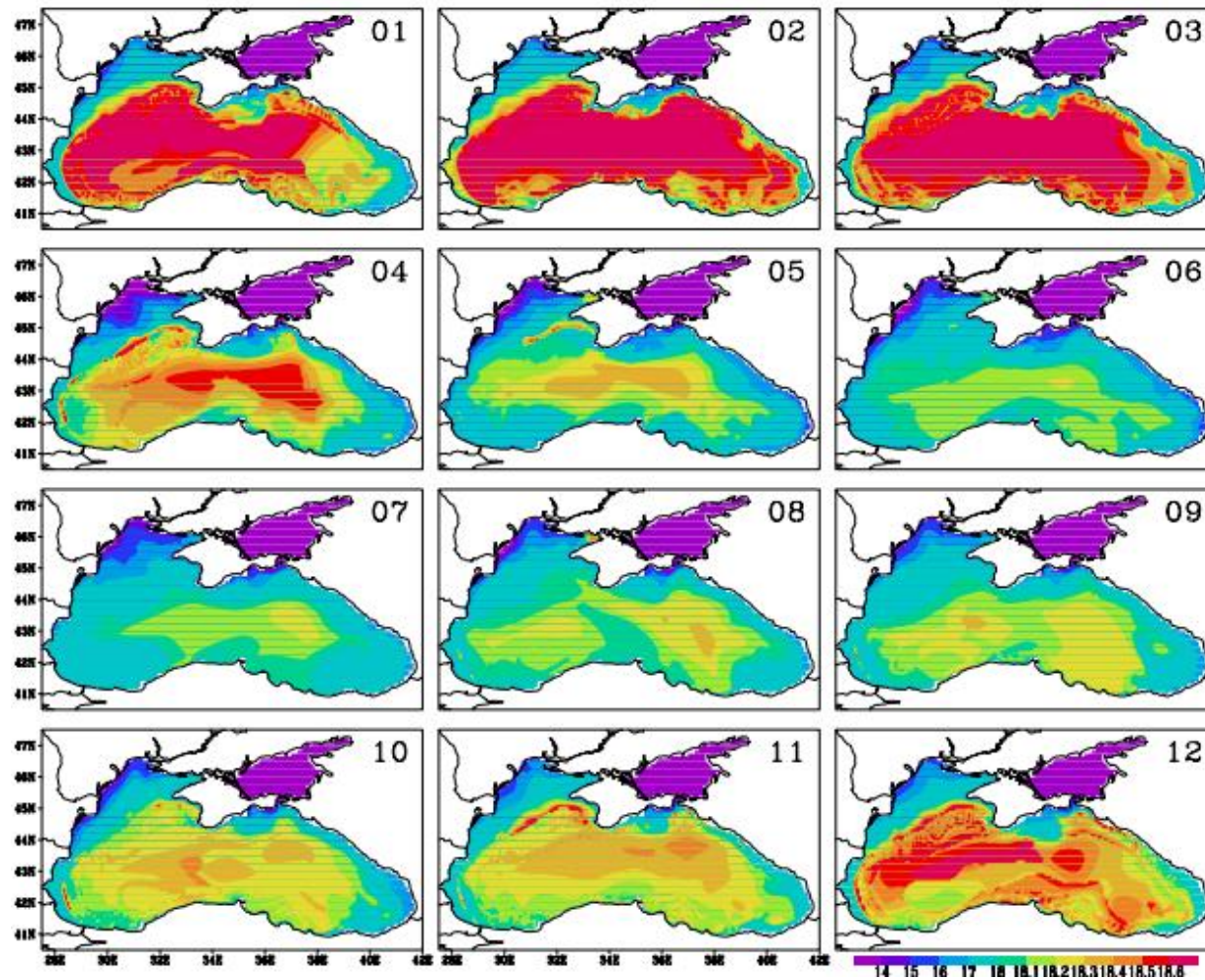


Figure 11. Monthly averaged mixed-layer salinity of the Black Sea obtained through the climatological run of General Estuarine Transport Model (GETM) (From Peneva and Stips 2004)

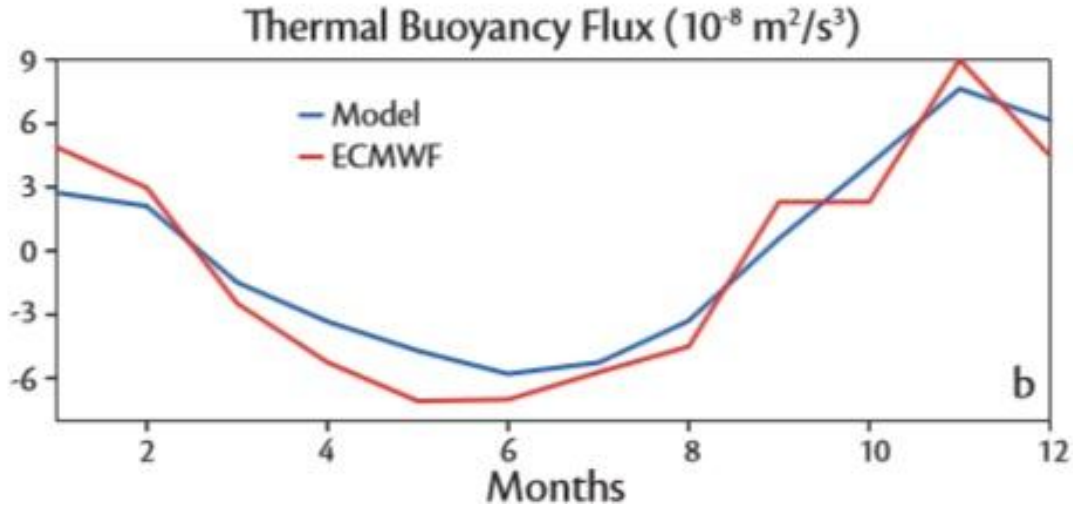


Figure 12. Illustration of the temporal variability of the thermal buoyancy flux from the 5-minute-resolution Black Sea Modular Ocean Model (MOM) (Stanev et al. 2003), along with the matching curve calculated from the European Centre for Medium-Range Weather Forecasts (ECMWF)-reanalyzed data (From Stanev 2005).

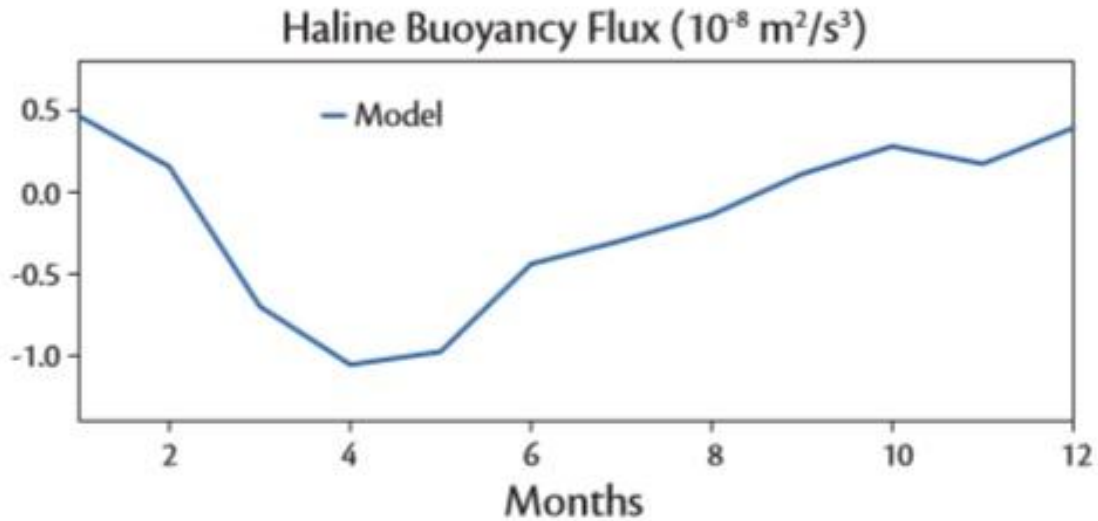


Figure 13. Illustration of the temporal variability of the haline buoyancy flux from the 5-minute-resolution Black Sea Modular Ocean Model (MOM) (From Stanev 2005).

According to model simulations (Stanev and Staneva 2001), the peak of the water's heating ($2 \times 10^2 \text{ W/m}^2$) occurs in June, whereas the peak of the cooling ($3 \times 10^2 \text{ W/m}^2$) takes place in early winter. Moreover, the amplitude of the haline buoyancy flux is

surpassed by the amplitude of the thermal buoyancy flux by an order of magnitude. On the other hand, in terms of net values, the net haline buoyancy flux is approximately four times larger than the net thermal buoyancy flux.

E. CHLOROPHYLL-A

The concentration of chlorophyll-a is the most suitable and useful parameter in terms of monitoring the marine ecosystem. For instance, there is a high correlation between the level of the chlorophyll-a concentration and the primary production; that level is also determined as the indicator of the phytoplankton biomass. Since the concentration of chlorophyll-a has been monitored for many years and still continues, there are many data sets available for research purposes (Yunev et al. 1987; Berseneva 1993; Vedernikov and Demidov 1993; Yilmaz et al 1998; Yunev et al 2002; Kopelevich et al. 2002).

Satellite ocean-color data provides the synoptic scale measurements of marine ecosystems, and the concentration of chlorophyll-a is an exclusive feature of these ecosystems. Temporal and spatial distributions of the chlorophyll-a concentration are identified by satellite ocean-color sensors lately, which are widely accepted as the standard tool for this particular data collection (Kopelevich et al. 2002). The Coastal Zone Color Scanner (CZCS) was designed as the first-generation ocean-color sensor and Nimbus-7, a NASA satellite, was the carrier of this sensor. During the period of October 1978 to June 1986, a large amount of beneficial information regarding ocean color was collected via the CZCS. This period is considered the stable phase of the Black Sea ecosystem. The severe changes in the Black Sea ecosystem began shortly after that period. These changes were accompanied by the rush of the “*Mnemiopsis leidyi*,” which was carried to the region mistakenly since the summer of 1988 (Shuskina and Vinogradov 1991). These changes make the CZCS measurements even more important since they allowed researchers to identify the period of stable conditions in the Black Sea, and these changes enabled researchers to compare current conditions with the stable conditions in order to better understand the subsequent occurrences (Kopelevich et al. 2002). Due to the CZCS’ lack of significant coverage of the Black Sea region during cold

periods, it is not feasible to study the interannual fluctuations between warm and cold periods in the region (Nezlin et al. 1999; Kopelevich et al. 2002).

According to the mean monthly distributions provided by Kopelevich et al. (2002), the distinction between the regions of the western shelf and the Black Sea's open region is obvious. The eastern shelf, on the other hand, appears to be confined adjacent to the coastline, while the regions of the western shelf demonstrate great variability in terms of their mean monthly distributions. The open regions show relatively uniform patterns, especially for the period between April and October (Kopelevich et al. 2002).

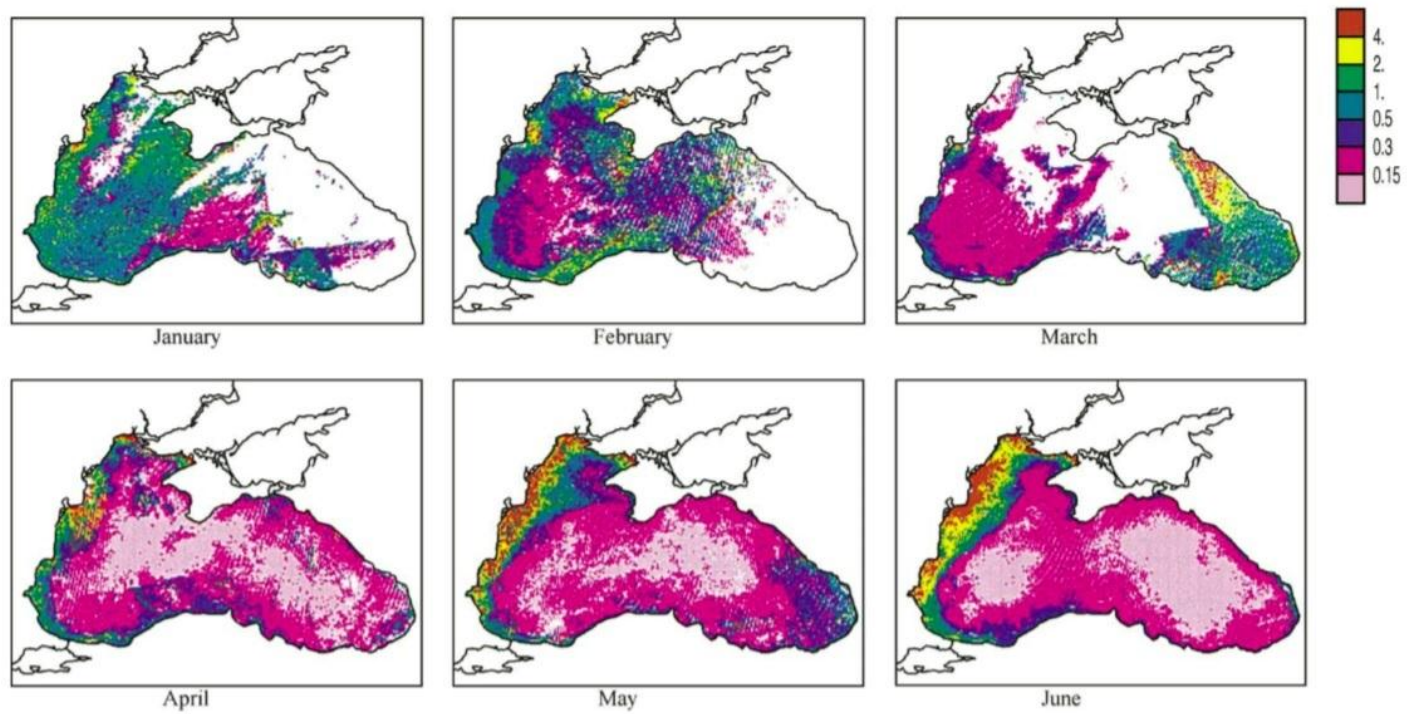


Figure 14. The average monthly distributions of chlorophyll-a (mg/m^3) found in the CZCS data for the first 6-month period (From Kopelevich et al. 2002).

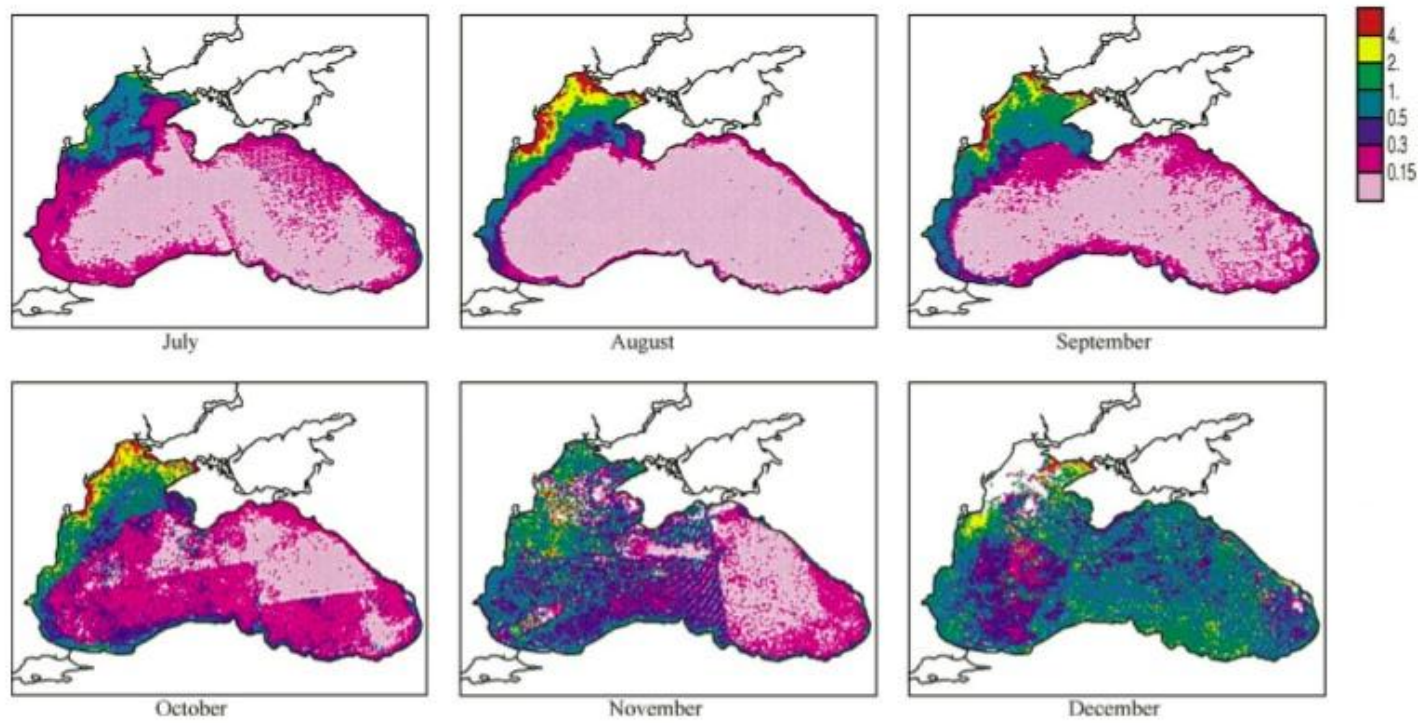


Figure 15. The average monthly distributions of chlorophyll-a (mg/m^3) found in the CZCS data for the second 6-month period (From Kopelevich et al. 2002).

In 1993, Vedernikov and Demidov studied the surface chlorophyll-a concentrations based on different parts of the basin during different seasons. They chose November through March as the cold period, May through September as the warm period, and the months of April and October as the transition periods. According to this study, the mean chlorophyll-a concentrations at the surface of the open parts of the Black Sea were found to be 0.97-1.52 mg/m³ during the cold period, 0.28-0.38 mg/m³ during the warm period, 0.61 mg/m³ during April, and finally 0.43 mg/m³ during October. These results are well-correlated with the outcomes of the study done by Kopelevich et al. 2002 which selected the same periods. In the latter study, the concentrations found for the open parts of the basin were appeared to be 0.70-0.83 mg/m³ during the cold period, 0.14-0.15 mg/m³ during the warm period, 0.19-0.20 mg/m³ during April, and 0.18-0.25 mg/m³ during October. Both studies detected the lowest concentrations during warm periods and the highest concentrations during the cold periods. The differences between the concentrations of chlorophyll-a are justified by the additional time frame in the latter study (Kopelevich et al. 2002).

The open parts of the western shelf and the eastern shelf seemed to share the same mean chlorophyll-a concentration in terms of mean annual and warm period values. There was an obvious discrepancy for the cold period as the mean concentration for the open parts of the eastern shelf was found to be approximately 19% more in comparison with that of the western shelf. During the transition months, however, the western shelf demonstrated a 10-28% more concentration (Kopelevich et al. 2002).

The coastal parts of the eastern shelf exhibited higher mean concentration values compared to the open parts throughout the year. This difference was around 40% during the cold period, more than twice the amount during the warm period, and finally 80% higher for the annual mean. In terms of the seasonal changes, on the other hand, both the coastal and the open parts of the Black Sea had the same nature. During the cold period, the chlorophyll-a concentrations were detected as four to six times more than the amount during the warm period and three to five times more than the amount during April and October (Kopelevich et al. 2002).

For the western shelf, the mean chlorophyll-a concentrations found in the open parts and the coastal parts of the Black Sea differed significantly, particularly for the warm period. The Romanian coast, which is heavily influenced by the Danube River flow, was found to have the highest mean chlorophyll-a concentrations throughout the entire year. During the warm period, this region's waters had values 18 times more as compared with the open parts and approximately nine times more as compared to the eastern shelf. Since the homogeneity in the water column rises during the cold period, the discrepancies among the different regions (west shelf vs. east shelf, open region vs. coastal region, etc.) of the basin become less pronounced. Even though the whole Black Sea basin is found to be the most homogeneous during the cold period, open parts, particularly, tend to exhibit the highest homogeneity during the warm period (Kopelevich et al. 2002).

In previous studies, the assessment of the long term variability of the Black Sea physical properties is made using either satellite data (e.g. Stanev and Peneva, 2002; Ginzburg et al., 2004; Nardelli et al., 2010; Grayek et al., 2010) or in-situ data (e.g. Oguz et al., 2006; Oguz and Gilbert, 2007). In addition to that, impacts of the North Atlantic Oscillation (NAO), the East Atlantic/West Russian (EAWR) (e.g. Oguz et al., 2006) and the El Nino Southern Oscillation (ENSO) on the Black Sea hydrodynamics were investigated (e.g. Ginzburg et al., 2010; Oguz et al., 2006). Aside from those studies, Arthur et al. (2012) quantify the correlations between the variability of different physical processes concerning the Black Sea internal dynamics in their study, using the SOM for the wind and EOF for the Sea Level Anomaly (SLA) with connection to Sea Surface Temperature (SST).

The main aim of this research can be summarized as follows: (1) to utilize an SOM to detect recurrent patterns of the surface winds for the 10-year period that follows the study of Arthur et al. (2012), (2) to utilize an SOM to detect recurrent patterns of the surface currents for the same 10-year period, (3) to investigate the influence of the large-scale teleconnection indices on recurrent patterns of both data sets, (4) to correlate recurrent patterns of the both data sets with each other, (5) to superimpose the chlorophyll-a concentration on recurrent patterns of both data sets.

THIS PAGE INTENTIONALLY LEFT BLANK

III. DATA SOURCES

A. AVISO

Geostrophic velocity anomalies used in this research were obtained through the Archiving, Validation, and Interpretation of Satellite Oceanographic data (AVISO), which is a system located at Collecte Localisation Satellites (CLS). CLS was founded in 1996 and the specializations of this processing center are data collection, trajectory of satellites, as well as satellite-based ocean observations. Conductivity-Temperature-Depth-Oxygen Profiler (CTDP) is another system run by both CLS and American Physical Oceanography–Distributed Active Archive Center (Po-Daac). AVISO is connected to CTDP, which is capable of downloading Geophysical Data Records (GDR), Interim Geophysical Data Records (IGDR) and processed data from both centers. On the other hand, French geophysical corrections, orbit files for the French, and American instruments are downloaded by AVISO (http://www.aviso.oceanobs.com/no_cache/en/newsstand/newsletter/newsletter01/what-is-aviso/).

1. ALTIMETRY

a. History

The discussion of using radar instrumentation in space for oceanography purposes first took place in 1969 at the congress of Williamstown. Thus, measurement of the sea level using radar techniques was initially aimed by satellite altimetry. First altimetry measurements tried to determine the topography of the ocean surface. With the missions Skylab and Geos-3, the United States became the first country that ever used the satellite-borne altimeter technology in history. Following the United States, in 1991, the European Space Agency (ESA) launched ERS-1 and got involved to this concept.

Centre National d'Etudes Spatiales (CNES) was working on placing an altimeter called Poseidon onboard of Spot-1 in 1981. Concurrently, NASA was evaluating the Topex (Topography Experiment). Besides sharing interest in new missions they had one more detail in common: both agencies were suffering from small budgets that would not allow them to execute the missions by themselves. In 1983, negotiations

began regarding how to combine these two projects together, and in 1987 the partnership was officially established. Instruments were going to be launched on a United States satellite using a European rocket, and the project was named Topex/Poseidon (T/P).

Topex/Poseidon was critical for the oceanography community, as it provided increased knowledge of oceanography and improved the community's understanding in terms of ocean observation. Even the in-situ observations made over the previous one hundred years were not capable of providing the same amount of information that was collected during the ten-day cycle of Topex/Poseidon measurements (<http://www.aviso.oceanobs.com/en/altimetry.html>).

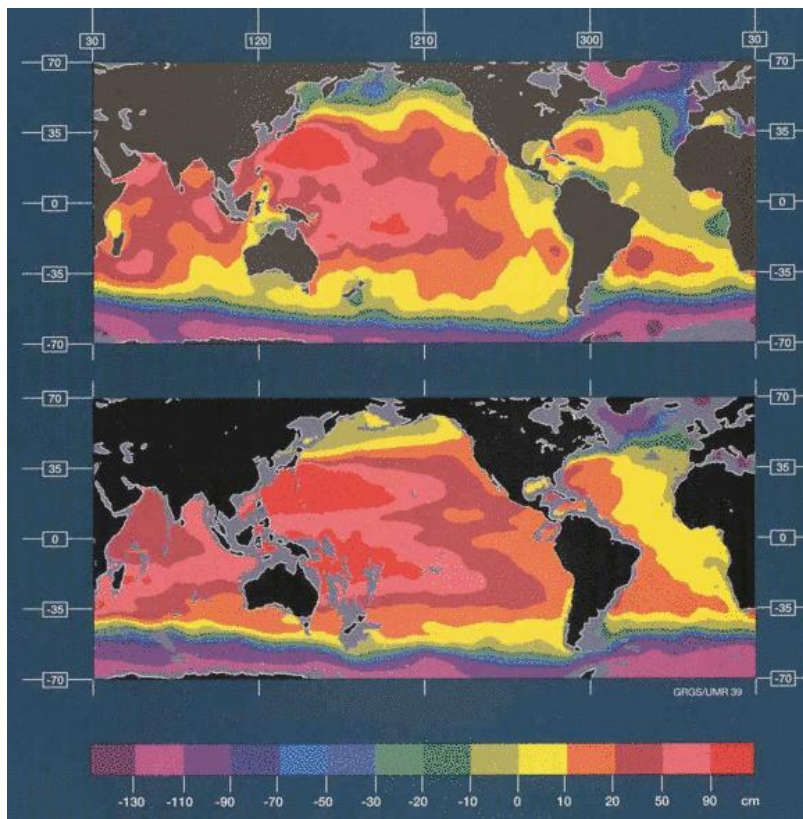


Figure 16. A Topex/Poseidon cycle compared to 100 years of in situ data (From <http://www.aviso.oceanobs.com/en/altimetry/history.html>)

b. Principle

High-frequency signals (at least 1700 pulses Hz) are emitted to Earth by the altimeters and, once they are reflected, the echo from the sea surface is received by the altimeters again. The basic purpose of this exercise is to find out the satellite-surface distance. The time it takes for a radar pulse to travel from the satellite to the surface and return to the satellite again after reflection is measured. Additionally, it is known that electromagnetic waves travel at the speed of light. So, the distance is calculated in light of this information. The presence of the atmosphere complicates this process since the water vapor that it contains, or the ionization taking place in it can decelerate the electromagnetic waves. Thus, the results should be adjusted according to the interferences of the atmosphere. There is potential for extracting other kinds of information through altimetry. One of them being the characteristics of the surface that reflection of the signal takes place and it can be determined by focusing on the shape and the magnitude of the echoes.

Tracking altimetry satellites is another crucial process and should be done accurately. There are a variety of ways for tracking satellites, one of which is a system called Doris. Doris is a location system that was developed by CNES, and put onboard of Topex/Poseidon. It is connected to a network of 50 transmitting ground beacons spread worldwide. The Doppler shift on the beacon signals is used by Doris to identify the satellite's velocity as it orbits (<http://www.aviso.oceanobs.com/en/altimetry.html>).

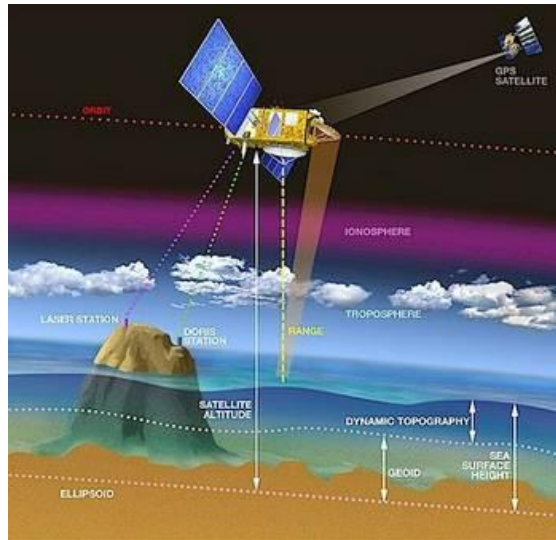


Figure 17. The concepts and systems that contribute to the altimetry measurement (From Cnes)

c. *Multi-Satellites*

There should be a reasonable balance between the temporal and spatial resolutions of an altimetry satellite when determining its orbit. One way to overcome this compromise is to use Multi-Satellites with different orbits/resolutions, and to take advantage of the multiple views of the same spot. This process enables fine tuning of the separate measurements (<http://www.aviso.oceanobs.com/en/altimetry.html>).

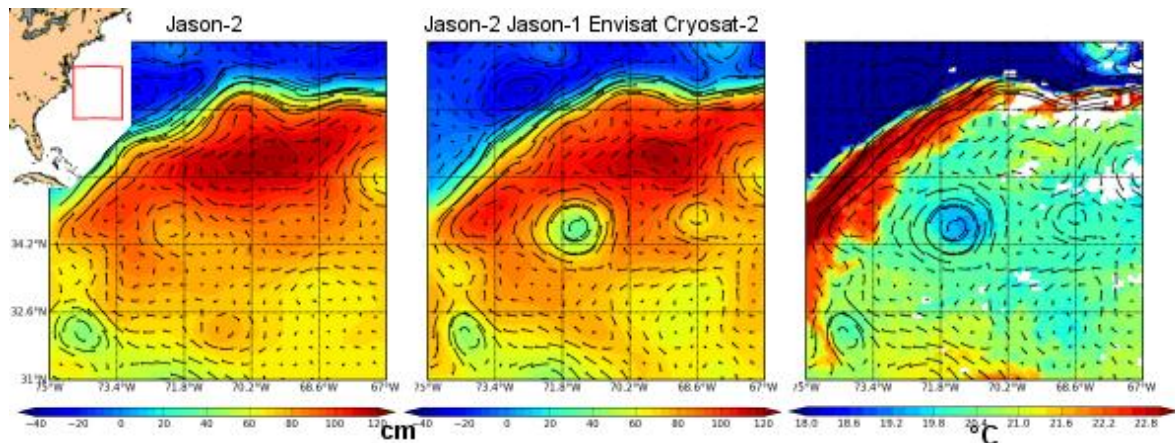


Figure 18. Comparison of the details of images collected from a single satellite and multi-satellites (From CLS/Cnes)

2. MISSIONS

Since it was first founded, the system AVISO has been conducting satellite altimetry missions to provide an immense international user community with data that is collected through precise and high-quality altimetry measurements with the help of advanced technology and better orbit determination. For instance, Topex/Poseidon (T/P) had been the pioneer in highly precise altimetry measurements and it changed the perspective significantly in terms of systematical sea surface height observations.

There are ongoing missions, while some have been terminated. Future missions are planned to start in 2013. Certain missions are executed by standalone agencies, whereas others have the contribution of groups. The U.S. Navy, the European Space Agency (ESA), the National Aeronautics and Space Administration (NASA), Centre National d'Etudes Spatiales (CNES), the China Academy of Space Technology, the Indian Space Research Organization (ISRO), the European Organisation for the Exploitation of METeorological SATellites (EUMETSAT), and the National Oceanic and Atmospheric Administration (NOAA) are agencies that have been involved in at least one of the missions conducted.

Table 2. Specifications of the Satellites Used in the Past Missions of AVISO

Satellite	Geosat	ERS-1	T/P	GFO	ERS-2	Envisat
<i>Launch Date</i>	03/10/1985	07/17/1991	08/10/1992	02/10/1998	04/21/1995	03/01/2002
<i>End Date</i>	01/31/1990	03/31/2000	01/18/2006	11/26/2008	07/06/2011	May 2012
<i>Altitude</i>	800 km	785 km	1336 km	800 km	785 km	782.4-799.8 km
<i>Inclination</i>	N/A	98.52 ⁰	66 ⁰	108 ⁰	98.52 ⁰	98.55 ⁰
<i>Repetitivity</i>	N/A	33, 35, 168 days	9.9156 days	17 days	35 days	30-35 days
<i>Agency</i>	U.S. Navy	ESA	NASA and CNES	U.S. Navy and NOAA	ESA	ESA
<i>Goal</i>	Describe the marine geoid	Observe Earth and its environment	Measure sea surface height	Measure ocean topography	Observe Earth and its environment	Observe Earth's atmosphere and surface

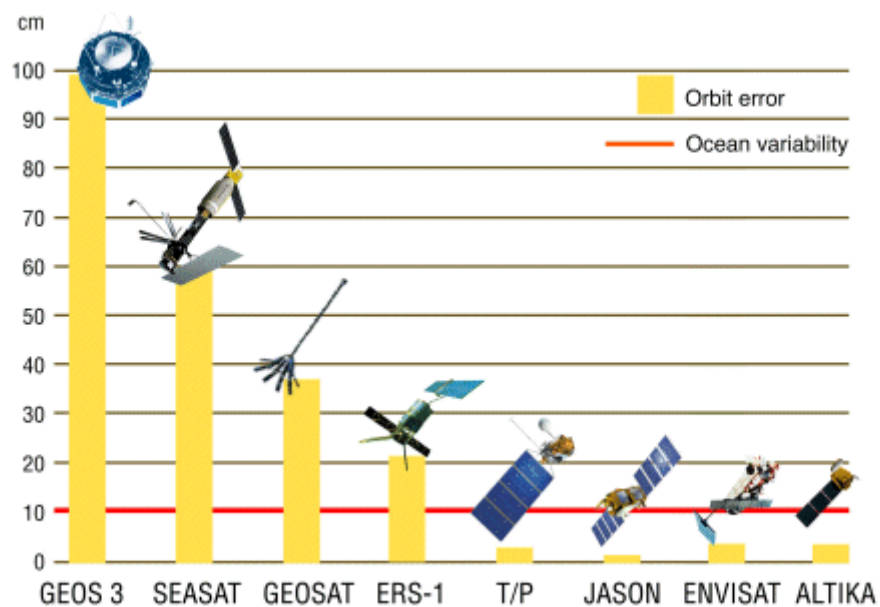


Figure 19. Altimetry measurement accuracy evolution since the first mission (From Cnes)

Table 3. Specifications of the Satellites being Used in the Current Missions of AVISO

Satellite	HY-2	Cryosat	Jason-1	Jason-2
<i>Launch Date</i>	08/15/2011	04/08/2010	12/07/2001	06/20/2008
<i>Altitude</i>	971 km	717 km	1336 km	1336 km
<i>Inclination</i>	99.3 °	92 °	66 °	66 °
<i>Repetitivity</i>	14, 168 days	369 days	9.9156 days	9.9156 days
<i>Agency</i>	China Academy of Space Technology	ESA	CNES and NASA	CNES, NASA, EUMETSAT and NOAA
<i>Goals</i>	Observe the ocean dynamics	Polar observation	Measure sea surface height	Measure sea surface height

The Spot satellite family began their mission with the very first member Spot-1, which was in service from February 22, 1986 to 2001. The last two members of the family are still active and working. Spot-4 was launched on March 24, 1998, and Spot-5 was launched on May 4, 2002. The altitude for Spot family satellites is set at 830 km. The agency behind them is CNES and their goal is to observe Earth.

Table 4. Specifications of the Satellites Planned to be Used in the Future Missions of AVISO

Satellite	Saral	Sentinel-3	Jason-3	Jason-CS	Swot
<i>Launch Date</i>	2013	2014	April 2014	End of 2017	2020
<i>Altitude</i>	~800 km	814.5 km	1336 km	1336 km	970 km
<i>Inclination</i>	98.55 ⁰	98.65 ⁰	66 ⁰	66 ⁰	78 ⁰
<i>Repetitivity</i>	35 days	27 days	10 days	10 days	22 days
<i>Agency</i>	ISRO and CNES	ESA	CNES, NASA, EUMETSAT and NOAA	CNES, NASA, EUMETSAT and NOAA	CNES and NASA
<i>Goals</i>	Observe the oceans	Deliver routine operational services	Measure sea surface height	Measure sea surface height	Cover more than 90% of the globe

Future missions aim for better temporal and spatial resolutions to enable studies that phenomena and variations are more closely investigated. In particular, Saral will be equipped with Ka-band which is going to provide better observations of ice, rain, wave heights, and coastal zones. On the other hand, the altimeter on Sentinel-3 will feature both low and high resolution modes. The low resolution mode will be used over oceans and other homogenous surfaces, whereas the high resolution mode will be used over sea ice and for other applications that require more detail (<http://www.aviso.oceanobs.com/en/missions.html>).

3. DATA

There are five different products available: namely sea surface height, surface geostrophic velocity (or anomaly), wind and wave, auxiliary data, indicators, and in-situ products. There are various options for each of these products, as well. The users can work on either a global or regional scale; they can use real time (RT), near real time (NRT), or delayed time (DT) versions of these products; and users even can reach the data from multi-satellites which is called “merged data.”

The delayed time product comes with two versions: Reference (Ref) and Updated (Upd). Reference series are produced by two satellites at a given time (Jason 2–Envisat, Jason 1–Envisat, or Topex/Poseidon–ERS) and they are homogenous. Whereas Updated series are fed by up to four satellites (Jason-2–Jason-1–Envisat since 2009, or Jason-1–Topex/Poseidon–Envisat–GFO from October 2002 to September 2005), and they are treated by a better verification process, yet they are inhomogeneous in terms of quality.

Products are distributed by the partnership of Segment Sol multimissions d'ALTimétrie, d'Orbitographie et de localisation précise (Ssalto), and the Data Unification and Altimeter Combination System (Duacs). Both systems process the data that comes from all the altimeter missions and they aim to provide the users with consistent information that is as homogenous as possible. Ssalto, additionally, operates facilities on earth in order to control the Poseidon and Doris instruments.

The product used in this research is delayed time (Upd) and merged mean sea level anomalies (DT-MSLA) for the Black Sea region. The content of this product is sea surface height on a regular grid with the resolution of $1/8^0 \times 1/8^0$, calculated with respect to a mean sea level profile as well as geostrophic velocity anomalies that correspond to height. The data is available weekly, and provided each Wednesday of the week that the data is averaged over (<http://www.aviso.oceanobs.com/en/data/products/sea-surface-height-products/regional/msla-black-sea.html>; “The altimeter products were produced by Ssalto/Duacs and distributed by Aviso, with support from Cnes (<http://www.aviso.oceanobs.com/duacs/>)”).

B. SEAWIFS

The Sea-viewing Wide Field-of-View Sensor (SeaWiFS) Project aims to collect, archive, and distribute validated research data regarding ocean bio-optical properties on a global scale and gathered by an ocean color sensor orbiting around the Earth. Different quantities and types of microscopic marine plants (marine phytoplankton) affect the ocean color in a variety of ways. More specifically, the higher the concentration of chlorophyll and plant pigments other than chlorophyll, the greener the water color. The goal here is the derivation of that concentration, using ocean observations made by a satellite and evaluating the ocean color from those observations (http://oceancolor.gsfc.nasa.gov/seawifs/background/seawifs_background.html).

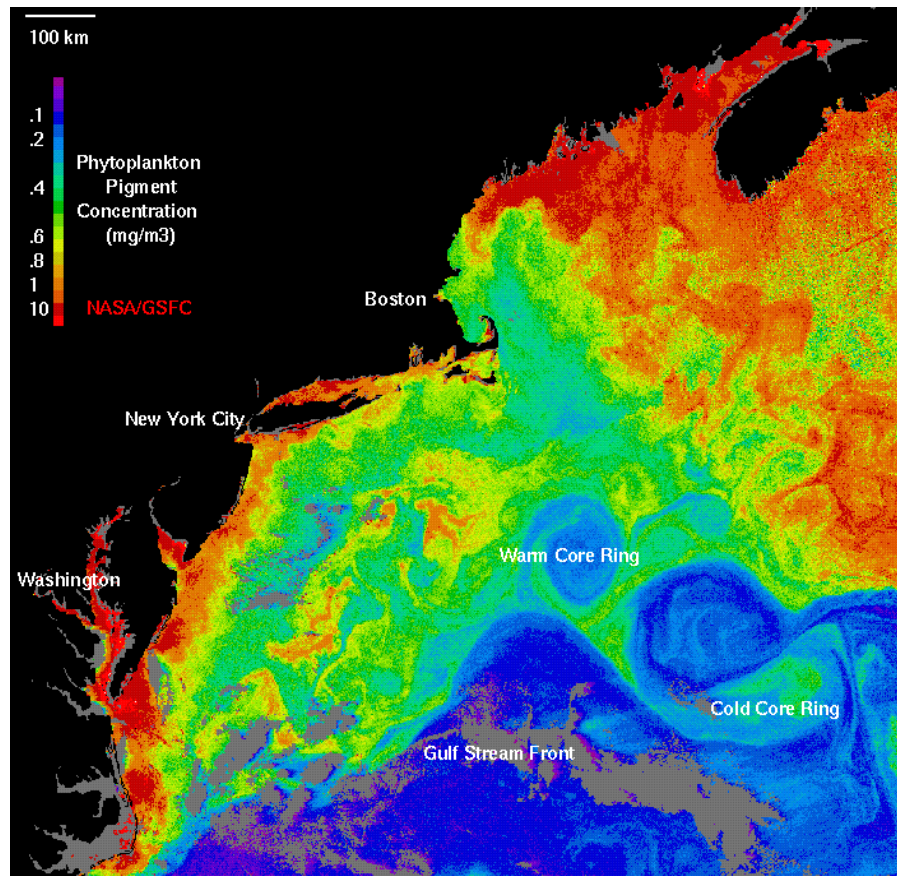


Figure 20. An example of the images collected by SeaWiFS Project (From NASA/GSFC)

1. OBJECTIVES

The goal of SeaWiFS data is to study the influence of oceanic factors on global change. Understanding the role of oceans in the biogeochemical cycles (e.g., carbon cycle etc.), which is studied by using the chlorophyll's and other marine phytoplankton productions' magnitude and variability, is intended. For that purpose, the scientific community has been using SeaWiFS data to identify the limits of highly abundant growth (spring blooms), as well as the length of time over which this growth occurs.

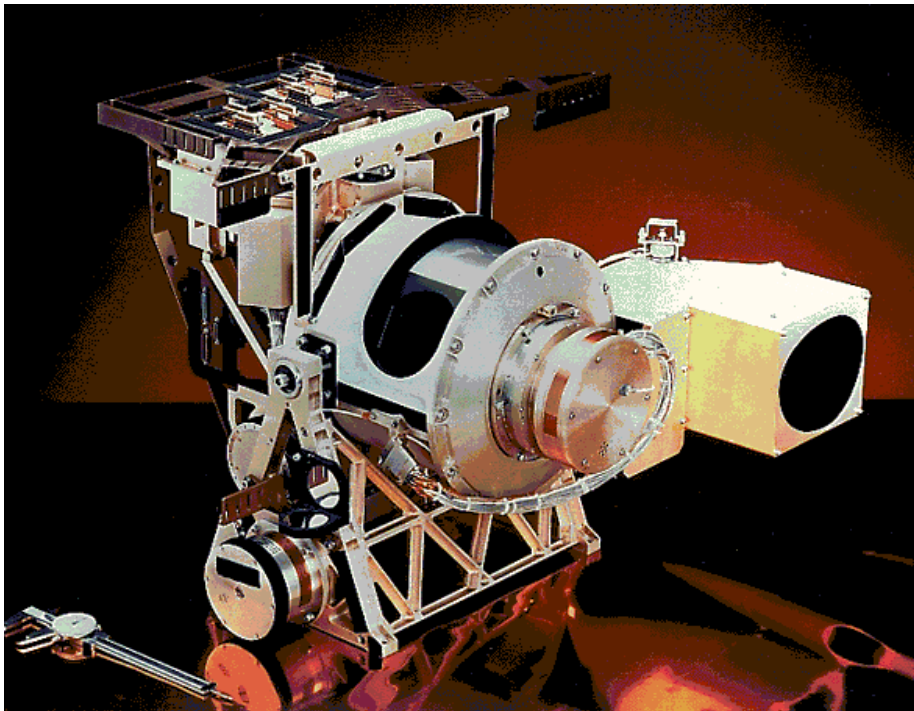


Figure 21. A photograph of the scanner assembly used in SeaWiFS (From http://oceancolor.gsfc.nasa.gov/seawifs/background/figures/brochure_fig1.gif)

The objective of the project has been to accurately collect ocean color data on a global scale for at least 5 years and extract reasonable biological parameters (photosynthesis rates, etc.) from this data with the help of auxiliary information. The next step has been to make these findings available to researchers around the world (http://oceancolor.gsfc.nasa.gov/seawifs/background/seawifs_970_brochure.html).

2. ORGANIZATION

SeaWiFS data is broadcasted by OrbView-2 (OV-2) satellite in real time to the Goddard Space Flight Center (GSFC), the High-Resolution Picture Transmission (HRPT) station, and other stations, whereas Global Area Coverage (GAC) and Local Area Coverage (LAC), recorded data in other words, is broadcast to the GSFC, the ORBIMAGE, and the WallopsFlight Facility (WFF). Next, HRPT, GAC, LAC, and HRPT data are delivered to the SeaWiFS Data Processing System (SDPS). The SDPS is comprised of GSFC mission operations; SeaWiFS data processing; data capture; and calibration, validation, and data quality elements.

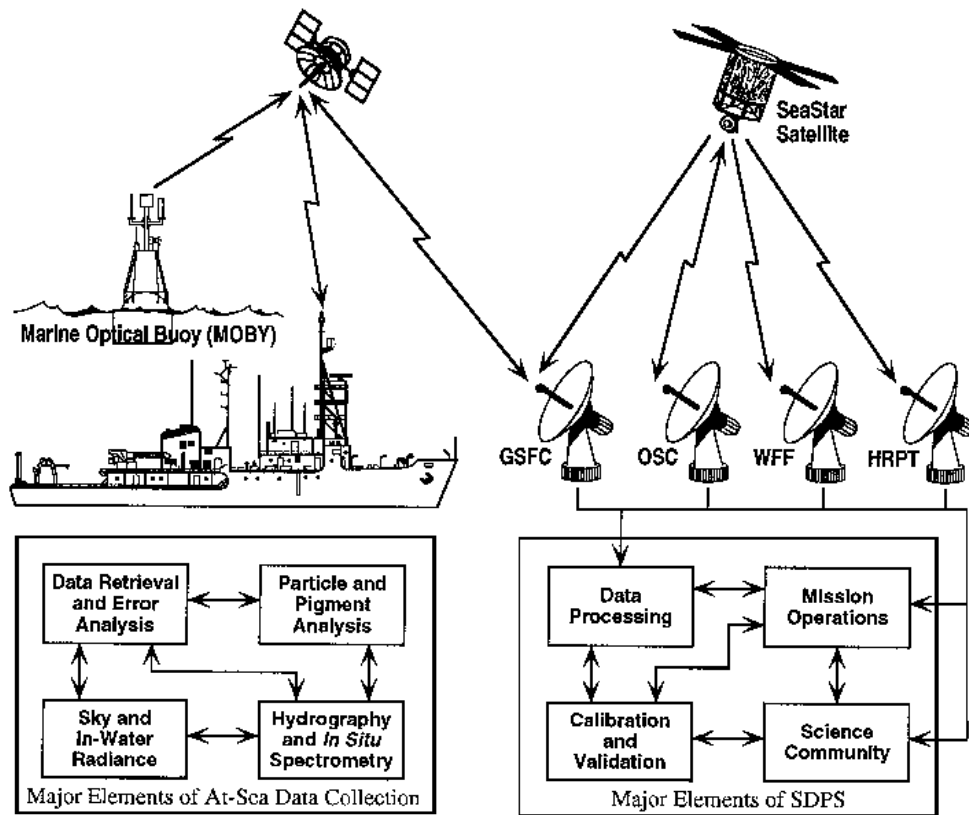


Figure 22. Major elements of SeaWiFS Project (From http://oceancolor.gsfc.nasa.gov/seawifs/background/figures/brochure_fig3.gif)

Raw data from the satellite is received by the data processing element and standard global ocean color data products are generated out of that raw data. The GSFC

Earth Observing System Data and Information System (EOSDIS) Distributed Active Archive Center (DAAC) is responsible for archiving SeaWiFS data and distributing it to researchers. Then, it receives that standard global ocean color data.

The calibration and validation element establishes the procedures of calibration for SeaWiFS data and updates those procedures. In order to do that, this element collects auxiliary data (i.e., wind, atmospheric pressure, etc.), analyzes trends and variations, and validates higher-level products with correlative data.

The mission planning element links SeaWiFS Project Office (SPO) and ORBIMAGE together to enable a connection that tracks automatic data measurements and transmissions, schedules the scientific maintenances, and catches problems. Additionally, the orbit elements and navigation information are provided by this element to some extent. Mission management, the space segment, and the command and data acquisition station are ORBIMAGE's responsibilities (http://oceancolor.gsfc.nasa.gov/seawifs/background/seawifs_970_brochure).

3. DATA COLLECTION

Two different scientific data are produced by SeaWiFS in terms of spatial resolutions: LAC and GAC. Even though the broadcast for LAC is continuous, it is selectively recorded. The recording process for GAC, on the other hand, is continuous and is executed on board of the satellite. Direct broadcasts of LAC for the East coast of the United States have been received by the GSFC and other real-time broadcasts of LAC have been received by a number of global HRPT stations. Recorded data of GAC and LAC are first received by NASA WFF, and then forwarded to SDPS at GSFC.

Acquiring full GAC data every 48 hours is essential for the science goals of the project. Therefore, almost all of the recording capacity onboard of the spacecraft and transmission time to GSFC is assigned for that requirement. Limited space left from the GAC is used for LAC recording. The LAC recording process has been allotted in priority order: 1) watching critical sensor functions, 2) conducting essential optical calibration and validation processes, and 3) collecting data for science studies that are in need of data

in full resolution (http://oceancolor.gsfc.nasa.gov/seawifs/background/seawifs_970_brochure.html).

4. SPACECRAFT AND SENSOR

SeaWiFS instruments are carried by the SeaStar spacecraft which was built by Orbital Sciences Corporation and was launched on August 1, 1997 to Earth's low orbit. The control and command of the satellite are undertaken by the company GeoEye. After 20 days following the launch, the satellite reached its final orbit which is 705 km circular, noon, sun-synchronous. Data collection was enabled 30 days after the launch. Orbit determination is backed up by a redundant amount of global positioning system (GPS) receivers.

The SeaWiFS instrument is comprised of two parts: an optical scanner and an electronic module. The scanning mechanisms operate a spinning half-angle mirror and an off-axis folded telescope. The telescope spins at twice the speed of the mirror and the mirror is phase-synchronized with the telescope. The telescope, accompanied with the half-angle scan mirror setting, enables a design configuration that keeps the level of polarization at minimum beyond 58.3 degrees which is the maximum scan angle necessity.

The signals those are detected, and amplified, are directed to the electronic module from the scanner. This electronic module is the element where the signals are amplified even more strongly and then filtered for the purpose of noise bandwidth limitation (<http://oceancolor.gsfc.nasa.gov/seawifs/seastar/spacecraft.html>).

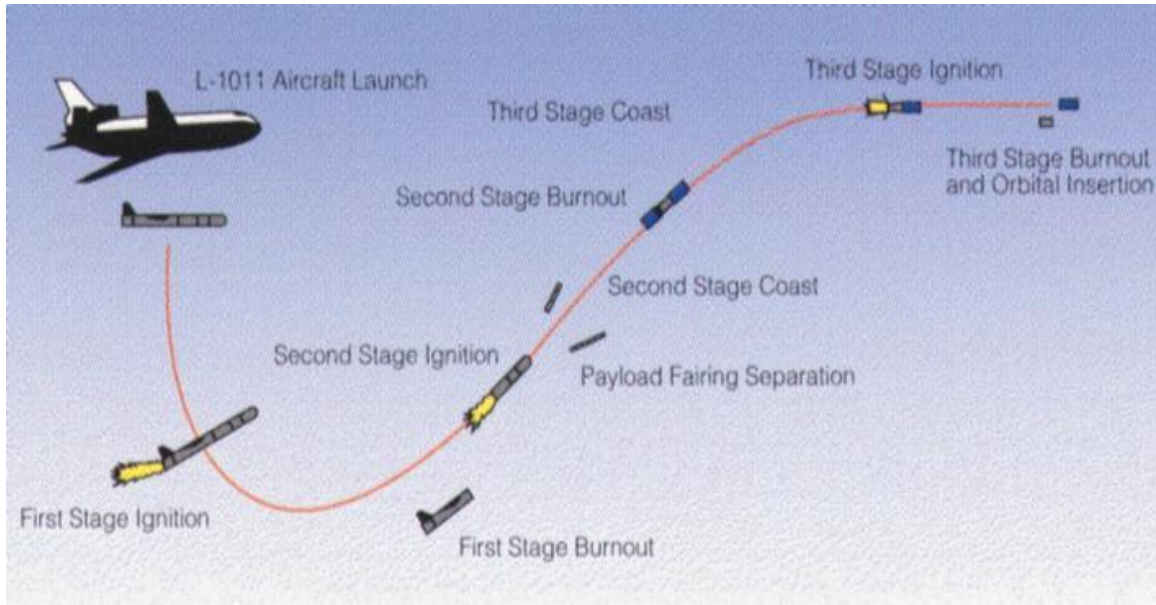


Figure 23. Launch diagram of SeaWiFS (From http://oceancolor.gsfc.nasa.gov/seawifs/seastar/seawifs_launch_diagram.jpeg)

Table 5. Mission Characteristics of SeaWiFS

Orbit Type	Sun Synchronous at 705 km
<i>Equator Crossing</i>	Noon+20 min, descending
<i>Orbital Period</i>	99 min.
<i>Swath Width - 1</i>	2,801 km LAC/HRPT (58.3 ⁰)
<i>Swath Width - 2</i>	1,502 km GAC (45 ⁰)
<i>Spatial Resolution</i>	1.1 km LAC, 4.5 km GAC
<i>Revisit Time</i>	1 day

C. QUIKSCAT

1. SCATTEROMETRY

a. Introduction

Scatterometers are airborne or space-borne microwave radar sensors that are designed to transmit a pulse of a microwave signal to the surface of the earth in order to measure the echoed microwave energy while scanning.

The main research area that space-borne scatterometry is used for has been primarily the near-surface winds over the ocean. These instruments are specifically called the wind scatterometers. They provide radar cross-sections of the surface accompanied by views of different azimuth angles, which help researchers better understand the near-surface wind vector that is present over the ocean surface when processed by a geophysical model function (GMF). GMFs provide information regarding the relationship between wind and backscattered energy. The radar echoes coming from the ocean surface are produced by wind-generated capillary-gravity waves which mostly correspond to the near-surface wind over the ocean. This scattering mechanism is called Bragg scattering (named after physicist Sir William Lawrence Bragg), and it results from waves that correspond with the microwaves.

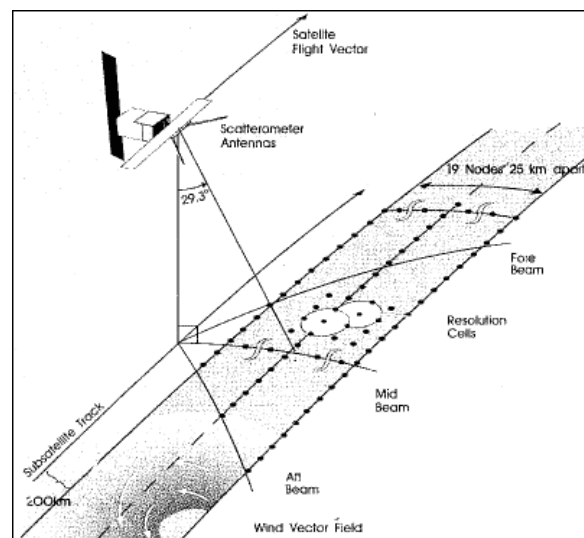


Figure 24. Principle of Scatterometer (From NOAA)

Wind speed and direction determines the backscattered power. This backscattered power from waves varies when observed from different azimuth angles. These variations lead to the process of the estimation and determination of sea surface wind speeds, which is known as wind retrieval.

Data obtained using ocean scatterometers are crucial to the research community, especially in the area of ocean circulation and air-sea interaction, and their influence on climate and weather patterns. Ocean scatterometers also enable the research of unusual phenomena, such as La Niña or changes that take place in polar regions over the long term. These data have also been used for the verification and justification of the outputs that are produced by the atmospheric, oceanic and coupled models, to improve modeling accuracy and increase the forecast period (<http://winds.jpl.nasa.gov/aboutScat/index.cfm>).

b. History

Information regarding the winds above the ocean surface used to come from irregular and mostly inaccurate reports from ships and buoys.

Scatterometry originated from early radar technology used in World War II. The measurements made by this early radar were found to be noisy, but that noise was discovered to be the signal response echoed from the surface winds. This relationship between the radar response and surface winds wasn't established until late 1960s.

Skylab missions in 1973 and 1974 were the first examples of space-borne scatterometry and they convinced the community that it is, in fact, beneficial and feasible to conduct scatterometry. Following those missions, the Seasat-A Satellite Scatterometer (SASS) was put into service in October 1978 and demonstrated that wind velocity can be measured from space accurately. European Space Agency's Remote Sensing Satellite (ERS-1) was the next mission in that category and a single-swath scatterometer was onboard of the spacecraft.

The NASA Scatterometer (NSCAT) had the privilege of housing the first dual-swath Ku-band. It was launched in August 1996 onboard of a Japanese Advanced

Earth Observing Satellite (ADEOS). Between the activation of the instrument in September 1996 and the termination of it due to a power loss in June 1997, NSCAT was very successful at collecting sea surface wind vector measurements. Due to this success, reliable data obtained through NSCAT led to a wide variety of applications, mostly addressing scientific and operational problems. To minimize the gap between scatterometry data, the schedule of the following QuikSCAT mission was accelerated and SeaWinds was launched by this mission in June 1999 (<http://winds.jpl.nasa.gov/aboutScat/history.cfm>).

2. MISSION

The goal of the QuikSCAT mission was to record wind speed and direction data near the sea-surface regardless of the condition of the weather or clouds. It was, indeed, a "quick recovery" mission intended to reduce the gap in ocean-wind vector data that resulted from the loss of the NSCAT on the ADEOS. QuikSCAT was launched from the Vandenberg Air Force Base in California onboard of a vehicle called Titan II. The QuikSCAT mission was conducted for NASA's Earth Science Enterprise by a division of the California Institute of Technology called the Jet Propulsion Laboratory (JPL). Other mission partners are listed in Table 6.

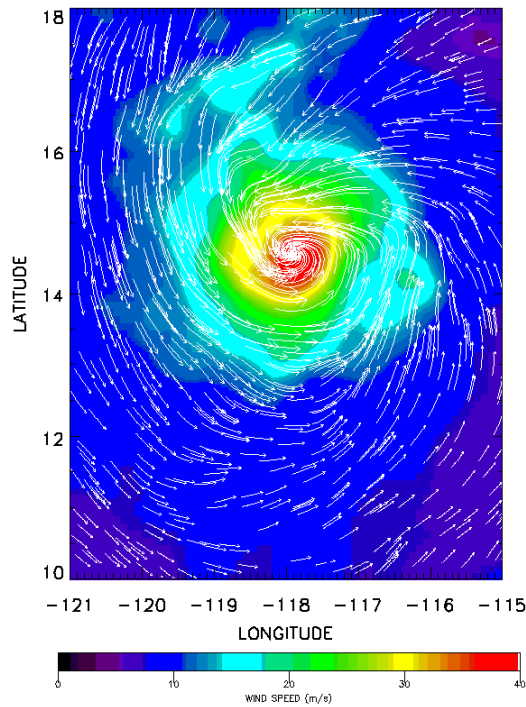


Figure 25. Hurricane Dora viewed from QuikSCAT (From JPL/NASA)

The orbit that QuikSCAT was designed to fly in was a circular, near polar orbit that was limited to a maximum altitude of about 800 km (500 miles) above Earth's surface. It accomplished a full orbit in around 101 minutes, which approximately corresponds to 14 orbits per day. SeaWinds, which is an active radar scatterometer, is the primary instrument on the QuikSCAT satellite. Each day SeaWinds makes around 400,000 measurements over ocean, land, and ice continuously with a 1,800-kilometer-wide band; it covers 90% of Earth's surface. With that capability, it makes hundreds of times more observations of the wind velocity on the Earth's surface every day than ships and buoys combined. SeaWinds, furthermore, is able to provide measurements of both velocity and the direction of the surface winds that are high-resolution, accurate, continuous, and which do not depend on weather conditions. Obtaining this data is crucial in terms of storm warning, global climate research, and many more different studies.

There were several ground systems involved in the QuikSCAT mission. The first types were Earth Polar Ground Stations that tracked the satellite. These stations were

located in Poker Flats, Alaska; McMurdo, Antarctica; Svalbard, Norway; Wallops Island, Virginia; and Hatoyama, Japan (the back-up station). The second type of ground system was where the data products were produced and distributed. These systems were the Jet Propulsion Laboratory (JPL) and NOAA. JPL was responsible for producing high-quality research data products and distributing them to the science community within two weeks of receipt. This distribution was made through the JPL Physical Oceanography Distributed Active Archive Center (Po.daac). NOAA, on the other hand, was responsible for producing operational data products for the international meteorological community in the within three hours of receipt.

Table 6. Mission Partners of QuikSCAT

National Oceanic and Atmospheric Administration (NOAA)
NASA Goddard Space Flight Center (GSFC)
Ball Aerospace and Technologies Corporation
U.S. Air Force Space and Missile Systems Center
Honeywell Satellite Systems Operations
Raytheon E-Systems Corporation
Lockheed Martin Astronautics
Hughes Electron Dynamics Division

QuikSCAT was in service until there was a mechanical failure of the spin mechanism of the antenna. Due to that failure, SeaWinds stopped rotating in November 2009. It didn't stop functioning completely, but its capability was significantly reduced. However, the collected data have still been setting the transfer standard for cross-calibration, and the standard for defining the measurement stability that is vital for continuity with scatterometer missions in the future. NASA and ISRO have agreed to allow the QuikSCAT team to have access to measurements taken by the Oceansat-2 scatterometer (OSCAT), which has been operating since September 2009. The partnership between NASA and ISRO was established as a long-term cooperation that enables direct cross-calibration of QuikSCAT with OSCAT to help in the generation of an ocean vector winds climate series (<http://winds.jpl.nasa.gov/missions/quikscat/#mission>).

THIS PAGE INTENTIONALLY LEFT BLANK

IV. METHODOLOGY

A. INTRODUCTION TO NEURAL NETWORKS

The discovery of the concept of neural networks is a captivating progress and a very important milestone. Frank Rosenblatt (1957) was the inventor of the first neural network for pattern classification. This network is called “Perceptron.” Thirteen years after its invention, Minsky and Papert (1969) published *Perceptrons*, which called enormous attention to neural network research. The concept of neural networks was formalized and demonstrated in this book as well as discussing a few of its serious limitations concerning the original architecture (Noyes 1992). To be more specific, Perceptron, in this publication, is proved to be unable to execute a basic logical computation of an exclusive-or (XOR). That disability was found to be a crucial drawback at first, yet research continued, and as a result, the concept of neural networks has become a popular tool to provide solutions to complicated problems (Fitzpatrick 1997; Guthikonda 2005).

The neural networks approach involves modeling the biological brain with the assistance of Artificial Intelligence’s brain-paradigm. The methodology is novel as it compares the previous computer science concepts, especially in terms of data storage. Typical programs tend to store the data in solid structure types and, eventually, the data is stored in a centralized database. Neural networks, on the other hand, distribute the information throughout the network (Noyes 1992; Guthikonda 2005). In other words, they resemble the biological brain.

Neural networks attract many researchers and individuals around the world due to their promising capability to solve complex problems. They can be extremely fast as well as efficient. Such features enable the handling of large data sets (Noyes 1992). The reason underlies this capability is that each node contributing to a neural network is fundamentally self-governing. Therefore, only a small portion of the total computation in the problem’s grand-scheme is performed by each node. The strength lies in the aggregation of the computational power of all the nodes in the entire network. This

special design, which imitates the biological brain, makes parallel multitasking feasible. Another advantage of neural networks is that they are tolerable against fault (Noyes 1992). This means that a limited portion of corrupted data, or a limited number of nodes that exhibit malfunction or do not even function at all, will not paralyze the whole network. Under these circumstances, the network figures out a way to perform reasonably even with these faults because it is able to learn. This feature, too, is inspired by the biological brain since we know that even if the order of the words change, we are still able to understand a sentence (this sentence with misspelled words is set up intentionally to prove that the statement is true) (Guthikonda 2005).

Before delving into the learning capability of neural networks, the definition of learning should be stated clearly. Learning can be defined in two ways depending on different categories: biologically and mechanically. Biological learning is detailed as an experience which causes alteration in an organism's state and improves its performance in consecutive similar situations. Mechanical learning, on the other hand, is defined as a computational approach taken in order to achieve new intelligence and organize that intelligence in order to acquire new abilities (Noyes 1992). In light of these two definitions, it can be assumed that a neural network must have the ability to learn in order to be considered useful. Training of neural networks leads to learning, which eventually enables this learning to be applied for practical purposes (Guthikonda 2005).

A different way to categorize the learning process is to take control on the data into account. Admittedly, there are two kinds of learning in this regard: supervised learning and unsupervised learning [Egge98]. In supervised learning, the accurate answers are known and the main purpose is to train the network to respond to a given situation with respect to these accurate answers. Input vectors benefit from supervised learning as well as output vectors. Once the output vectors are obtained, they are used together with the input vectors to analyze the performance of the network and to locate any errors. Reinforcement learning, for instance, is a specialized supervised learning method, which only provides the information of whether or not the output is accurate; it is based on the back-propagation algorithms (Guthikonda 2005).

In unsupervised learning, whereas, it is either the accurate answers are not available in advance or the accurate answers are not shared with the network beforehand. The input vectors are handled separately. The output vectors have no contribution to the learning process, unlike in supervised learning. The network must perform as a self-governed system and must extract the patterns of the input data itself without an interaction of any kind, especially human interaction. Supposedly, this is a crucial feature since it is time-consuming and sometimes it is not even possible for a human to make the computations by him or herself when working on large and complicated data sets. Unsupervised learning is the kind of learning utilized by self-organizing maps (Guthikonda 2005).

B. THE SELF-ORGANIZING MAPS

1. INTRODUCTION

Self-organizing maps were first described by Tuevo Kohonen in 1982. “Self-organizing” comes from the fact that they are autonomous and supervision is not demanded. SOMs have the ability to learn by themselves using competitive learning. “Maps” refers to the way they handle the given input data sets, which is by attempting to map weights of the data. The nodes of the SOM network try to resemble the input data sets they are initially given and this reaction of the nodes, essentially, sets up the foundation for the whole learning process. Preserving the main and important characteristics of the input data sets constitutes the fundamental principle of SOMs, and this principle is what makes the SOMs special in comparison to other methods. Retaining the topological relationships among the input data and, mapping these relationships to an SOM network are very valuable aspect of representing complex data sets (Guthikonda 2005).

2. STRUCTURE

SOMs have a fairly simple structure, which is illustrated in Figure 26.

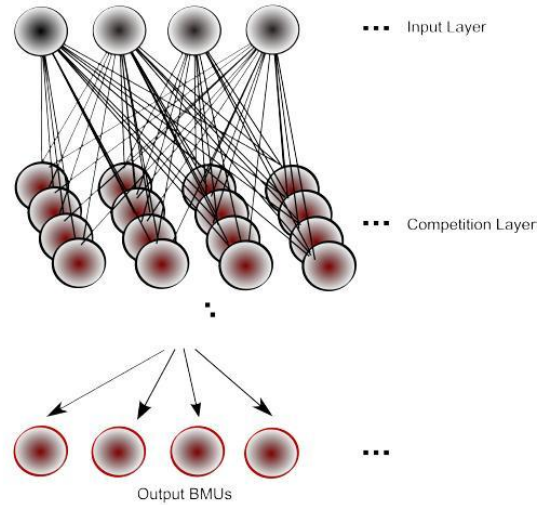


Figure 26. Illustration of the structure of a SOM (From Maung 2012)

A 4 x 4 SOM network is shown in Figure 26 as the competition layer. There are a few aspects of the structure that are worth mentioning. First of all, each input node has a connection with each map node. Even for a small network (as in Figure 26) that corresponds to a large number of connections. For example, in the Figure 26 network, 4 times 4 times 4 equals 64 connections. Unlike the relationship between input nodes and map nodes, notice that there is no connection between map nodes in the network. The organization of the nodes is a two dimensional grid, which, as mentioned earlier, provides an easy way to visualize the outputs. This type of structure is also helpful when using the SOM algorithm. Each node in the network is denoted with a unique coordinate (i, j) . This unique coordinate system provides an easy way to refer to a node in the network and to determine the ranges between nodes. The map nodes do not know the values that their neighbors hold due to the fact that each only has connections with the input nodes. Therefore, each node must use the information given by the input vectors in order to update its own weights. The weight vectors of both the map nodes and the input vectors should match to enable the algorithm to perform properly (Guthikonda 2005).

3. ALGORITHM

As an unsupervised learning algorithm, SOM has learning and prediction phases. During the learning phase, map is built; network organizes using a competitive process with a training set. During the prediction phase, new vectors are quickly given a location on the converged map, easily classifying or categorizing the new data. Vector quantization, which is a data compression technique, is the other crucial property of SOMs. SOMs reflect multi-dimensional data sets on a lower dimensional space; in most cases, SOMs reflect these data sets on two dimensions (Buckland 2003). This provides a user-friendly and easy-to-visualize representation of the complex data and enables a user to work on the data even more efficiently (Guthikonda 2005). The algorithm of the self-organizing map can be described as six main steps (Buckland 2003). These steps that the algorithm utilizes are outlined in Table 7 (Guthikonda 2005).

Table 7. Main six steps of the algorithm of the SOM

1st Step	Each node's weight is initialized with a random number between 0 and 1.
2nd Step	A random vector is selected from the training data set and introduced to the network.
3rd Step	Each node in the network is inspected in order to find out which one resembles the input vector more accurately in terms of weights. Best Matching Unit (BMU) is the name given to the winning node. The Euclidean distance formula, which measures the similarity between two data sets, is used in order to do this selection. The BMU is found by the calculation of the distance between the weights of node and the input vector. (as shown in Equation 1).
4th Step	The radius of the neighborhood of the BMU is calculated. This radius is initialized as the network's radius and decays with each time-step until reaching the BMU itself (as shown in Equations 2a and 2b).
5th Step	All of the nodes that fall in the radius of the BMU are adjusted in order to make them as similar as possible to the input vector (as shown in Equations 3a and 3b). The weight of the closest node to the BMU is changed the most, and the degree of this change diminishes as the range between the BMU and the nodes increases (as shown in Equation 3c).
6th Step	The second step is repeated for N iterations.

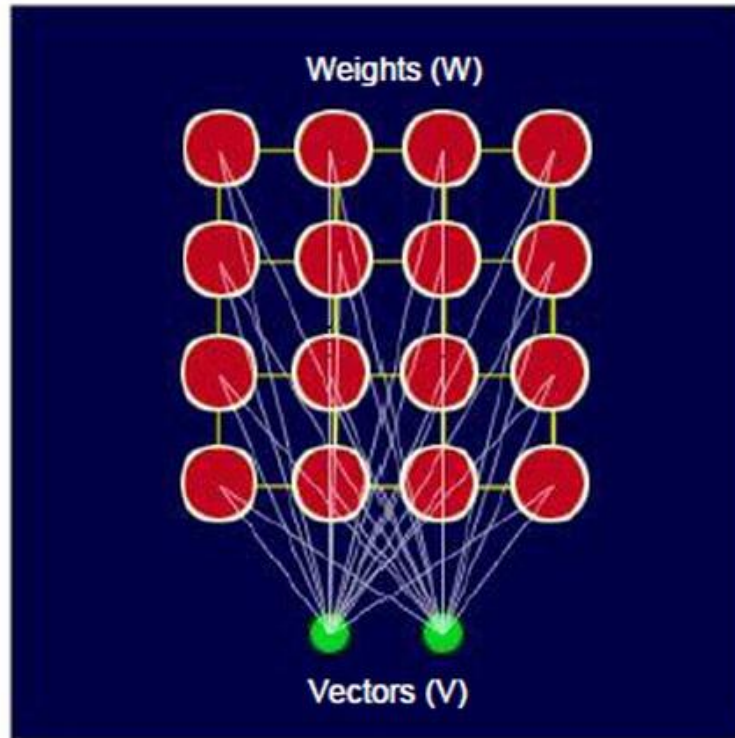


Figure 27. A two-dimensional illustration that shows the same type of connection of each node with the input vectors. Note that there is no connection among the nodes
 (Available from http://www.saedsayad.com/clustering_som.htm)

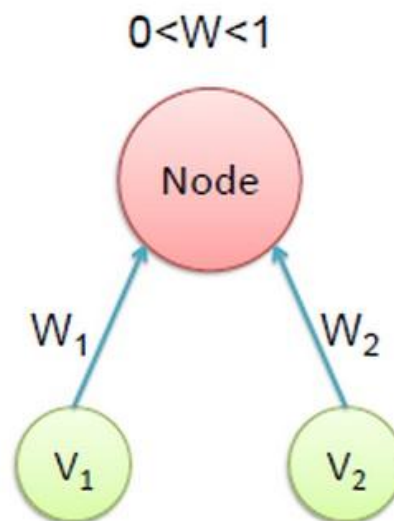


Figure 28. An illustration that shows the initialization step of each node's weights
 (From http://www.saedsayad.com/clustering_som.htm)

The observational (input) vector $\mathbf{V} = (v_1, v_2, \dots, v_n)$ is compared to the node's weight vector $\mathbf{W} = (w_1, w_2, \dots, w_n)$. The distance (or difference) between the two vectors is computed by

$$D = \sqrt{\sum_{i=0}^n (v_i - w_i)^2}, \quad (1)$$

The optimal placement of the weight vectors $\mathbf{W}(j)$ is obtained from the minimization of the distance,

$$D_c = \min_j \{D_j\}, \quad (2)$$

which is called the best matching unit (BMU). The BMU neighborhood is determined as follows. The size of the neighborhood is represented by an exponential decay function that shrinks until eventually the neighborhood is just the BMU itself. The width of the lattice at iteration t (see Figure 29) $\sigma(t)$ is calculated by

$$\sigma(t) = \sigma_0 \exp\left(-\frac{t}{\lambda}\right), \quad (3)$$

where σ_0 is the width of the initial lattice; λ is a constant. The new weight for a node is the old weight, plus a fraction (L) of the difference between the old weight and the input vector, adjusted (θ) based on distance from the BMU,

$$\mathbf{W}(t+1) = \mathbf{W}(t) + \theta(t)L(t)[\mathbf{V}(t) - \mathbf{W}(t)], \quad (4)$$

where $L(t)$ is the learning rate at the iteration t ,

$$L(t) = L_0 \exp\left(-\frac{t}{\lambda}\right), \quad (5)$$

with L_0 the initial learning rate; and $\theta(t)$ is the Gaussian curve for the neighborhood,

$$\theta(t) = \exp\left[-\frac{D^2}{2\sigma^2(t)}\right], \quad (6)$$

so that nodes that are closer are influenced more than farther nodes. As iteration advances, it is observed that, under the influence of this formula, a given node weight

becomes much more similar to the input vector that is selected. The bigger the initial difference between a node and selected input vector, the more iteration is spent to train the node and vice versa. That difference is then scaled by two different aspects: the SOM's current learning rate and $\theta(t)$ (Guthikonda 2005).

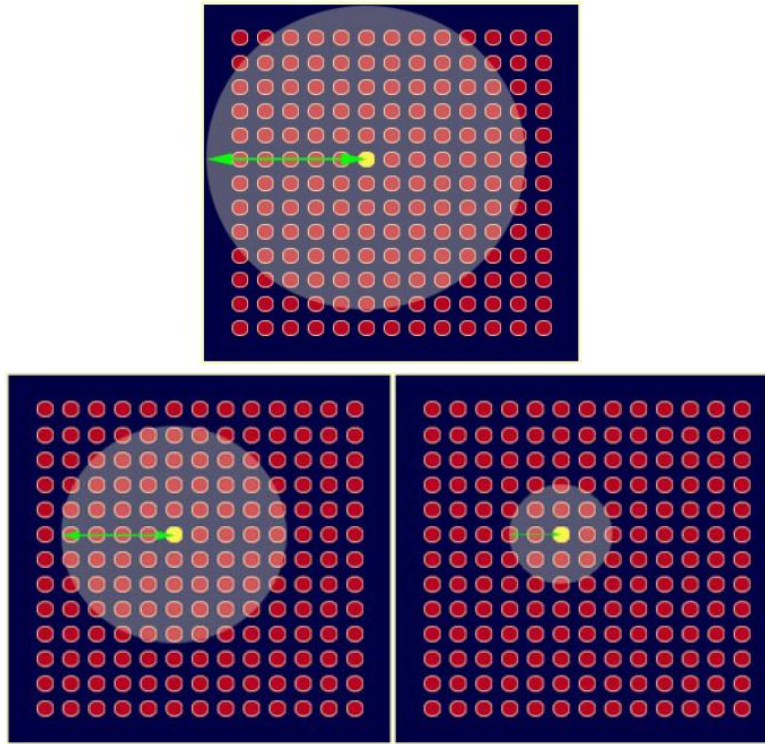


Figure 29. An illustration of the process utilized by Equation 2a (From Guthikonda 2005)

The degree of influence that the node's distance from the BMU has on the node's learning is shown by the influence rate. Initially, influence rate is set to 1 for all the neighboring nodes of the BMU and zero for the ones that are away from the BMU. At the end, due to weights' random distribution and numerous iterations, SOM is able to settle down to a map of stable zones (http://www.saedsayad.com/clustering_som.htm). Nodes that do not fall into the neighborhood radius are entirely ignored. The term "distFromBMU" represents the exact number of nodes that are located between the BMU and the given node. The formula used to calculate that particular information is:

$$\text{distFromBMU}^2 = (\text{bmuI} - \text{nodeI})^2 + (\text{bmuJ} - \text{nodeJ})^2, \quad (7)$$

The fact that the network is composed of nodes that are on a two-dimensional grid makes the calculation possible. The amount learned by the nodes on the edge of the neighborhood radius is a fractional value that is smaller than 1.0. Clearly $\Theta(t)$ has a tendency to near 1.0 if the term “distFromBMU” becomes smaller. In terms of the BMU, its value for “distFromBMU” will be zero; this enables $\theta(t)$ to reach its maximum value, which in this case is 1.0 (Guthikonda 2005).

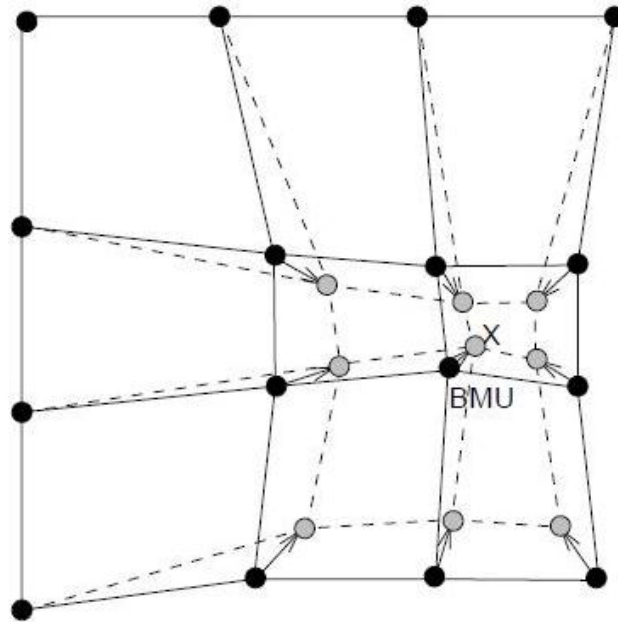


Figure 30. An illustration of the process of updating BMU along with its neighbors towards the “x,” which in this case is the input sample (From Vesanto et al. 2000)

The equations adopted within the SOM algorithm vary significantly from one study to another. Besides that, the biggest debate seems to be regarding the optimal parameters. Questions concerning the sufficient amount of iterations, the learning rate, and the width of the neighborhood radius have still not been answered clearly. The recommendation of Kohonen in this matter is to set up a training which has two altered phases. During the first phase, the learning coefficient will start with 0.9 and decrease to 0.1. The neighborhood radius, on the other hand, will start with half of the lattice’s diameter and decrease to the closest surrounding nodes. In the second phase, however,

the learning rate will start with 0.1 and decrease to 0.0; the iteration will be doubled in comparison with the first phase. The value for the neighborhood radius remains as 1, which encompasses the BMU only. In the light of these descriptions, Matthews (2004) remarks that the first phase can be denoted as “rough tuning,” which enables a quick order; and the second phase can be denoted as “fine tuning,” which assures a precise representation (Guthikonda 2005).

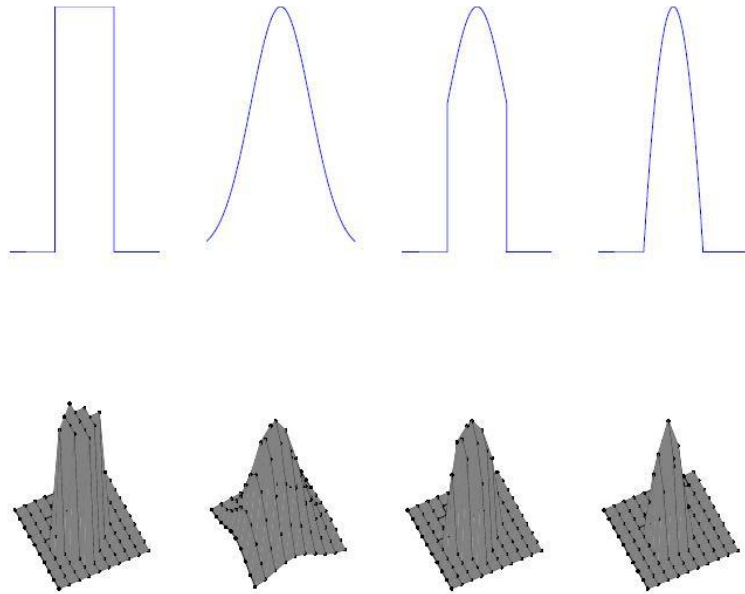


Figure 31. An illustration of the differences among the four neighborhood functions. They are, from left to right, “bubble,” “gaussian,” “cutgass,” and “ep.” The first row is a one-dimensional representation, whereas the second row is two-dimensional (From Vesanto et al. 2000).

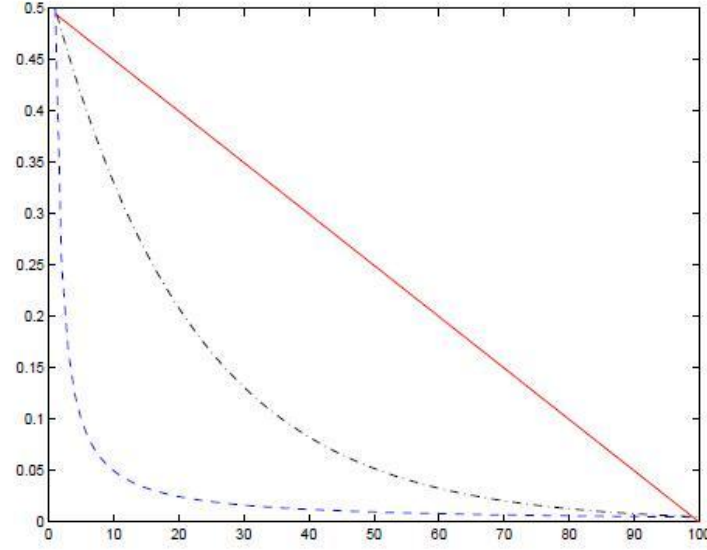


Figure 32. An illustration of the differences among the three functions of learning rate. *inv* is represented as a dashed curve, *power* is represented as a dot-dashed curve, and *linear* is represented as solid line (From Vesanto et al. 2000).

4. DAVIES – BOULDIN INDEX

The Davies–Bouldin index (DBI)

$$DBI = \frac{1}{N} \sum_{i=1, i \neq j}^N \max \left[\frac{\sigma_i + \sigma_j}{d(c_i, c_j)} \right], \quad (8)$$

is exerted to the data sets along with the SOM, to determine the number of patterns that best represents a data set. DBI was introduced by David L. Davies and Donald W. Bouldin in 1979, and is a measure that is used for assessing clustering algorithms. DBI operates as an internal scheme, and the authentication of how precise the clustering has been accomplished is made using characteristics of the data set (Davies and Bouldin 1979). In the formula; N is the number of clusters; σ_i is the average distance of all patterns in cluster i to their cluster centers c_i ; σ_j is the average distance of all patterns in cluster j to their cluster centers c_j ; and $d(c_i, c_j)$ is the distance between cluster centers c_i and c_j . Small values of DBI correspond to clusters that are compact, and whose centers

are far away from each other. Consequently, the number of clusters that minimizes DBI is taken as the optimal number of clusters.

5. TOOLBOX FOR MATLAB

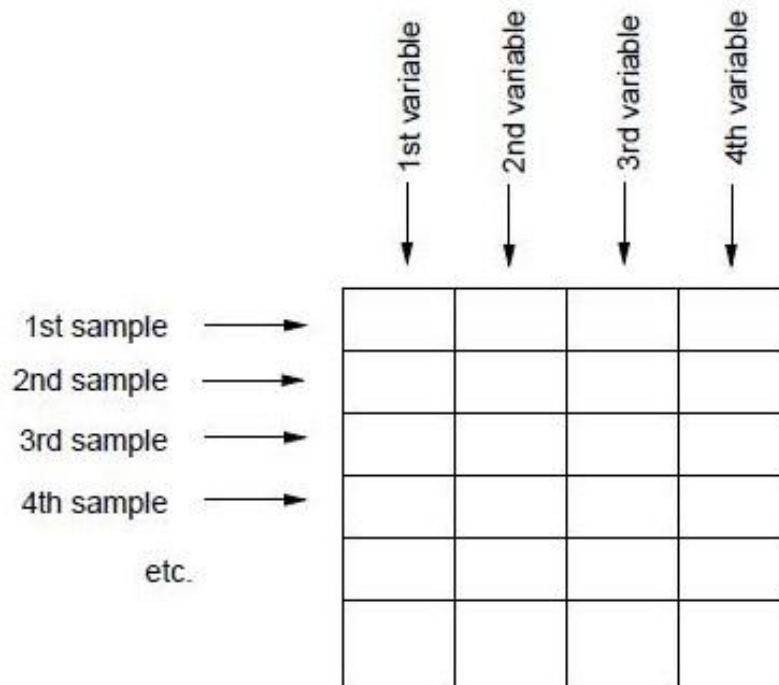


Figure 33. An illustration of the table format of the data (From Vesanto et al. 2000)

The Toolbox can perform with a particular form of data which is called table data or spreadsheet. Table's each row represents a data sample and is composed of the variables of the data set. These variables can symbolize different aspects of the data set such as an object's properties or measurements taken at a given time. The crucial rule governing this type of data organization is that samples in the organization must share the same type of variables. This rule assures that each column of the table includes all values for a single variable (Vesanto et al. 2000).

Either symbolic data or numeric data can be processed with the Toolbox, yet the SOM algorithm only allows for the usage of numeric data. Furthermore, the order of the

objects with respect to the values they contain must be meaningful, as well. This means that if it is assumed that a table is comprised of three objects, the distance between the first and the second object must be less than the distance between the second and third objects (Vesanto et al. 2000).

String labels of the data samples can be used to house symbolic data in the Toolbox, which enables users to utilize these data as personal notes for a given sample in case a user needs to remember something about the sample or s/he needs to assure a property of that entity. These labels, however, will not be recognized by the SOM algorithm as mentioned before. Pyle (1999) proposes that, if these labels are aimed to be processed in the training algorithm, conversion methods such as 1-of-n coding or mapping can be used (Vesanto et al. 2000).

C. COMPARISON WITH OTHER CONVENTIONAL METHODS

There are two major methods often preferred when identifying patterns of variability in oceanic data and meteorological data: the Empirical Orthogonal Function (EOF) and Principal Component Analysis (PCA). Liu and Weisberg tested both EOF and SOM in 2005 and 2007 in order to detect patterns of ocean currents using the exact same data set. Data was obtained through a moored Acoustic Doppler Current Profiler (ADCP) and contained a long velocity time series. The results favored SOM as researchers found that patterns from the leading mode EOF were less intuitive and less accurate compared to the SOM patterns. More specifically, non-symmetric features regarding coastal jet location, current strength, and veering of the velocity vector with respect to depth that takes place between the current patterns of upwelling and downwelling were detected by the nonlinear SOM, whereas data on these features couldn't be revealed by the linear EOF (Liu and Weisberg 2005; Liu and Weisberg 2001).

In another experiment, SOM and EOF were compared as each method's extraction of an artificial data that represents known patterns was tested. This time both SOM and EOF were found to be successful at extracting the patterns of a sine wave that is linear and progressive, but SOM was also successful when noise was added to the data. On the other hand, when the experiment was carried out using multiple data sets

concerning more complex patterns, the EOF technique failed to detect all patterns in contrast with the SOM method which was successful (Liu et al. 2006a; Liu and Weisberg 2001).

Reusch et al. (2005) used synthetic data sets that contained both negative and positive modes of four sea level pressure fields of the North Atlantic that are idealized, in order to test PCA method against SOM. Test is executed twice; adding and disregarding noise components. At the end, SOM was found to be more robust in comparison to PCA in terms of the extraction of the patterns of variability that are predefined. Astel et al. (2007) and Annas et al. (2007) also tested PCA method against SOM, and they both confirmed that SOM has a higher performance over the PCA (Liu and Weisberg 2001).

Another artificial neural network widely used and preferred in terms of clustering is K-means. Bação et al. (2005) compared the K-means method against SOM, and came up with the idea that SOMs can substitute K-means clustering algorithms. Lin and Chen (2006) carried out another test to compare the clustering accuracy among the SOM, Ward's method and the K-means method. The data used in this test are experimental data sets that features are known and under control in terms of cluster membership and cluster dispersion. SOM method, one more time, found to be more accurate in specifying the cluster membership compared to Ward's method and K-means method (Liu and Weisberg 2001).

V. SURFACE CURRENTS

The geostrophic velocity data from 1992 to 2012 were obtained from AVISO to provide data on the surface currents. Their monthly means show the seasonal variation of the surface currents. Six patterns were found after conducting the SOM. The inter-annual variability of the surface currents was also obtained. Different time frames were selected and examined throughout the initial analyses. A ten-year-long data set was found to be sufficient when extracting the patterns of the long-term temporal and spatial variation due to the fact that any data sets covering a period longer than 10 years do not affect the results. Therefore, this research focuses on data sets from 1999 to 2009.

A. MONTHLY MEAN SURFACE CURRENTS

The monthly average of January surface currents is shown in Figure 34. As shown in the figure, many eddies with various sizes are evident. The Batumi and the Sevastopol eddies, both of which are anti-cyclonic, are the most pronounced eddies during this month. The weak, cyclonic Suchumi eddy takes place north of the Batumi eddy. During this particular time of the year, the Caucasus eddy seems immature, but there is a tendency of anti-cyclonic circulation. Off of the Kerch Strait, the well-organized, anti-cyclonic Kerch eddy is detected. Unlike these other regions, the western shelf basin is not rich in terms of eddies. Apart from the Sevastopol eddy, the anti-cyclonic Bosphorus eddy is present. Additionally, the northerly western boundary current is distinctive. Due to the abundance of eddies, it is hard to identify the RIM current, but the general circulation seems to have two main gyres: the western and eastern gyres.

In Figure 35, the climatological average of the surface currents for February is presented. Most of eddies that existed in January disappear in February. The anti-cyclonic Sevastopol and Batumi eddies still exist yet they are weaker, while the northerly western boundary current is not detected. The main western and eastern gyres are observed in terms of general circulation.

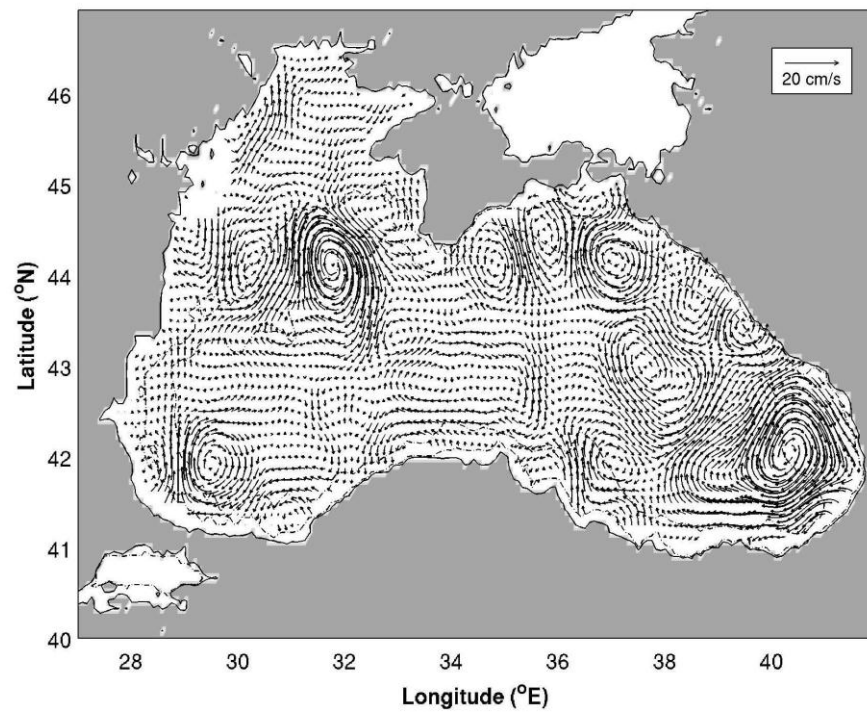


Figure 34. The climatological average of the surface currents for January

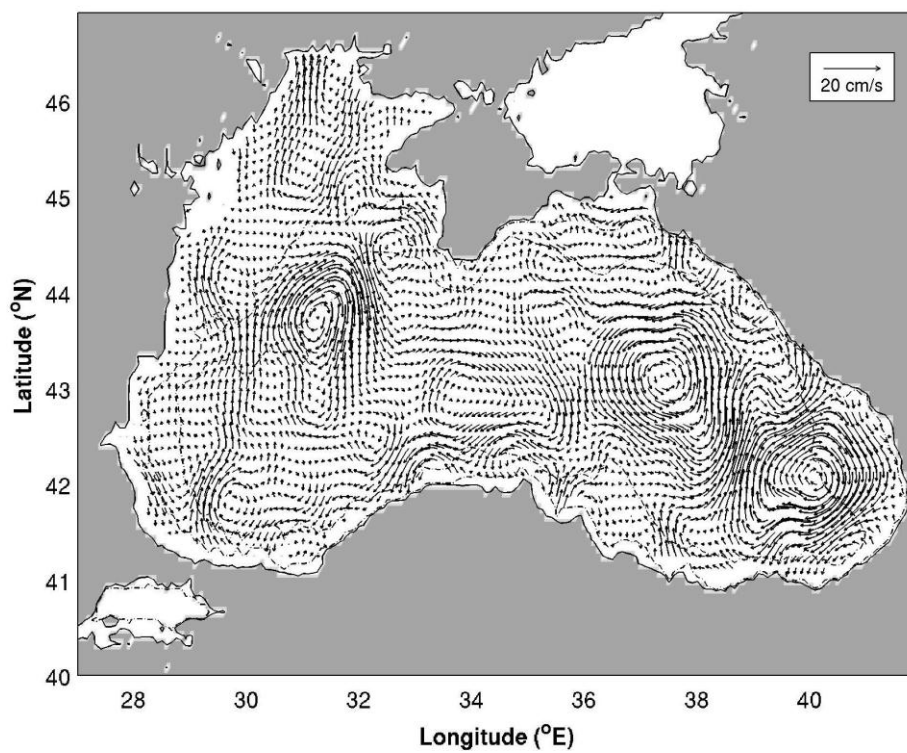


Figure 35. The climatological average of the surface currents for February

In March, a Batumi dipole eddies is detected in the Batumi eddy region. The Suchumi eddy appears to be in an immature stage, but there is a tendency of cyclonic circulation. The Sevastopol eddy demonstrates a weak cyclonic circulation. The general circulation of the basin is comprised of two main gyres, with the eastern gyre being more pronounced (see Figure 36).

The whole basin exhibits chaotic circulation patterns in April. The Sevastopol eddy disappears and the same Batumi dipole eddies is evident in the Batumi eddy region. The western main gyre is anti-cyclonic whereas the eastern main gyre is cyclonic. Both main gyres are strong during this period (see Figure 37).

In May, the Batumi dipole eddies in the southeastern basin starts detaching from the coast and gets weaker, as does the anti-cyclonic Caucasus eddy. A strong, northerly boundary layer arises in the southeastern part of the basin. During this time of the year, both the western and eastern main gyres are cyclonic and well-defined (see Figure 38).

In June, the whole basin is dominated by eddies with various sizes and strength. The Batumi dipole eddies in the Batumi eddy region detaches completely from the coast and moves to the north. Two small cyclonic eddies are evident in the Sevastopol eddy region and the Sakarya eddy begins to develop (see Figure 39).

Two cyclonic main gyres are evident during July. The Bosphorus eddy is detected at its developing stage. The Batumi dipole eddies in the southeastern part of the basin disappears and the Batumi eddy appears as a single eddy structure. The Sevastopol eddy seems to be included into the Western main gyre. The southerly and northerly boundary layers are formed in the western and eastern parts, respectively (see Figure 40).

The general circulation is formed by an elongated cyclonic single loop called the RIM current in August. Although there are regions showing a tendency of a circular motion, the only well-pronounced eddy is the cyclonic Batumi eddy. The anti-cyclonic tendency next to the Batumi eddy is considered a sign of the birth of the Suchumi eddy (see Figure 41).

The cyclonic RIM current persists in September, as well. During this time of the year the Batumi eddy seems to get stronger and wider. Meanwhile, the Sevastopol eddy is

still not evident and continues to be part of the general circulation. Neither major nor minor eddies are detected in the open basin (see Figure 42).

In October, the Batumi eddy gets stronger and moves to the southeastern corner of the basin. The elongated single loop structure appears to be dissolved and two-main-gyre structure starts to take over again. During this time, the eastern main gyre is stronger than the western main gyre. The Kerch and the Caucasus eddies start to develop in the northeastern part of the basin (see Figure 43).

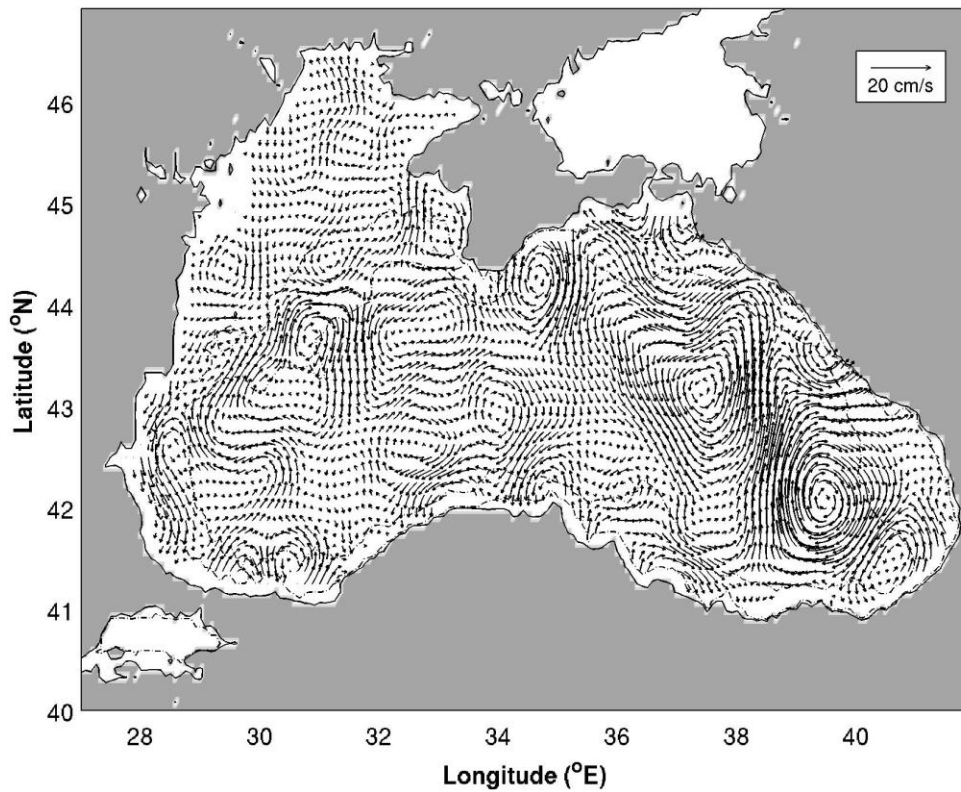


Figure 36. The climatological average of the surface currents for March

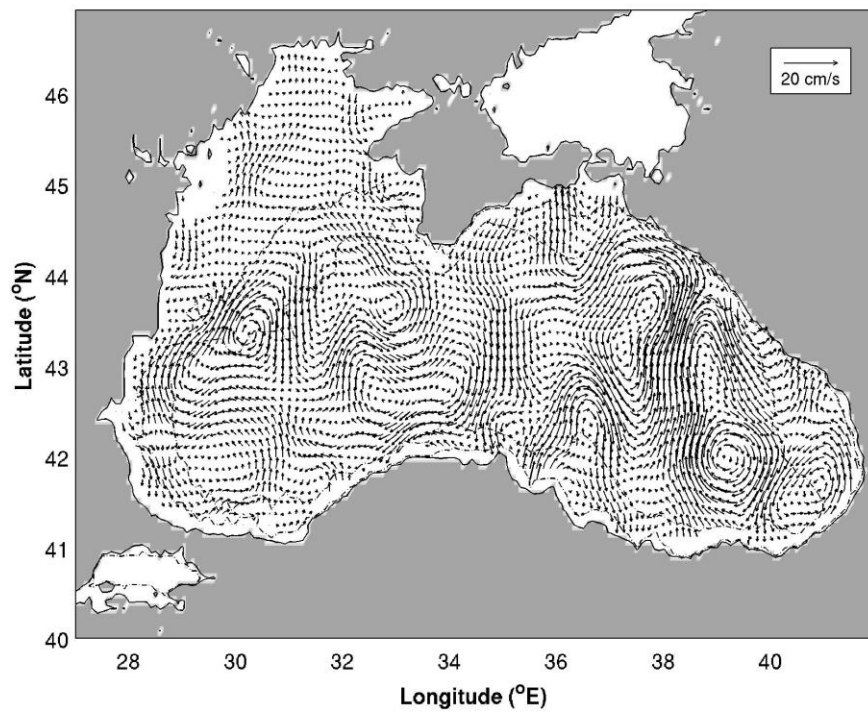


Figure 37. The climatological average of the surface currents for April

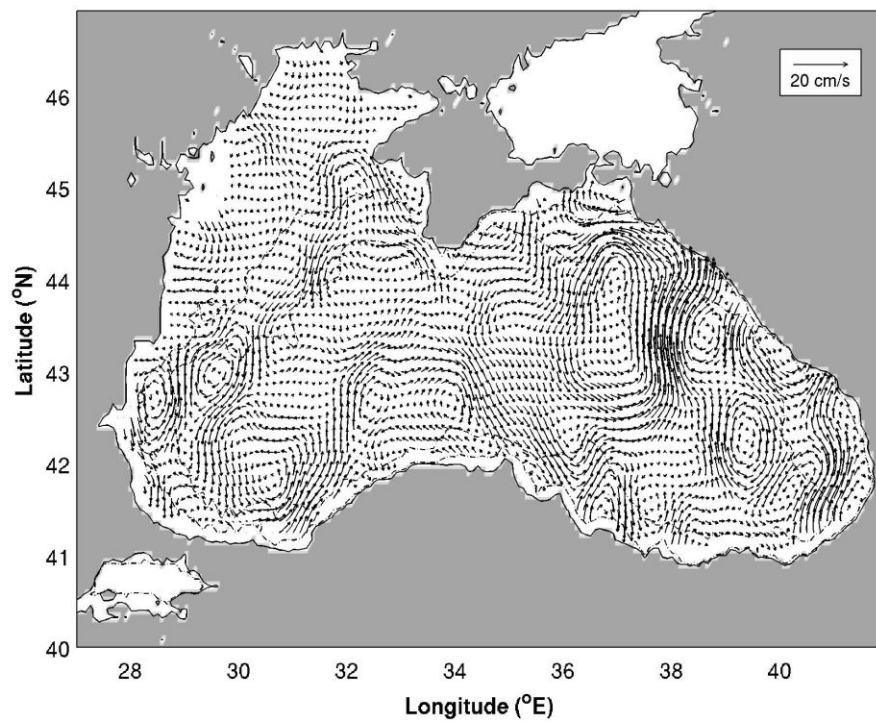


Figure 38. The climatological average of the surface currents for May

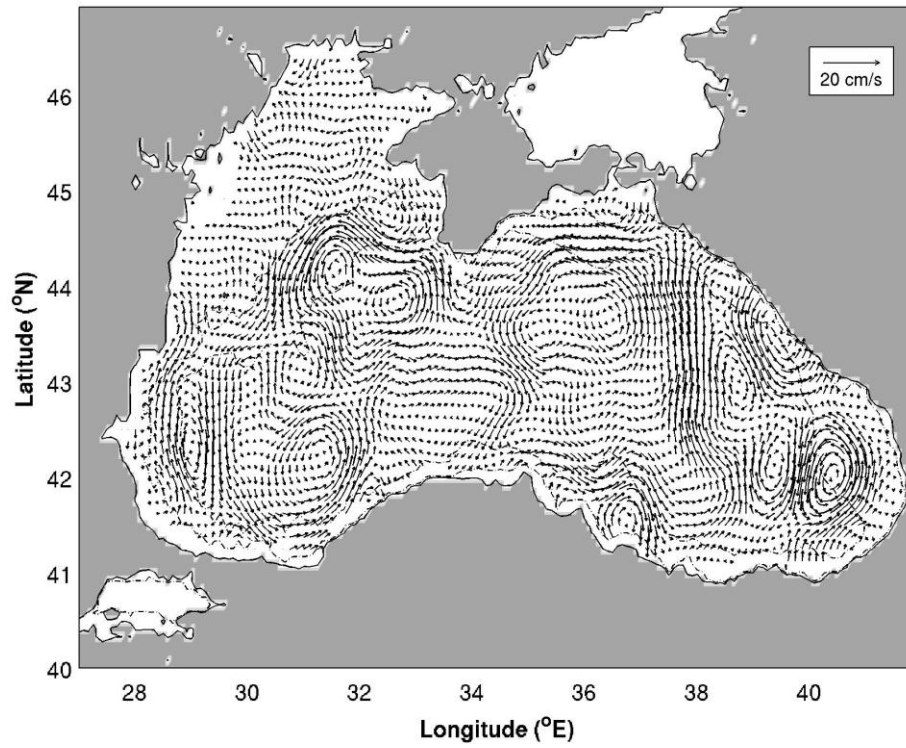


Figure 39. The climatological average of the surface currents for June

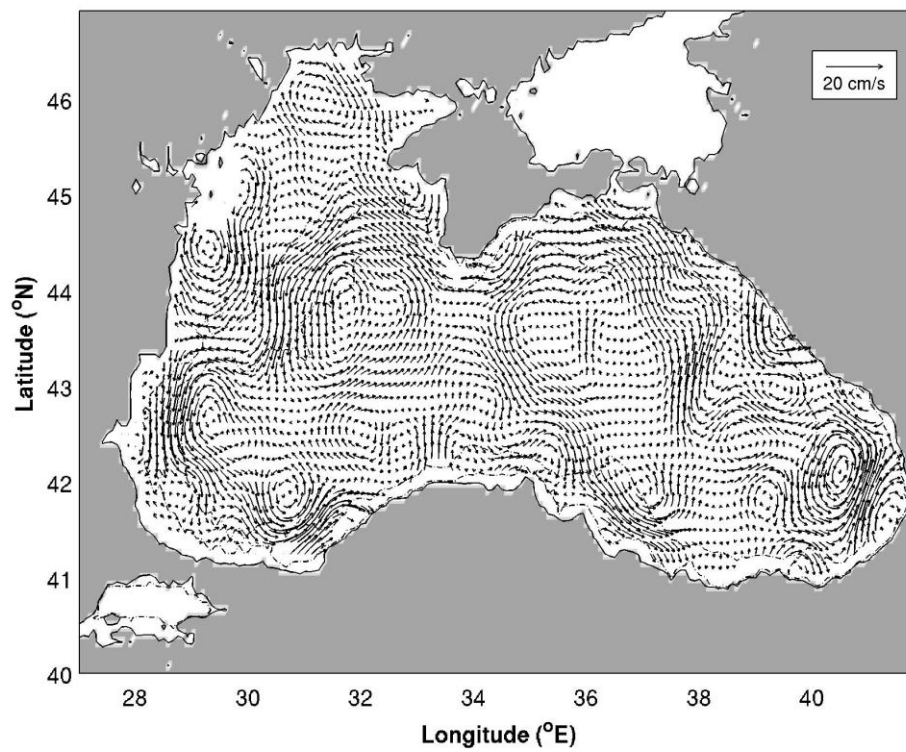


Figure 40. The climatological average of the surface currents for July

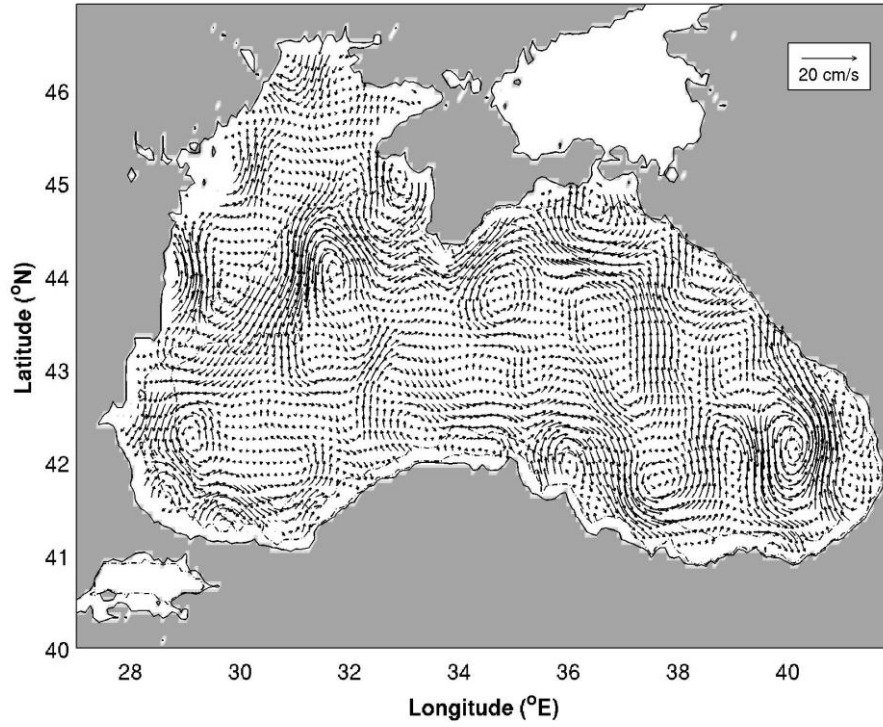


Figure 41. The climatological average of the surface currents for August

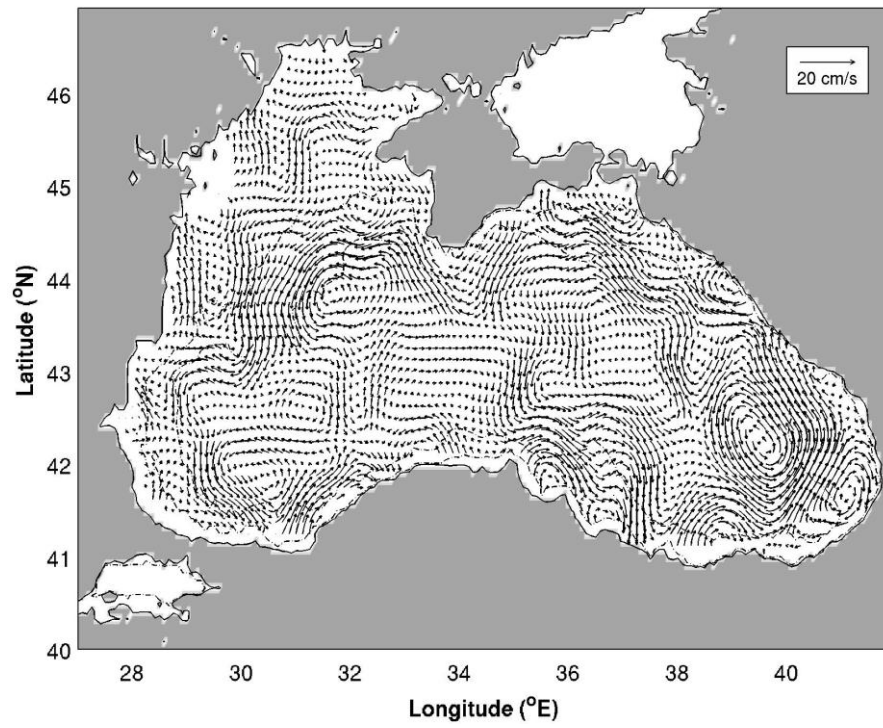


Figure 42. The climatological average of the surface currents for September

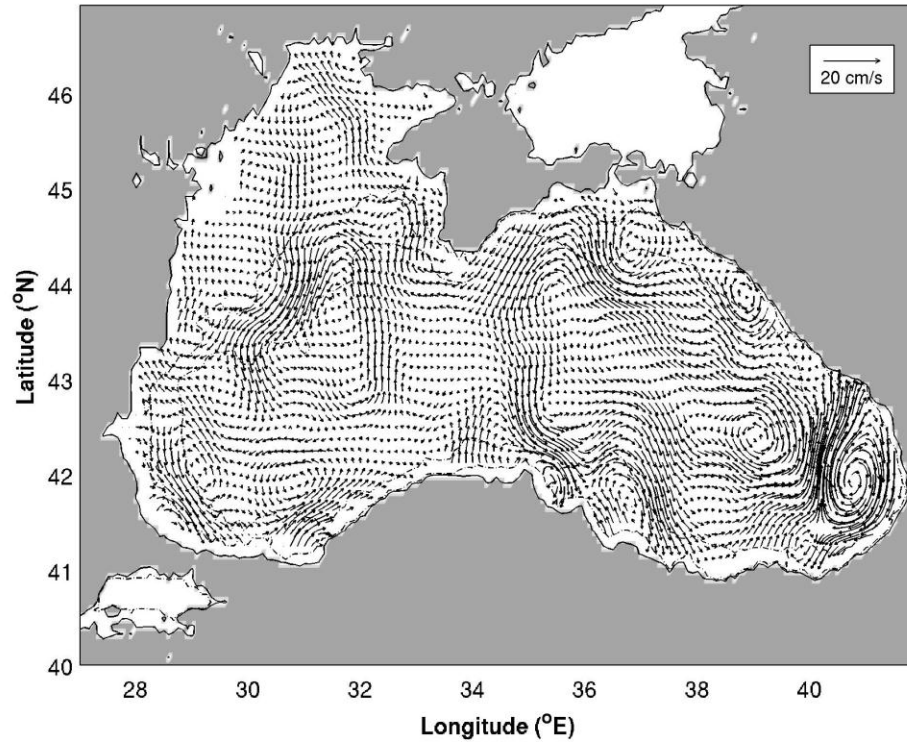


Figure 43. The climatological average of the surface currents for October

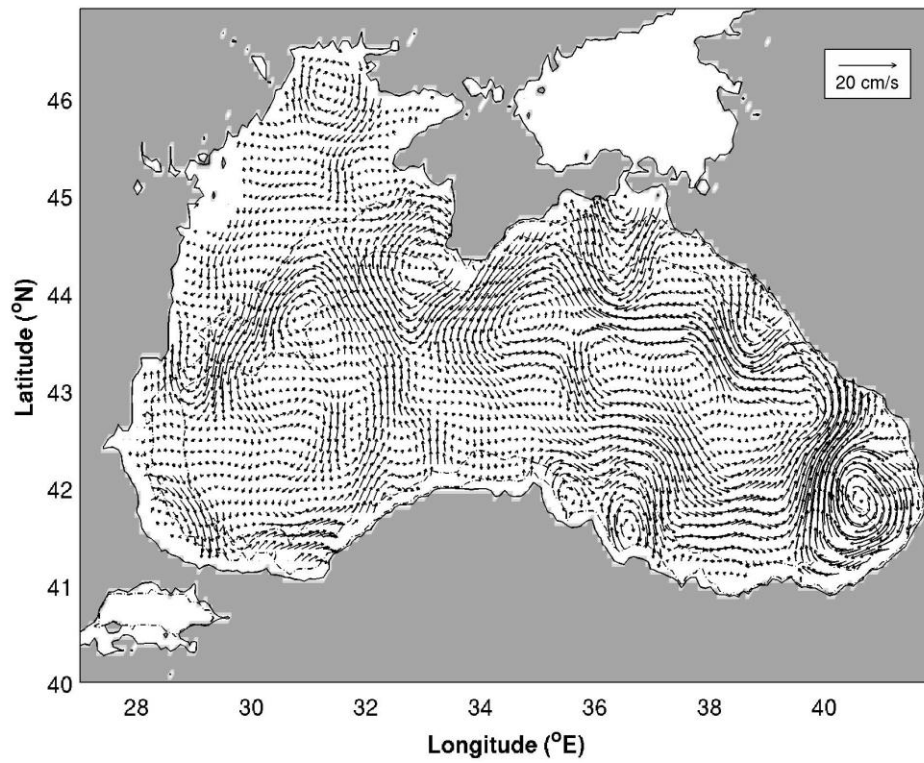


Figure 44. The climatological average of the surface currents for November

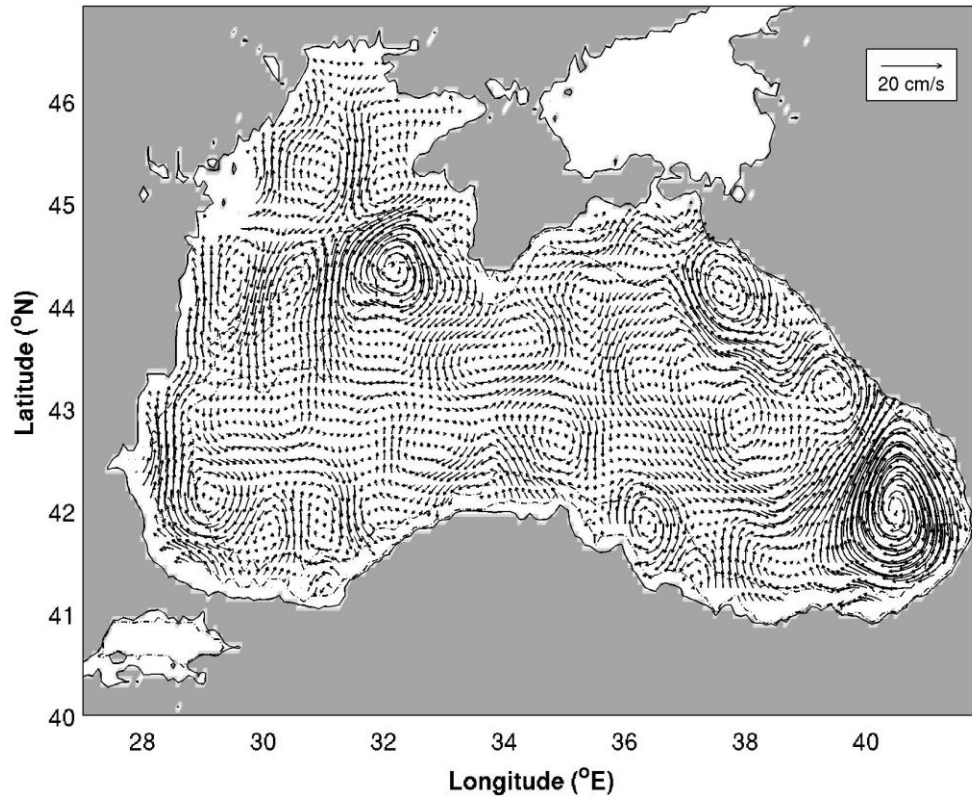


Figure 45. The climatological average of the surface currents for December

During the month of November, the Batumi eddy increases its strength, affecting a larger area in the southeastern corner of the basin. Meanwhile, the two-main-gyre structure persists. Both main gyres are strong and cyclonic during this time of the year. In November the Sevastopol eddy disappears completely and, in the southern region, the Kizilirmak eddy starts to develop (see Figure 44).

In December, the anti-cyclonic Batumi eddy is at its maximum strength. In the northwestern region the Sevastopol eddy forms again and rotates anti-cyclonically. The main gyres are very weak on both sides of the basin. In the northeastern and eastern regions, the Kerch eddy and the Suchumi eddy, respectively, develop (see Figure 45).

B. TEMPORAL AND SPATIAL VARIABILITY

To study the temporal and spatial variation of the surface currents, the Black Sea basin is subject to iterative SOM analysis. The DBI demonstrates the best option with regards to the selection of total number of clusters to represent the whole data set. The smaller the DBI, the better and more practical the data representation is. Therefore, in light of the DBI, the SOM analysis for the surface currents is based on six clusters (see Figure 46).

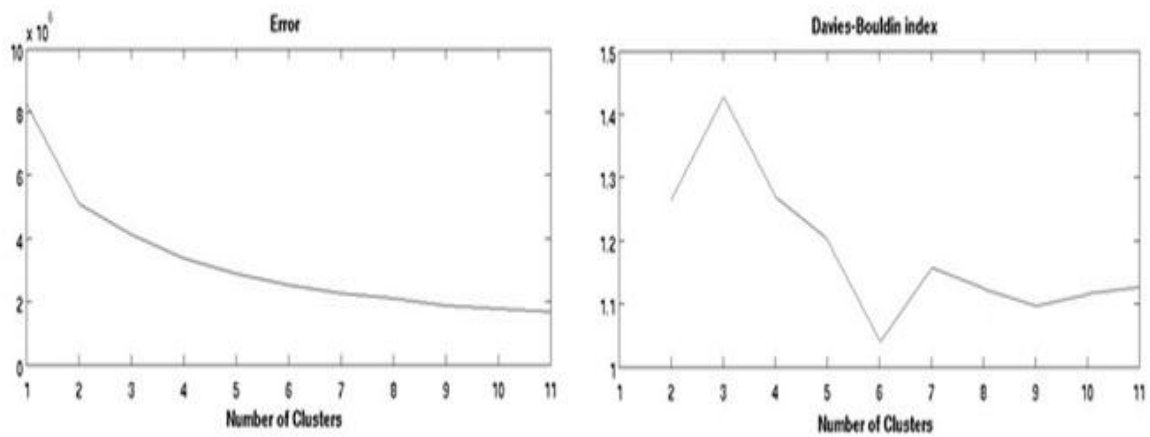


Figure 46. The Davies-Bouldin index results concerning the geostrophic velocity data set

1. SIX PATTERNS

a. *Pattern 1: Sevastopol Cyclonic and Batumi Dipole Eddies*

The first pattern represents more than 20% of the whole data set. In this pattern, the Batumi dipole eddies are detected at the southeastern corner of the basin. The eddy on the right is strong, cyclonic, and it spins at ~ 8 cm/s, whereas the other eddy is weak and anti-cyclonic. At the northwestern corner of the basin, the cyclonic Sevastopol eddy which spins at ~ 5 cm/s is evident. The general circulation is comprised of two main gyres. The western main gyre is anti-cyclonic and weak. The eastern main gyre, on the other hand, is cyclonic and strong. The northerly boundary current forms in the west. No eddy formation is observed in the open parts of the basin (see Figure 47).

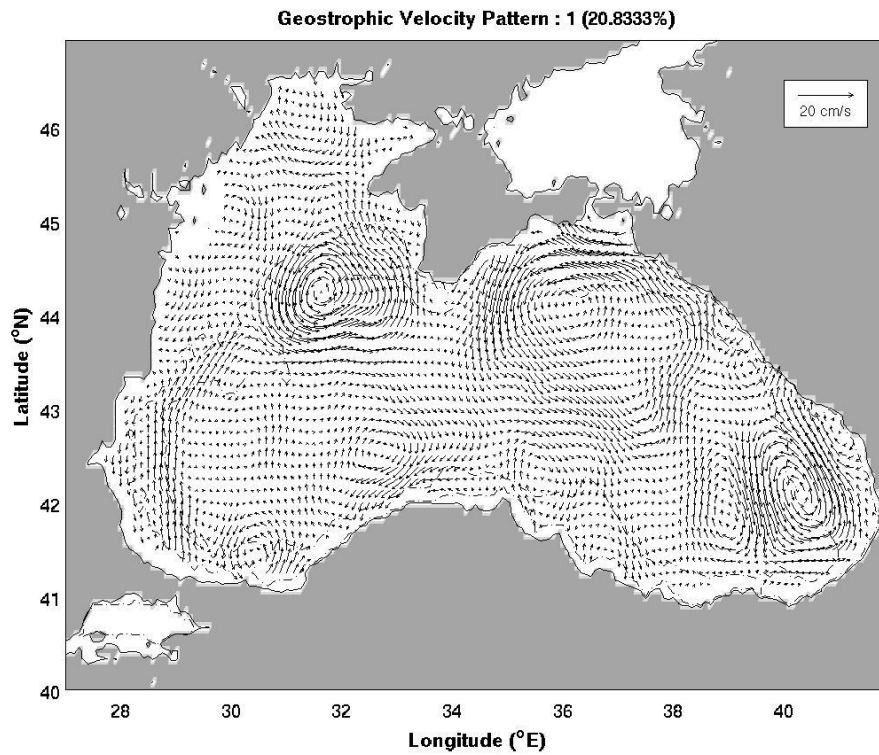


Figure 47. The first pattern of the surface currents and its percentage

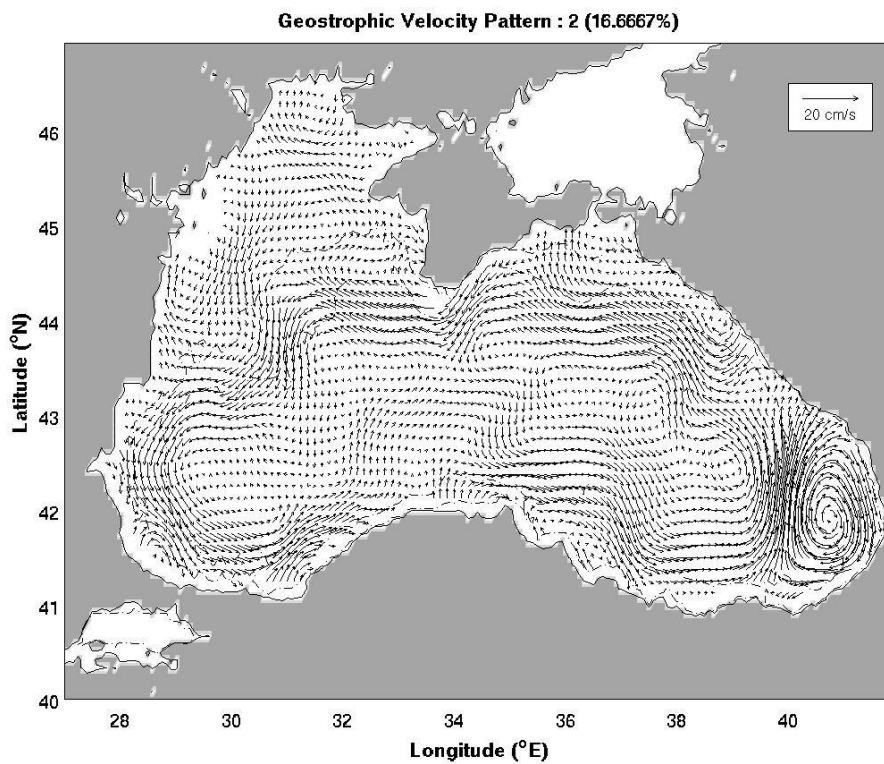


Figure 48. The second pattern of the surface currents and its percentage

b. Pattern 2: Cyclonic RIM Current and Anti-cyclonic Batumi Eddy

More than 16% of the data set is represented by the second pattern. The main feature of this pattern is the strong, anti-cyclonic Batumi eddy spinning at ~8 cm/s. Apart from the Batumi eddy, no other eddy structure, including the major Sevastopol eddy, is observed. The general circulation is formed by the strong and cyclonic RIM current flowing at ~5 cm/s. The open parts of the basin are relatively calm as opposed to the coastal regions. Therefore, this particular pattern is mostly dominated by the RIM current (see Figure 48).

c. Pattern 3: Anti-cyclonic Sevastopol and Batumi Eddies

The third pattern also represents almost 16% of the whole data set. The major eddies of the basin are the Batumi and Sevastopol eddies which spin at ~7-8 cm/s. Both of these major eddies are strong and anti-cyclonic. The RIM current does not appear which means that the general circulation is formed by the western and eastern main gyres. In the northeastern corner, the weak Caucasus eddy exists, while the strong northerly boundary current is present in the west (see Figure 49).

d. Pattern 4: Cyclonic RIM Current and Batumi Eddy

The fourth pattern comprises more than 20% of the whole representation of the data set. In this pattern the Black Sea basin is almost entirely dominated by the strong cyclonic RIM current which flows at ~10 cm/s. The open parts of the sea stay relatively calm and the very weak cyclonic Batumi eddy is detected but it is nearly absorbed by the RIM current (see Figure 50).

e. Pattern 5: Anti-cyclonic RIM Current and Batumi Dipole Eddies

The fifth pattern represents 15% of the whole data set and it demonstrates a basin-wide, chaotic environment. At the southeastern corner the Batumi dipole eddies take place and the stronger eddy spins at ~7 cm/s. The weak, anti-cyclonic Crimea eddy is observed in the north, whereas the Sevastopol eddy disappears. The general circulation is formed by the strong, anti-cyclonic RIM current which flows at ~6-7 cm/s (see Figure 51).

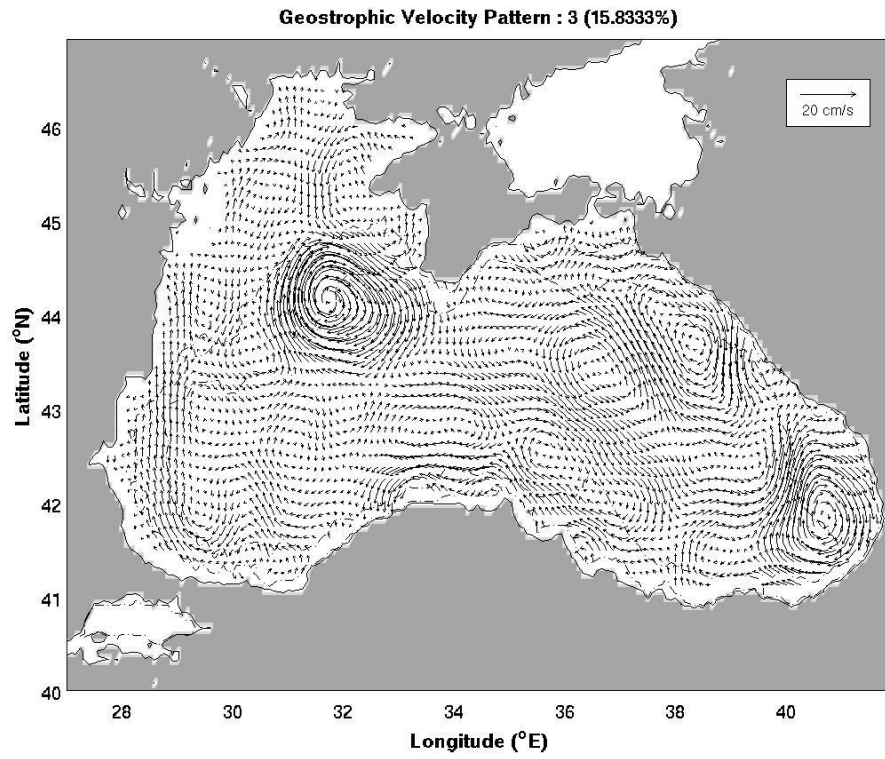


Figure 49. The third pattern of the surface currents and its percentage

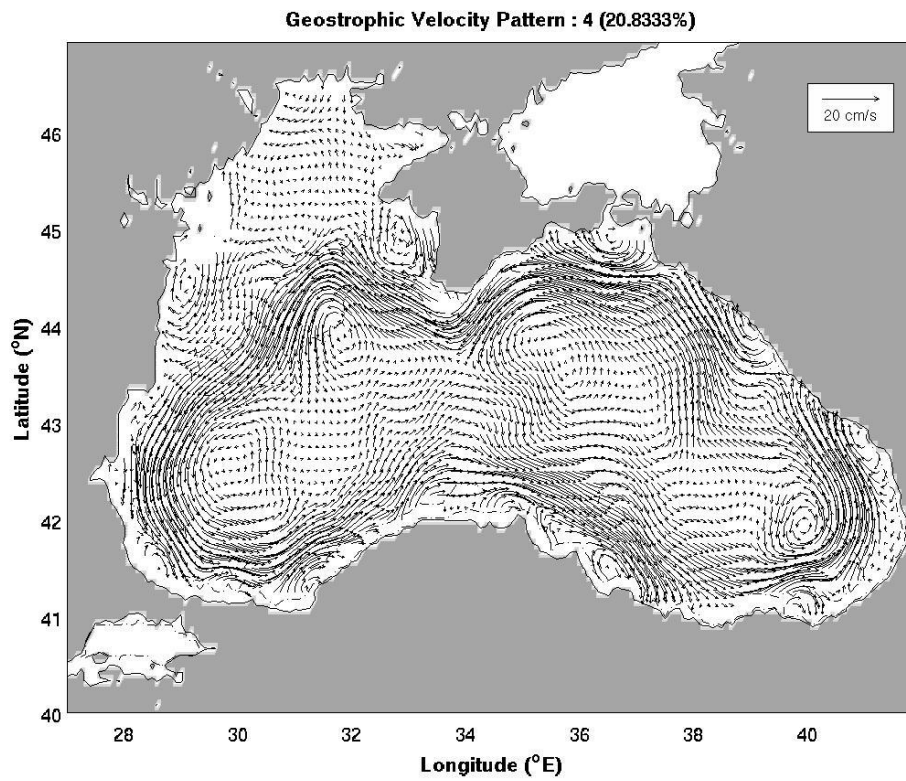


Figure 50. The fourth pattern of the surface currents and its percentage

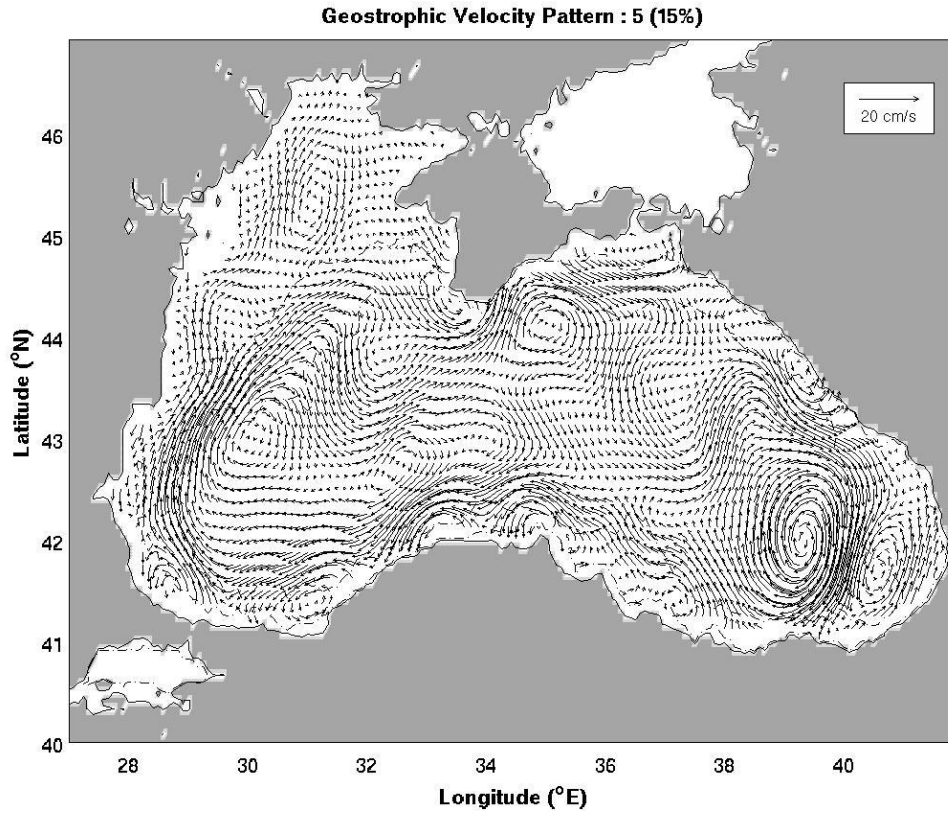


Figure 51. The fifth pattern of the surface currents and its percentage

a. Pattern 6: Anti-cyclonic RIM Current and Multi Eddies

More than 10% of the total representation for the data set is covered by the sixth pattern. The southeastern corner of the basin is entirely dominated by the strong, anti-cyclonic Batumi eddy spinning at ~ 8 cm/s. At the north of the Batumi eddy, the cyclonic Suchumi eddy is detected. The weak, anti-cyclonic Kerch eddy is observed in the north. At the northwestern corner the strong anti-cyclonic Sevastopol eddy forms, which spins at ~ 6 cm/s. The general circulation is comprised of the strong, anti-cyclonic RIM current (see Figure 52).

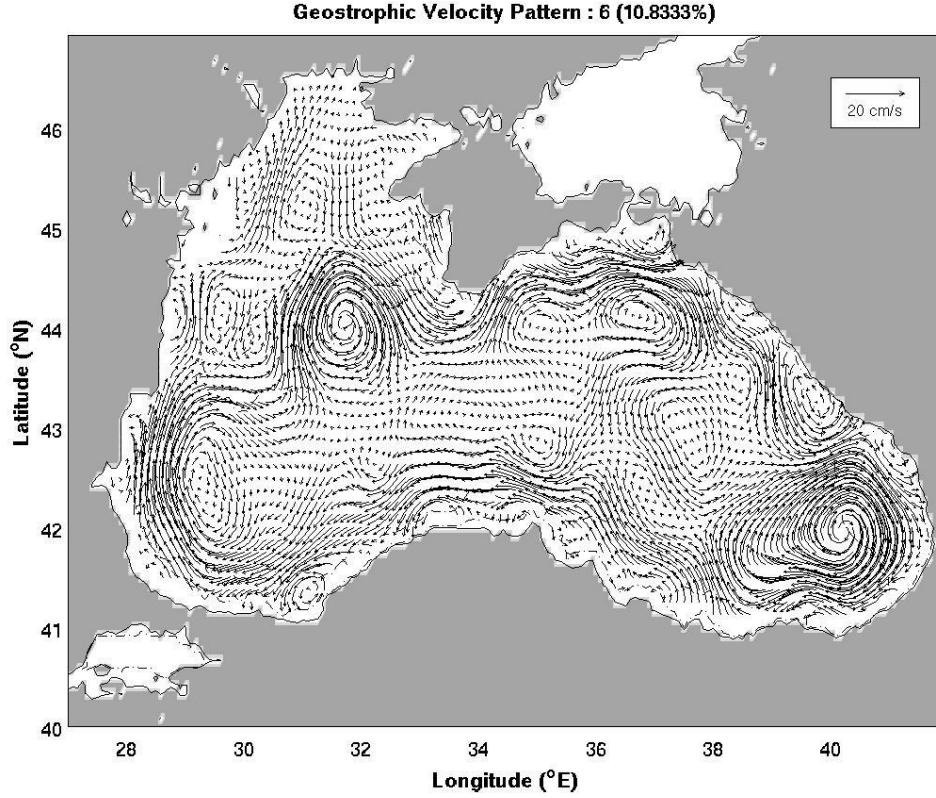


Figure 52. The sixth pattern of the surface currents and its percentage

2. VORTICITY FEATURES

The 33.7° E longitude is taken to divide the Black Sea into eastern and western parts. The spatially averaged Pattern- i relative vorticity (ζ_i) and enstrophy (E_i) for the two parts are calculated:

$$\zeta_E^{(i)} = \frac{1}{S_E} \iint_{S_E} \zeta_i dxdy, \quad \zeta_W^{(i)} = \frac{1}{S_W} \iint_{S_W} \zeta_i dxdy, \quad (9)$$

$$E_E^{(i)} = \frac{1}{2S_E} \iint_{S_E} \zeta_i^2 dxdy, \quad E_W^{(i)} = \frac{1}{2S_W} \iint_{S_W} \zeta_i^2 dxdy, \quad (10)$$

where the subscript ‘ E ’ means the East Black Sea, and ‘ W ’ indicates the West Black Sea. The enstrophy, basically, describes how the fluid acts to dissipate energy in terms of The The enstrophy, basically, describes how the fluid acts to dissipate energy in terms of kinetic energy. In a mechanical problem, this would be like how friction acts to slow down movement (velocity) because it dissipates energy. The averaged enstrophies over

the six patterns for the east and West Black Sea were calculated, and the differences of each pattern versus the average were taken as the anomalies relative to the mean enstrophies. Figure 53 shows the scatter diagrams of each pattern in terms of the East and West Black Sea relative vorticity and enstrophy anomaly.

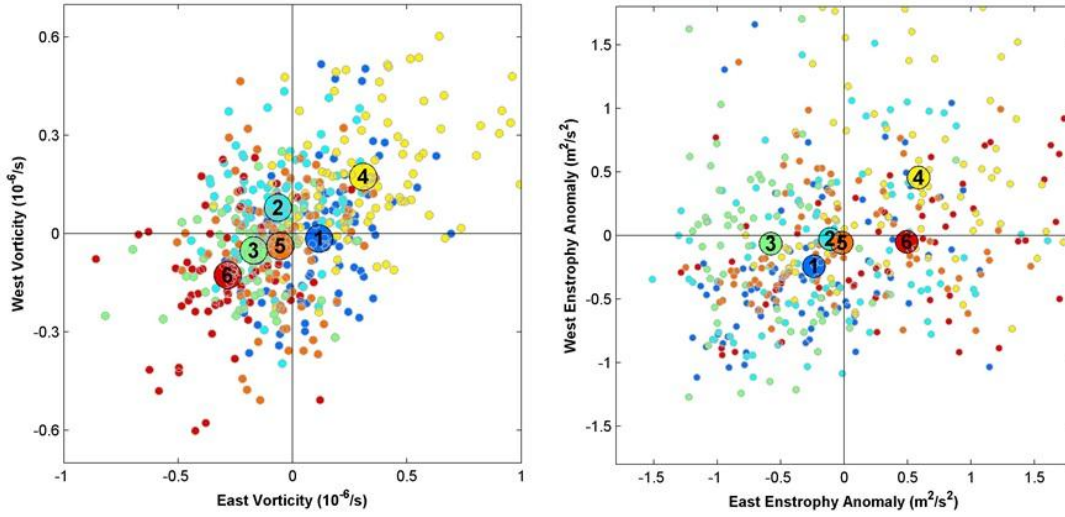


Figure 53. Horizontally averaged East and West (a) relative vorticity, and (b) enstrophy anomaly values of the six patterns of the surface currents

3. TEMPORAL VARIATION

To better illustrate the monthly and seasonal variability of the surface currents, the rate of occurrence of the six patterns was computed and the results are shown in Figure 54. Pattern 1 is one of the two patterns that dominate during winter-like and fall-like months. Its maximum contribution is in January with $\sim 45\%$ and it disappears completely in June. Even though there is less than a 35% chance it will appear, it is the pattern most likely to be observed in December. Pattern 2 is more likely to be observed during the spring. Its maximum contribution is detected in April with more than 50% and it has the highest percentage among the six patterns in this particular month. In summer and fall it tends to stay at around 20%, it declines in winter-like months, and it completely disappears in June. Pattern 3 tends to appear towards the end of the spring and the beginning of the summer. It reaches its maximum in May and becomes the pattern most likely to appear during that time of the year. It demonstrates an oscillation during

fall-like months and never shows up in January and February. The first three months of the year are dominated by the Pattern 4. It tends to appear strongly during cold periods, whereas during warm periods it exhibits a weak contribution. Pattern 4 disappears in May and doesn't appear again until September. Despite the fact that Pattern 5 shows maximum percentages in fall-like months and dominates in October, it has no significant seasonality and occurs occasionally throughout the year. Pattern 6 completely disappears from November to April, and appears only five months during the year. It dominates the period from June to September and reaches its maximum in July. With more than 40% contribution, it becomes the pattern most likely to be detected in July.

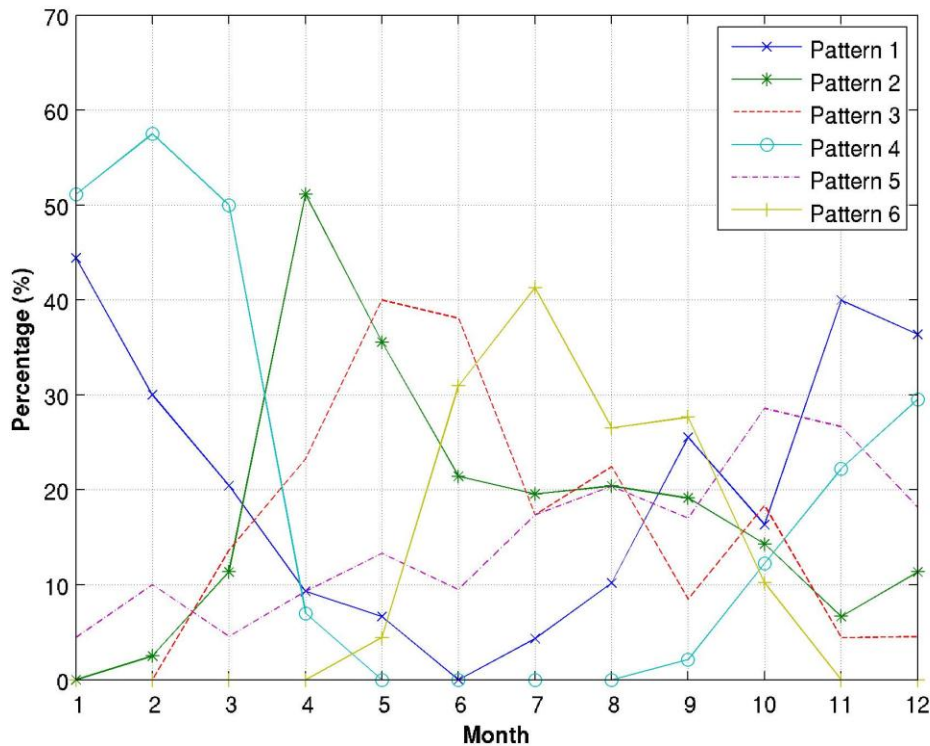


Figure 54. Monthly percentage of the six patterns of the surface currents

The time series of the six patterns of the surface currents from 2000 through 2009, with one year overlap, that was derived by SOM is shown in Figure 55 and the evolution of the duration and the frequency of the same patterns is shown in Figure 56 in order to

illustrate the inter-annual variability. Furthermore, Figure 57, Figure 58, and Figure 59 demonstrate the contemporaneous EAWR, NAO, and ENSO indices respectively, along with the times series of the surface currents. In addition to those figures, Table 9 is provided to allow a deeper understanding of the relationship between the surface currents and the large-scale teleconnection indices.

The potential influence of large-scale teleconnection indices on the recurrent patterns of the surface currents (shown in Figures 47-52) are evaluated by estimating for each recurrent pattern the value of the climate indices (i.e. EAWR, NAO, ENSO), acquired for the different months mapped towards this pattern. This process enables determining whether a recurrent pattern is associated to either positive or negative value of a particular index significantly, and therefore a connection between the surface winds over the Black Sea and large-scale teleconnection indices. Figure 60 shows for each recurrent pattern of the surface current, the distribution of positive and negative phases of the three teleconnection indices during the months mapped towards this atmospheric pattern. According to the figure, the EAWR index and the ENSO index are negative significantly during months mapped towards pattern 5, which indicates that the occurrence of pattern 5 (Anti-cyclonic RIM Current and Batumi Dipole Eddies) is promoted by these indices. On the other hand, ENSO index is significantly positive during months mapped towards pattern 2 (Cyclonic RIM Current and Anti-cyclonic Batumi Eddy) and therefore influence the surface current structure.

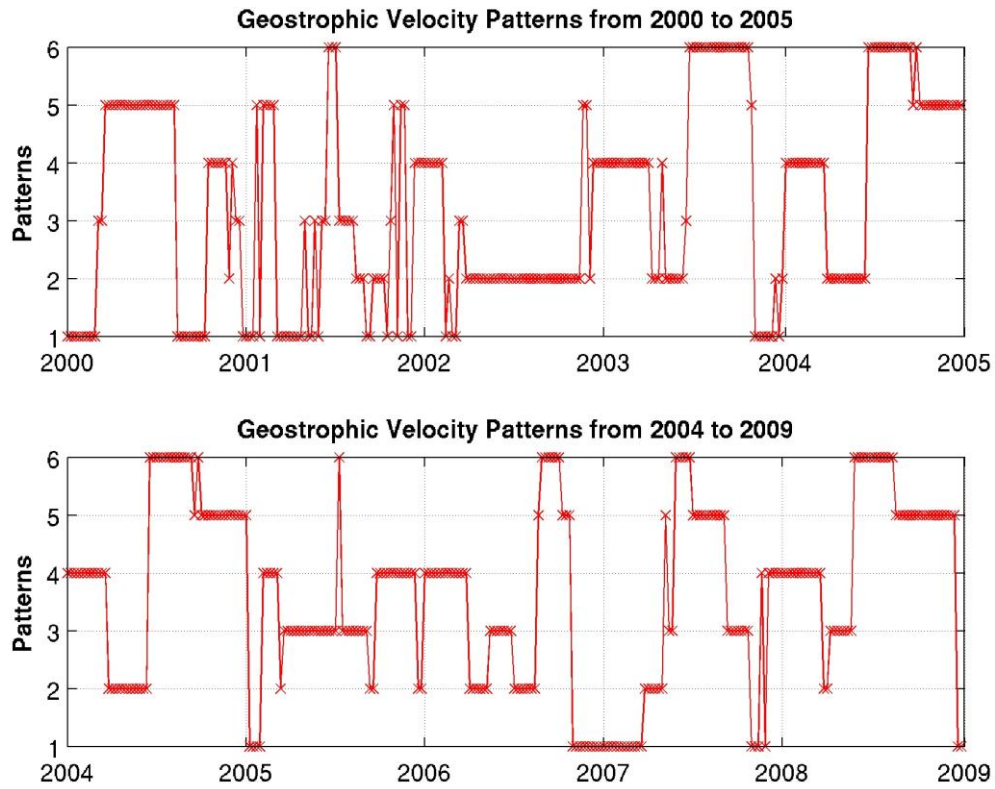


Figure 55. The inter-annual variability of the six patterns of the surface currents

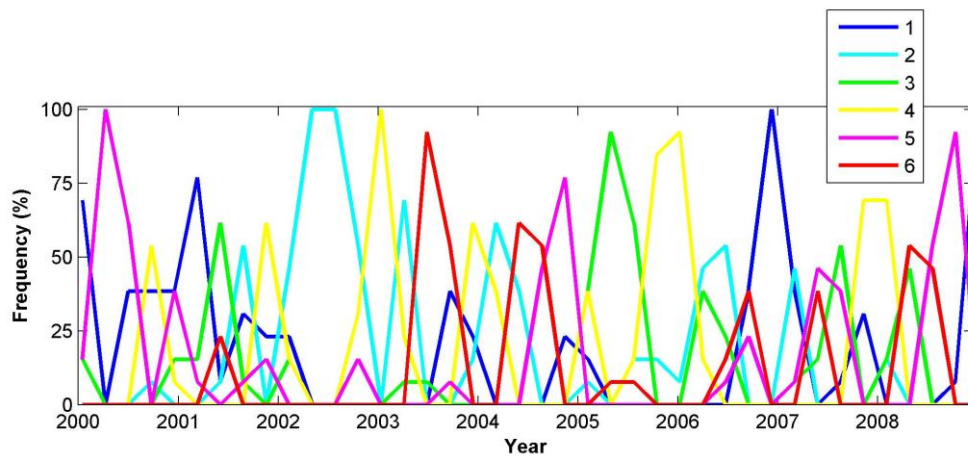


Figure 56. Evolution of the duration and the frequency of the six patterns of the surface currents shown in Figures 47 - 52. For instance, the SOM Pattern 2 lasted for approximately 3 months and dominated the period between 2002 and 2003 when no other patterns occurred.

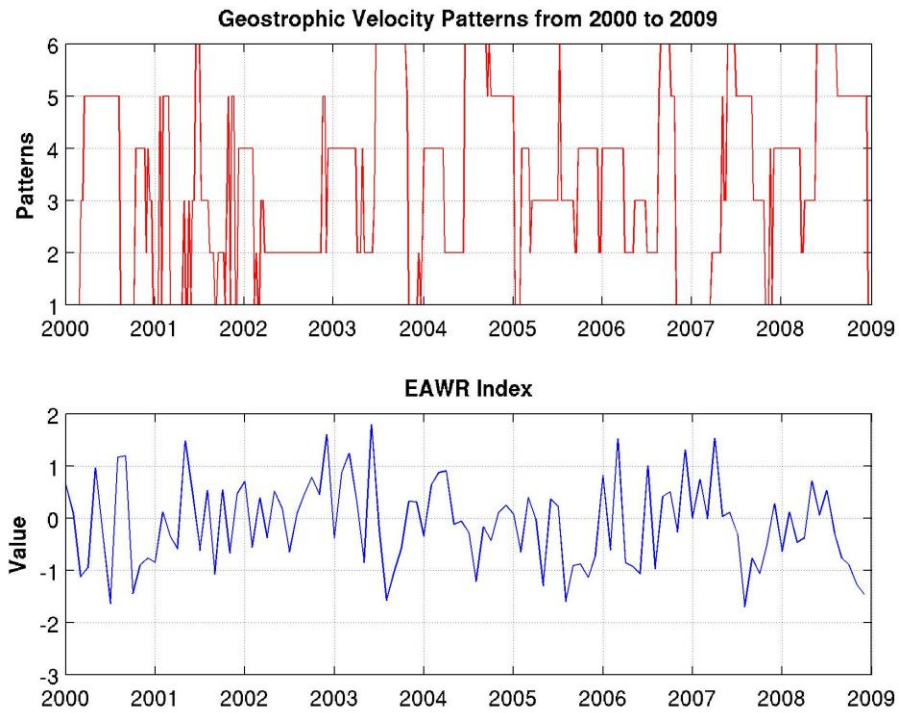


Figure 57. Comparison between the inter-annual variability of the six patterns of the surface currents and the EAWR index

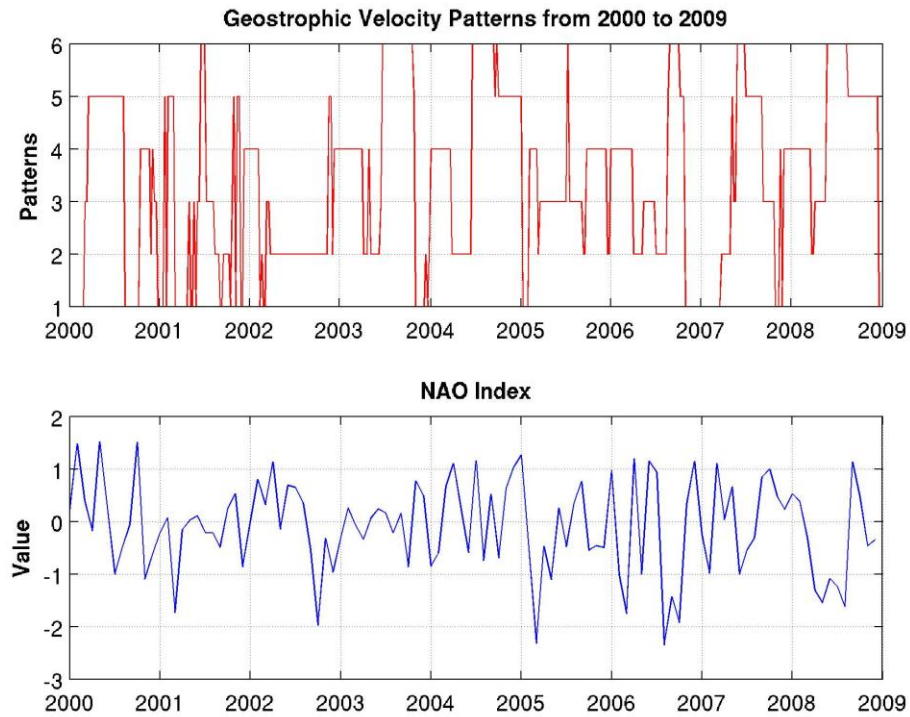


Figure 58. Comparison between the inter-annual variability of the six patterns of the surface currents and the NAO index

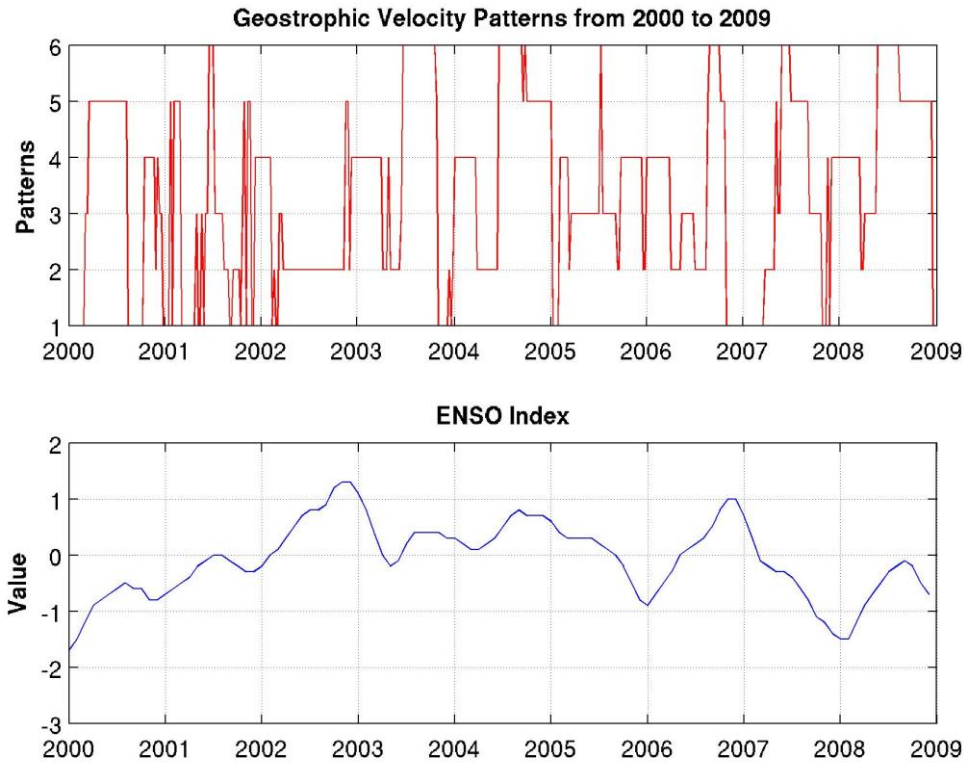


Figure 59. Comparison between the inter-annual variability of the six patterns of the surface currents and the ENSO index

Table 8. The percentages of the six patterns of the surface currents with respect to the large-scale teleconnection indices. For example, when the ENSO index is positive, Pattern 2 has the highest possibility to form among the six patterns at 25%. Yet, when the ENSO index is negative, pattern 6 has the smallest possibility of occurring at only 8%.

GEOSTROPHIC VELOCITY						
	(+) <i>NAO</i>	(-) <i>NAO</i>	(+) <i>EAWR</i>	(-) <i>EAWR</i>	(+) <i>ENSO</i>	(-) <i>ENSO</i>
<i>Pattern 1</i>	20 %	13 %	20 %	14 %	11 %	20 %
<i>Pattern 2</i>	25 %	15 %	25 %	16 %	30 %	11 %
<i>Pattern 3</i>	14 %	16 %	11 %	18 %	14.5 %	14.5 %
<i>Pattern 4</i>	15 %	24 %	22 %	16 %	20 %	23 %
<i>Pattern 5</i>	17 %	17 %	12 %	22 %	7 %	23.5 %
<i>Pattern 6</i>	9 %	15 %	10 %	14 %	17.5 %	8 %

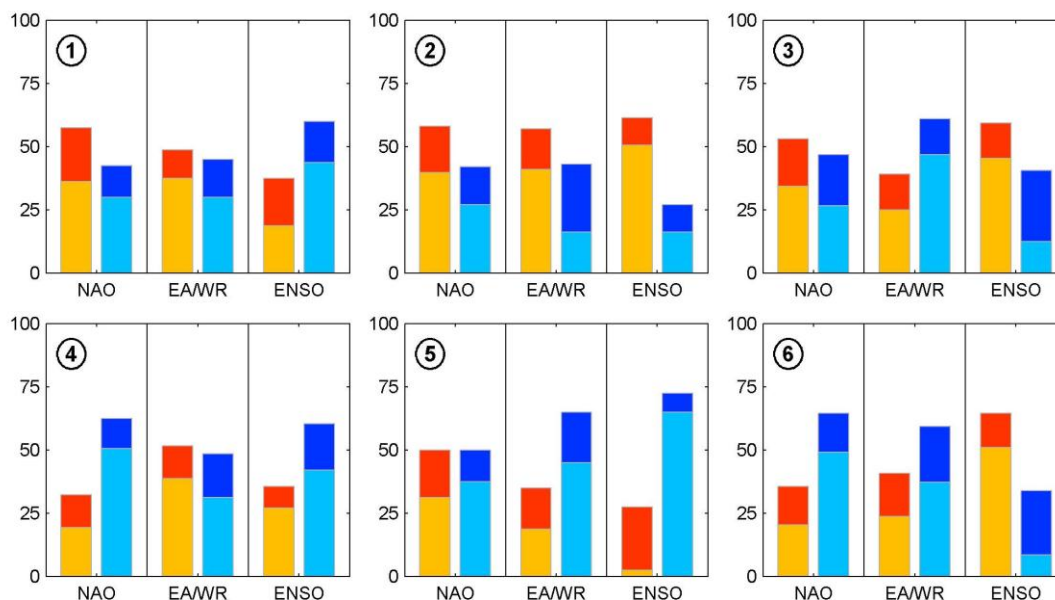


Figure 60. Distribution for each pattern of the surface currents between positive (red) and negative (blue) phases of the teleconnection indices. The areas with darker colors represent the strong phases for which the index's absolute value is greater than a standard deviation. Monthly average values of the climate are obtained through the NOAA Climate Prediction Center (Available at <http://www.cpc.ncep.noaa.gov/data/teledoc/telecontents.shtml>).

VI. SURFACE WINDS

The wind data from 1992 to 2012 were obtained from QuikSCAT. This data is representative of the winds near the surface of the Black Sea. The data provides monthly means that show the seasonal variation of the surface currents. After conducting the SOM, six patterns were found. Additionally, the inter-annual variability of the winds was obtained. Throughout the initial analysis different time frames were selected and examined throughout the initial analyses. A ten-year-long data set was found to be sufficient to extract the patterns of the long-term temporal and spatial variation due to the fact that any data sets covering a period longer than ten years do not affect the results. Therefore, this research focuses on data sets from 1999 to 2009.

A. MONTHLY MEAN WINDS

The monthly average of the winds for January is shown in Figure 61. In the Sea of Azov region, the winds are weak and easterly with a slight cyclonic curve. Strong northerly winds are observed in the western shelf and they get weaker as they move towards the central Black Sea. At the central eastern shelf, a weak cyclonic motion of the winds is detected. These winds are very weak compared to the winds of the western shelf. Meanwhile, the wind in the Batumi eddy region shows a strong southerly pattern within a small region. At the southeastern corner of the basin, weak easterly winds are observed.

In Figure 62, the climatological average of the winds for February is presented. This average is similar to January with some exceptions. Additionally, the winds in February are stronger. During this time, the Sea of Azov exhibits a chaotic pattern comprised of very weak winds, the cyclonic motion at the eastern shelf is more pronounced, the southerly winds in the Batumi eddy region become a part of the cyclonic motion, and the weak easterly winds at the southeastern corner of the basin disappear.

In March, the winds in the Sea of Azov region become stronger as they begin to blow from the southeast. The winds north of the western basin take on a chaotic nature as their movement appears to have no apparent pattern. The winds at the western and eastern shelves are weaker. The central Black Sea region exhibits relatively strong winds.

The cyclonic motion of the winds at the eastern shelf remains and the strong winds in the Batumi eddy region appear again (see Figure 63).

Figure 64 shows the climatological average of the winds for April. A clear pattern can be observed as the strong northerly winds start off of the Crimean peninsula and blow through the central basin reaching to the Bosphorus. No clear pattern is observed at the eastern shelf except for the mediocre southerly winds at the southeast corner. Weak easterly winds are observed at the Sea of Azov.

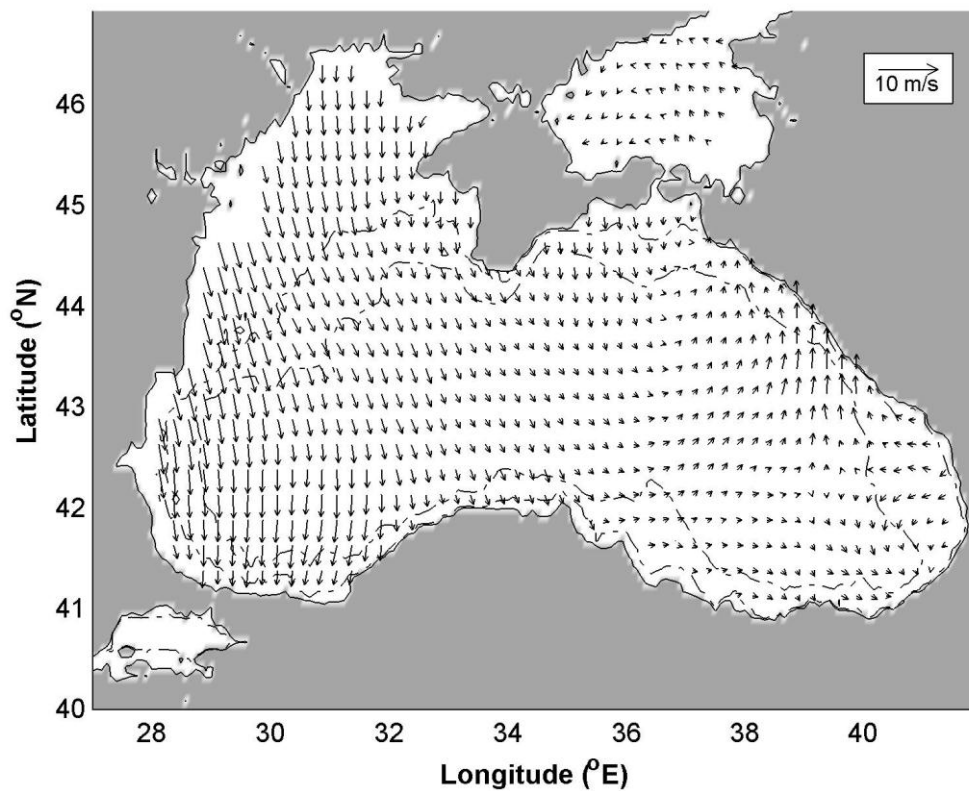


Figure 61. The climatological average of the winds for January

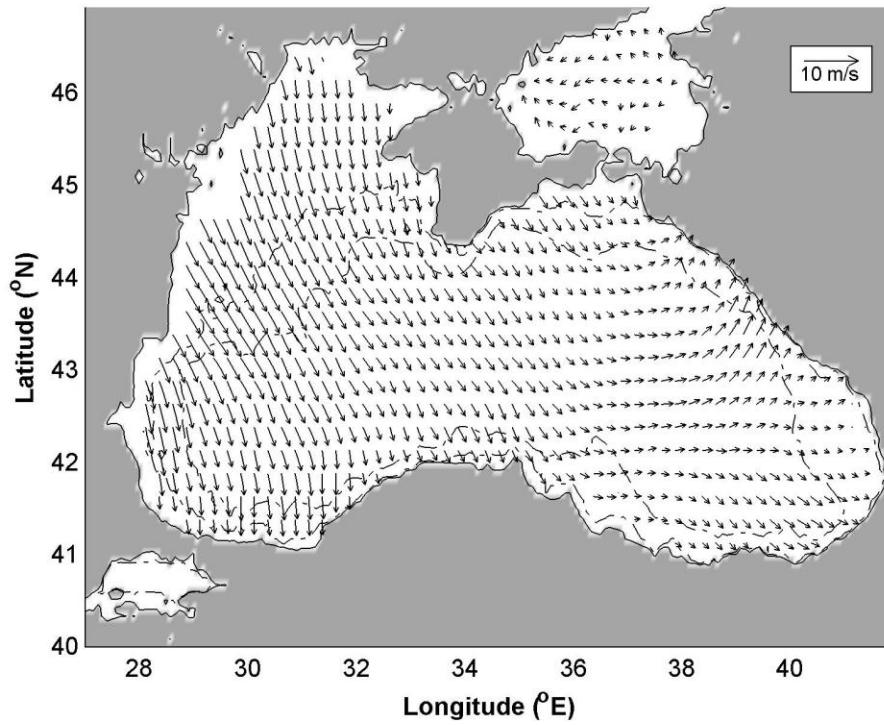


Figure 62. The climatological average of the winds for February

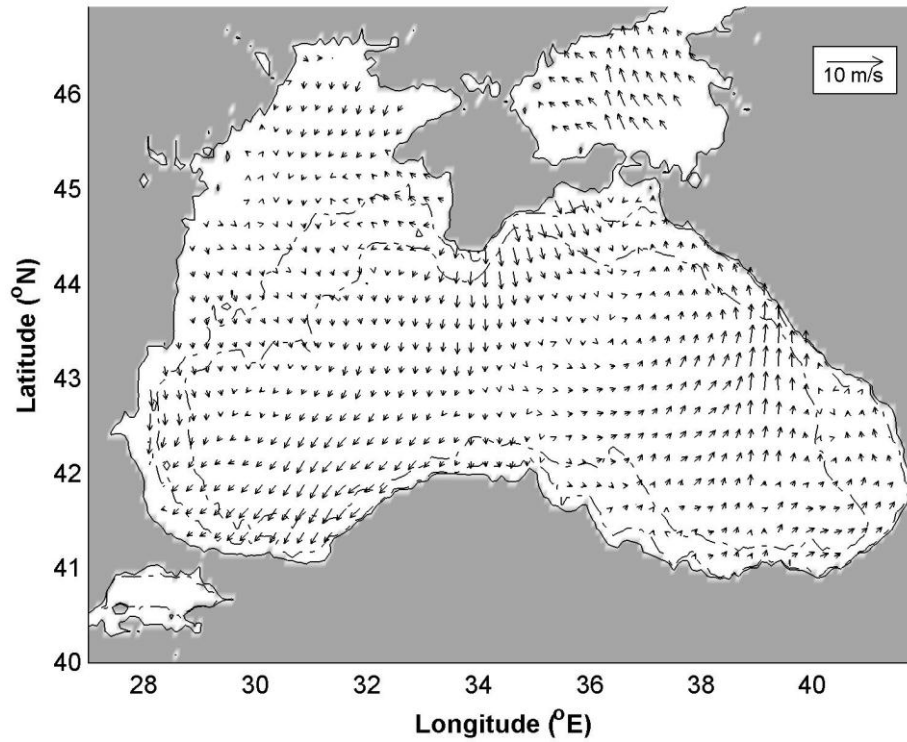


Figure 63. The climatological average of the winds for March

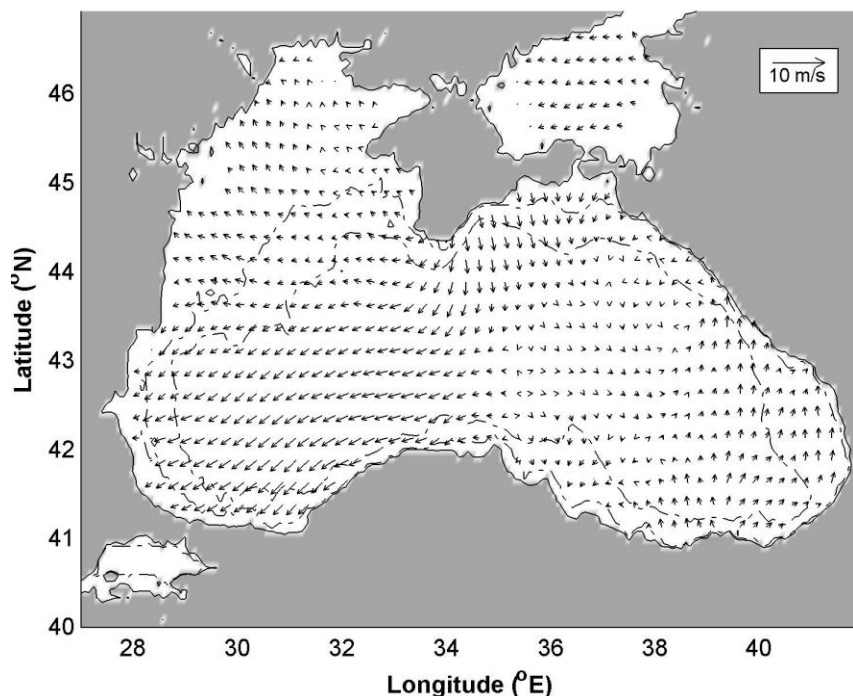


Figure 64. The climatological average of the winds for April

In May the strong northerly winds are evident at the north of the eastern shelf and at the south of the western shelf. They curve slightly anti-cyclonically at the southwest of the western shelf. Whereas, the winds at southeast of the eastern shelf exhibit a cyclonic curve. A very weak anti-cyclonic circulation can be noted at the northwestern corner of the basin. Additionally, weak northerly winds are detected at the Sea of Azov (see Figure 65).

Figure 66 showcases the climatological average of the winds for June. The winds mostly have a basin-wide northwesterly pattern and are very strong. A slight anti-cyclonic curve at the southwestern corner of the western shelf is evident. At the far southeast, a tendency of westerly winds is noted.

Figure 67, Figure 68, Figure 69, and Figure 70 illustrate the climatological averages of the winds for July, August, September, and October, respectively. The nature of the wind patterns is very similar for the climatological averages of these months with minor exceptions. The winds, in general, become northerlies and get stronger basin-wide in July. During these months, the anti-cyclonic curve in the western shelf and the

cyclonic curve in the eastern shelf are well-pronounced. In August the winds get even stronger and they differentiate from the winds in July in that the winds at the Sea of Azov start to blow from the northeast. The wind pattern of August is the same in September except that the winds weaken at the Sea of Azov. In October the winds generally turn slightly to the west from their northerly flow pattern.

In Figure 71 the climatological average of the winds for November is presented. The winds start to flow from the northeast instead of from the north and they get weaker at the Sea of Azov. The northerly winds dominate the southern part of the western shelf, the northern part of the eastern shelf, and the central Black Sea. Meanwhile, a weak cyclonic motion at the far southeast is detected.

In December only the winds in the southern part of the eastern shelf remain weak, while the winds in the rest of the basin get stronger. The northerly pattern of the winds continues to dominate. Additionally, northeasterly winds are noted at the Sea of Azov and the motion of the winds at the southeastern corner of the basin appears to be chaotic rather than cyclonic (see Figure 72).

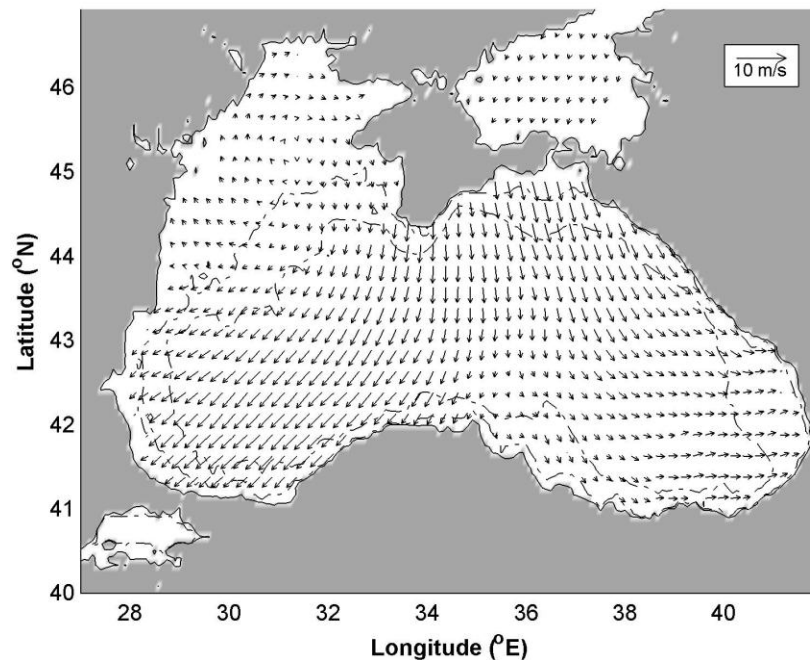


Figure 65. The climatological average of the winds for May

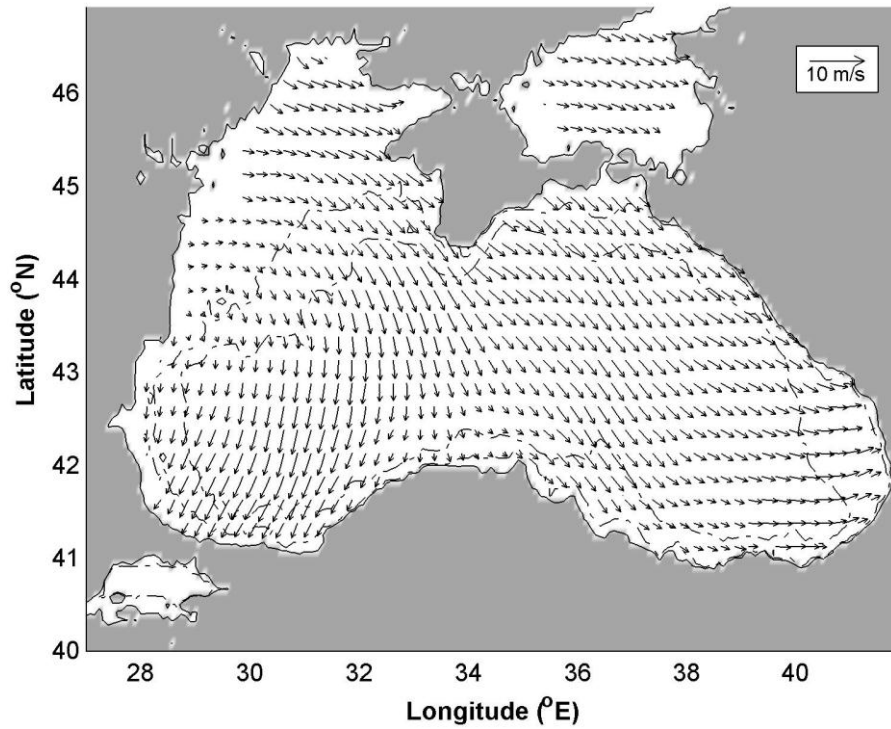


Figure 66. The climatological average of the winds for June

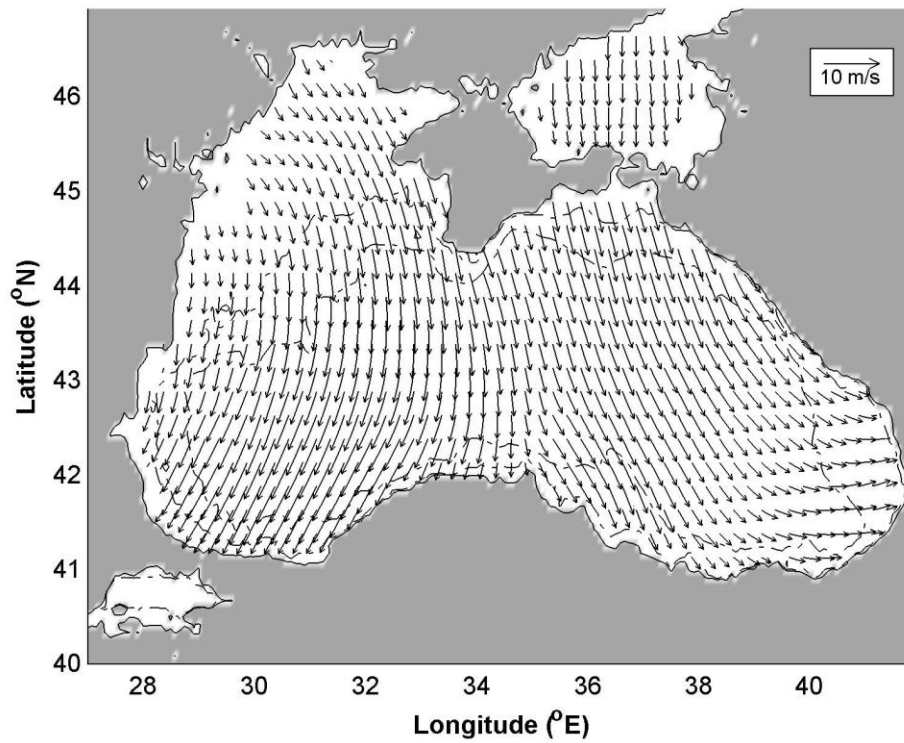


Figure 67. The climatological average of the winds for July

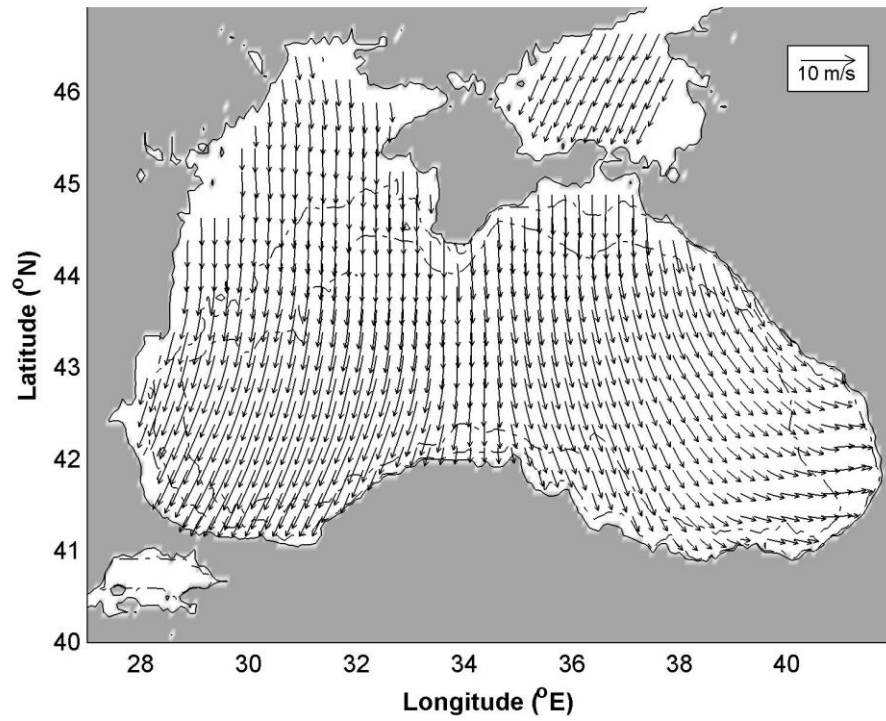


Figure 68. The climatological average of the winds for August

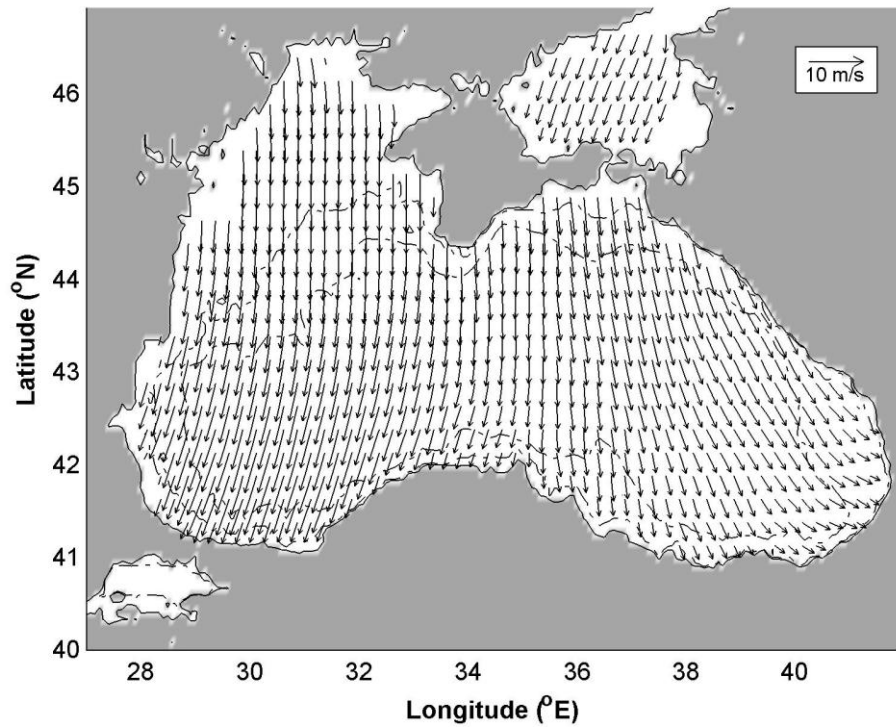


Figure 69. The climatological average of the winds for September

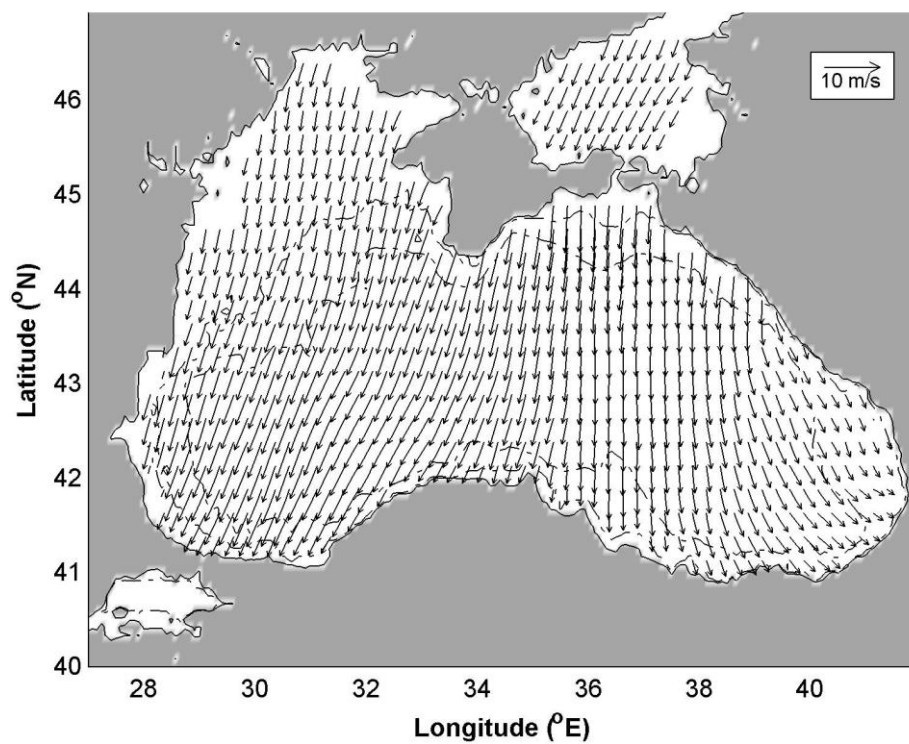


Figure 70. The climatological average of the winds for October

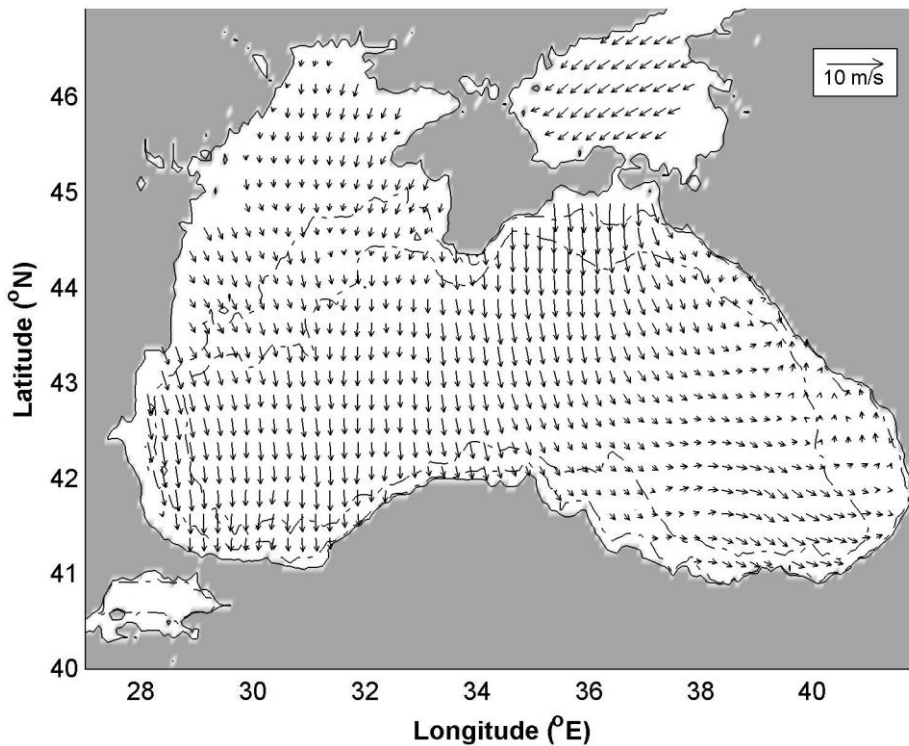


Figure 71. The climatological average of the winds for November

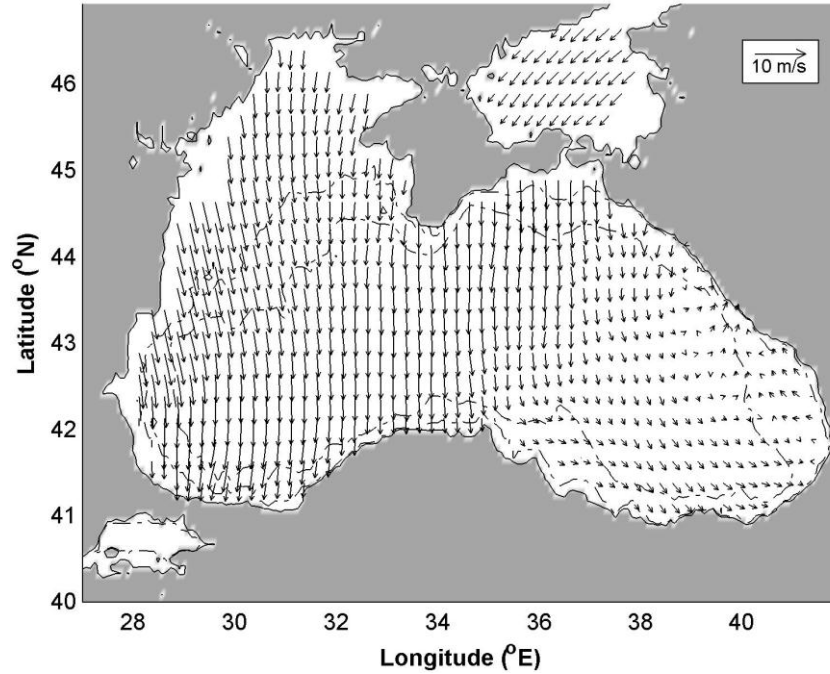


Figure 72. The climatological average of the winds for December

B. TEMPORAL AND SPATIAL VARIABILITY

To study the temporal and spatial variation of the winds, the Black Sea basin is subject to iterative SOM analysis. The DBI demonstrates the best option in terms of representing the total number of clusters in the data set. The smaller the DBI, the better and more practical the data representation is. Therefore, in light of the DBI, the SOM analysis for the surface currents is based on six clusters (see Figure 73).

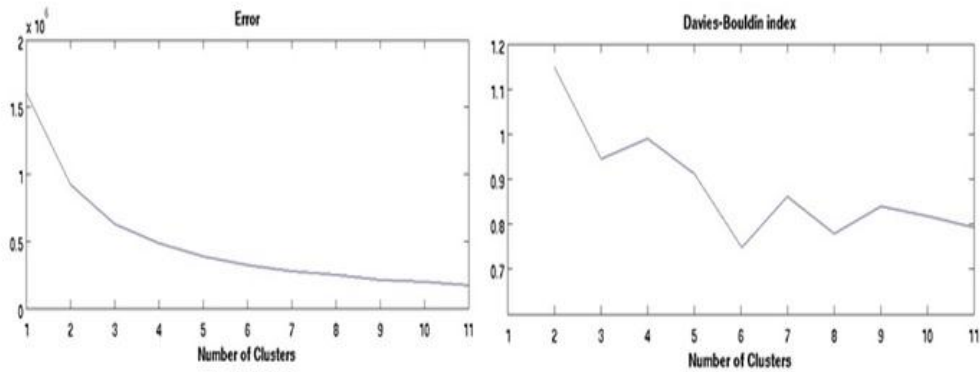


Figure 73. The Davies-Bouldin index results concerning the wind data set

1. SIX PATTERNS

a. Pattern 1: The Northerly Winds and the Cyclonic Curve in the Western Shelf

The first pattern represents more than 13% of the whole data set. In this pattern, westerly winds are observed north of the western shelf. The winds curve anti-cyclonically and become northeasterly south of the western shelf. At the eastern shelf, on the other hand, the winds blow from the northwest with a slight cyclonic curve south of the eastern shelf (see Figure 74).

b. Pattern 2: The Easterly Winds and the Anti-cyclonic Curve in the Western Shelf

More than 13% of the total representation for the data set is covered by the second pattern. The main feature of this pattern is the anti-cyclonic curve of the winds in the western shelf. The winds blow from the east, starting at the eastern shelf, and from the central Black Sea region. The winds are stronger to the west and they are strongest north of the western shelf (see Figure 75).

c. Pattern 3: The Dominance of the Strong Northerly Winds

The third pattern represents 23% of the whole data set. The strong northerly winds almost completely dominate the Black Sea region. The winds lose their strength to the south of the eastern shelf and they exhibit a cyclonic curve in this region (see Figure 76).

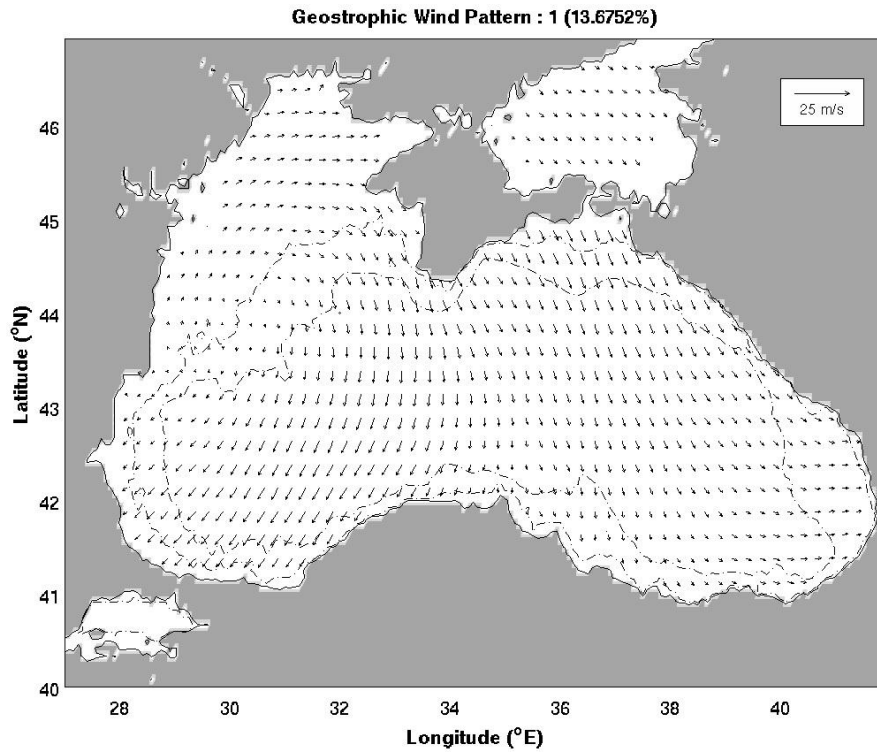


Figure 74. The first pattern of the winds and its percentage

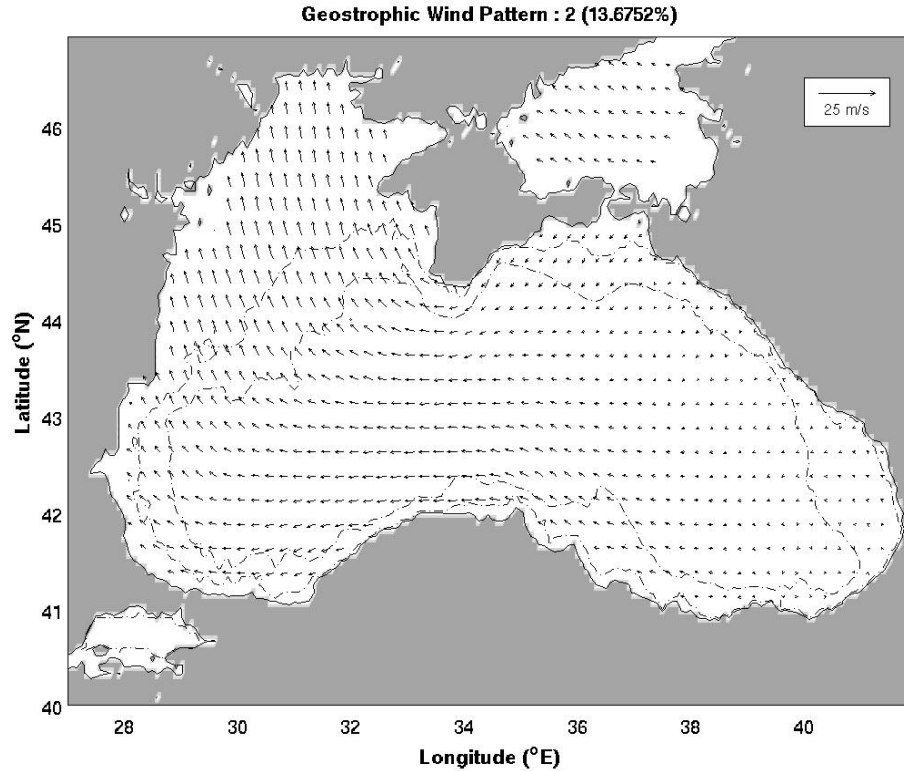


Figure 75. The second pattern of the winds and its percentage

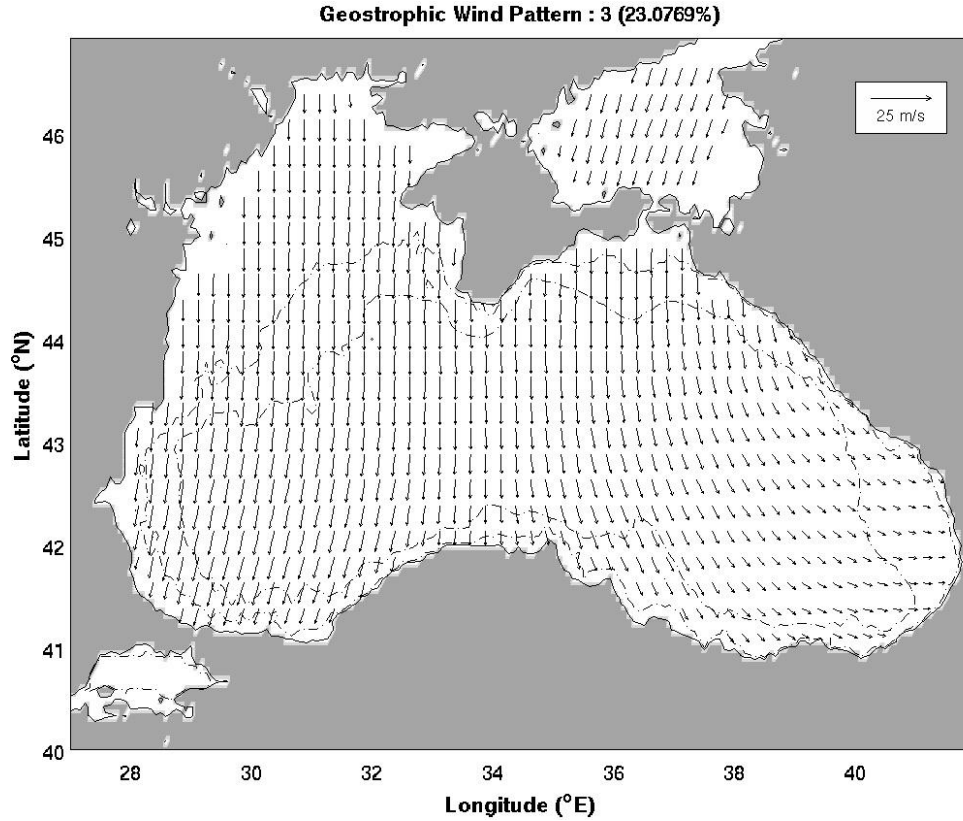


Figure 76. The third pattern of the winds and its percentage

d. Pattern 4: The Northwestern Winds in the West and the Westerly Winds in the East

The fourth pattern comprises more than 16% of the whole representation of the data set. The western and eastern shelves exhibit two different wind characteristics. The strong northwesterly winds occur in the western shelf with a little anti-cyclonic curve to the south, whereas, starting from the central Black Sea, the winds blow from the west and the whole eastern shelf is dominated by the relatively weak easterly winds (see Figure 77).

e. Pattern 5: The Dominance of the Strong Northeasterly Winds

The fifth pattern represents more than 21% of the whole data set. The northeasterly winds dominate the whole Black Sea region with the exception of the southeastern corner of the basin. The winds become weaker to the southeast and almost disappear completely close to the coast (see Figure 78).

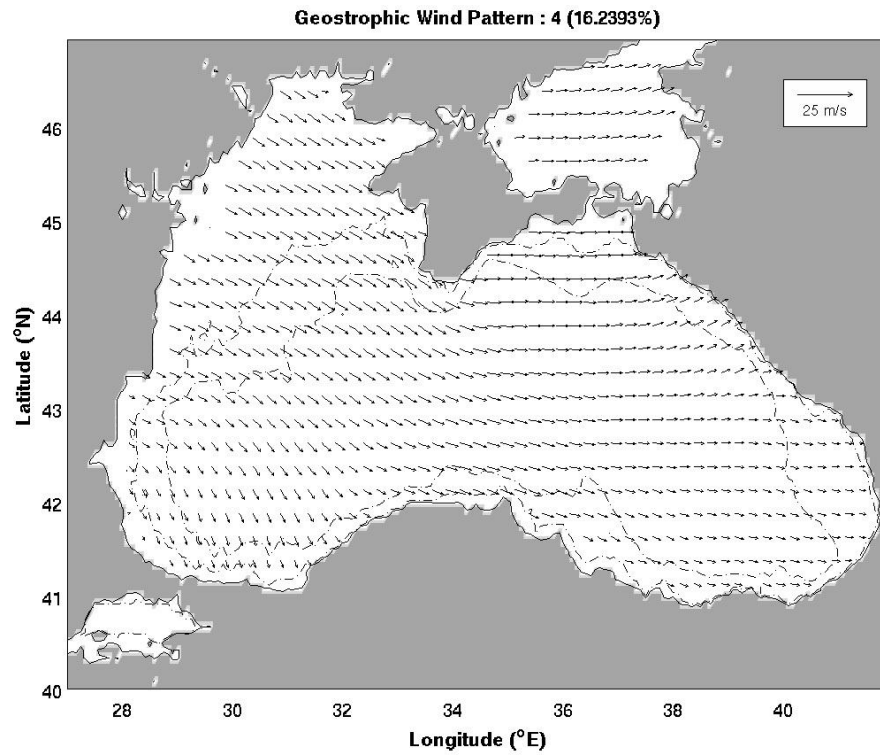


Figure 77. The fourth pattern of the winds and its percentage

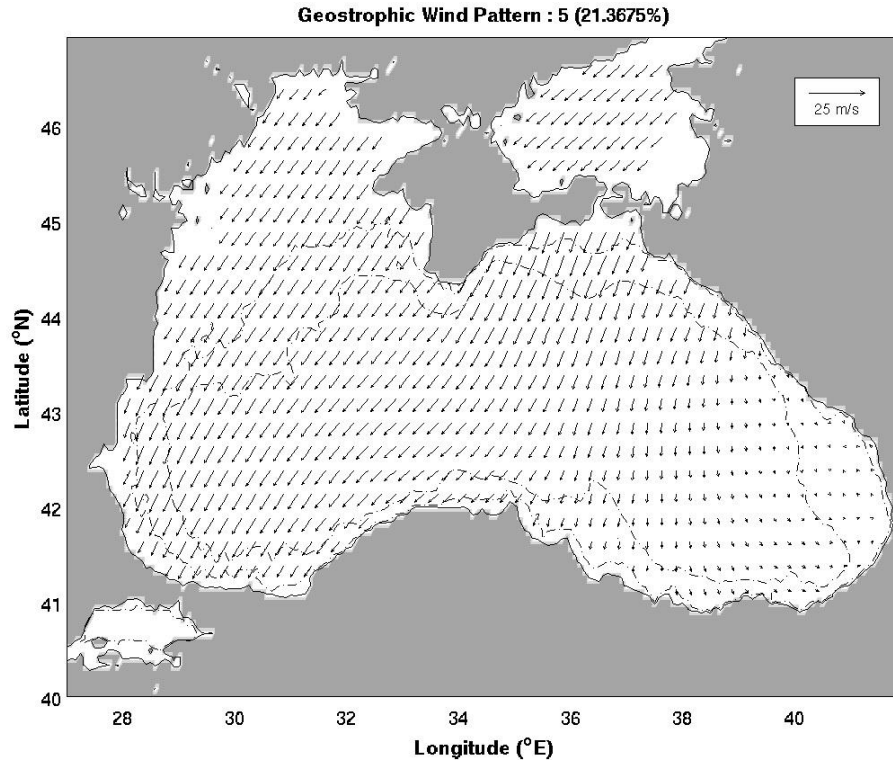


Figure 78. The fifth pattern of the winds and its percentage

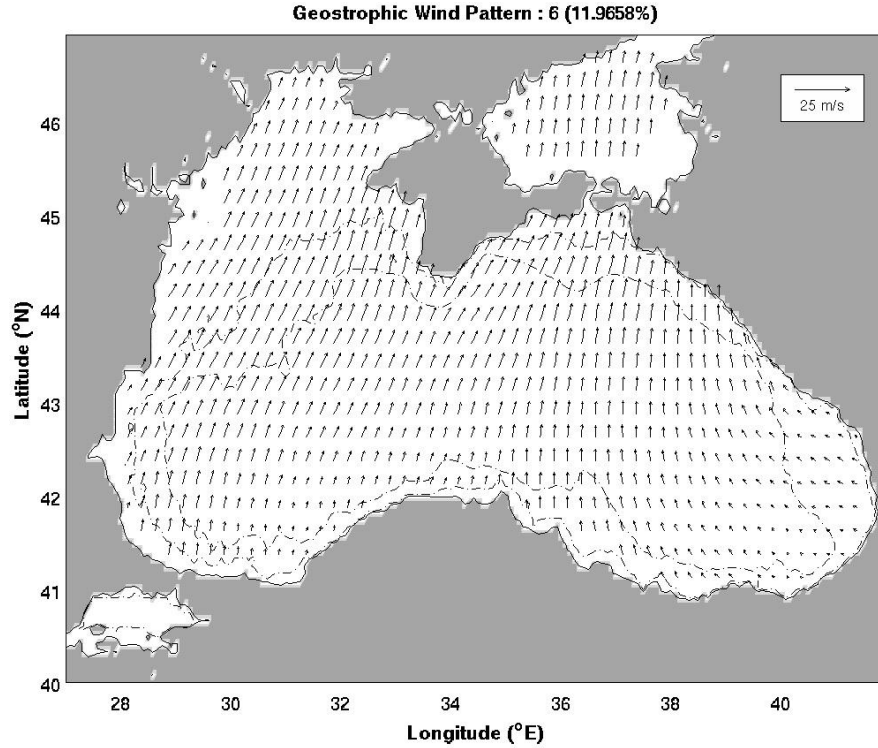


Figure 79. The sixth pattern of the winds and its percentage

f. Pattern 6: The Strong Southwesterly Winds

Almost 12% of the total representation for the data set is covered by the sixth pattern. The southwesterly winds dominate the whole Black Sea region with the exception of the southeastern corner of the basin. The winds blowing from the southeast become weaker and they have a slight anti-cyclonic curve (see Figure 79).

2. TEMPORAL VARIATION

To better illustrate the monthly and seasonal variability of the winds, the rate of occurrence of the six patterns was computed and the results are shown in Figure 80. Pattern 1 clearly dominates during the summer when the weather warms up. Its maximum contribution is in June when it takes up almost 35% of the data set and it disappears completely in January and February. Pattern 2 is more likely to be observed during spring-like and fall-like months. Its maximum contribution is detected in May, taking up a little more than 20% of the data set, and it has the second highest percentage among the

six patterns in this particular month. This pattern declines in extreme weather conditions like the cold weather in winter and the warm weather in the summer. Pattern 3 tends to appear mostly during the second six-month period of the year. It reaches its maximum in August and becomes the pattern most likely to appear during that time of the year. From July to mid-September Pattern 3 is the most dominant pattern among the six patterns. It tends to stay at 15%-18% during the first six-month period of the year and never disappears completely. Pattern 4 comprises the highest portion of the data set during the winter-like and summer-like months. It is the most dominant pattern in February with almost 35% and it is the second most dominant pattern in June with ~28%. Pattern 4 gets very weak during the spring and shows an oscillatory pattern of contribution during the fall. Pattern 5 contributes significantly during the spring and fall. It reaches its maximum percentages in fall-like months and dominates in October with almost 40% and in April with ~25%. On the other hand, the minimum contribution of Pattern 5, with less than 10%, is observed during June. Pattern 6 has no significant seasonality and occurs occasionally throughout the year. It contributes the least among the six patterns from May to September when it makes up only about 5% of the data set. With a little less than 30% contribution, Pattern 6 is the pattern most likely to be detected in March.

The time series (2000 to 2009) of the six wind patterns (shown in Figures 74-79) derived by SOM is shown in Figure 81, and the evolution of the duration and the frequency of the same patterns is shown in Figure 82 in order to illustrate the inter-annual variability. Furthermore, Figure 83, Figure 84 and Figure 85 demonstrate the contemporaneous EAWR, NAO, and ENSO indices, respectively, along with the times series of the winds. In addition to these figures, Tables 10 and 11 provide a deeper understanding of the relationship between the wind patterns and the large-scale phenomena, as well as the relationship between the wind patterns and the surface current patterns. Figure 86 presents the anomalies of the wind components for each month (from 2000 to 2009) and indicates to which recurrent patterns of the surface winds (shown in Figures 74-79) these anomalies are mapped by the SOM procedure.

The potential influence of large-scale teleconnection indices on the recurrent patterns of the surface winds (shown in Figures 74-79) are evaluated by estimating for

each recurrent pattern the value of the climate indices (i.e. EAWR, NAO, ENSO), acquired for the different months mapped towards this pattern. This process enables determining whether a recurrent pattern is associated to either positive or negative value of a particular index significantly, and therefore a connection between the surface winds over the Black Sea and large-scale teleconnection indices. Figure 87 shows for each recurrent pattern of the surface wind, the distribution of positive and negative phases of the three teleconnection indices during the months mapped towards this atmospheric pattern. According to the figure, the EAWR index and the ENSO index are negative significantly during months mapped towards pattern 2, which indicates that the occurrence of pattern 2 (The Easterly Winds and the Anti-cyclonic Curve in the Western Shelf) is promoted by these indices. On the other hand, NAO and EAWR indices are significantly positive during months mapped towards pattern 4 (The Northwestern Winds in the West and the Westerly Winds in the East) and therefore influence the wind anomaly.

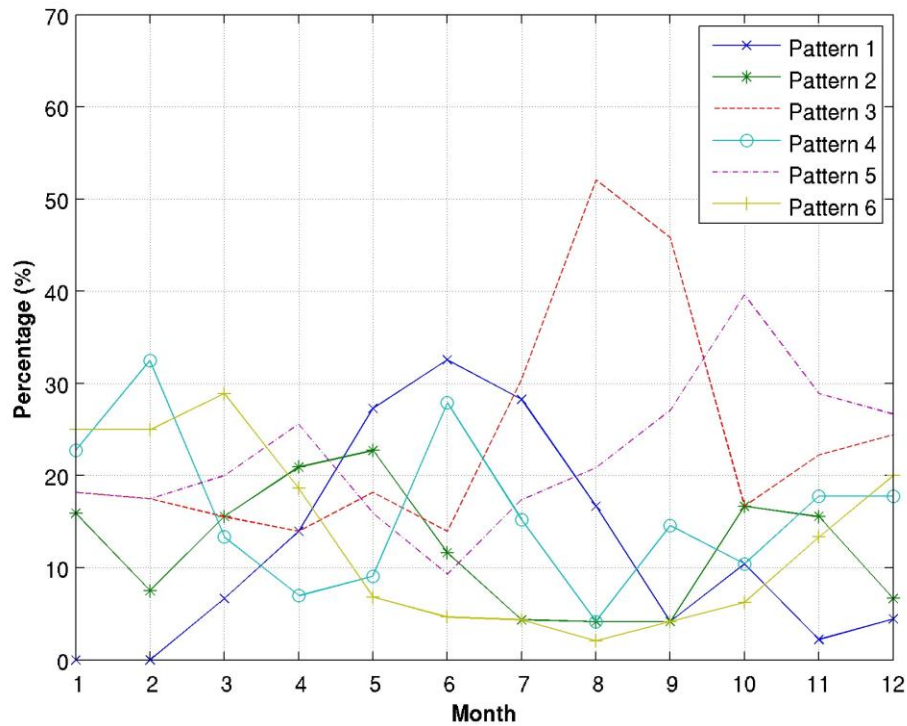


Figure 80. Monthly percentage of the six wind patterns

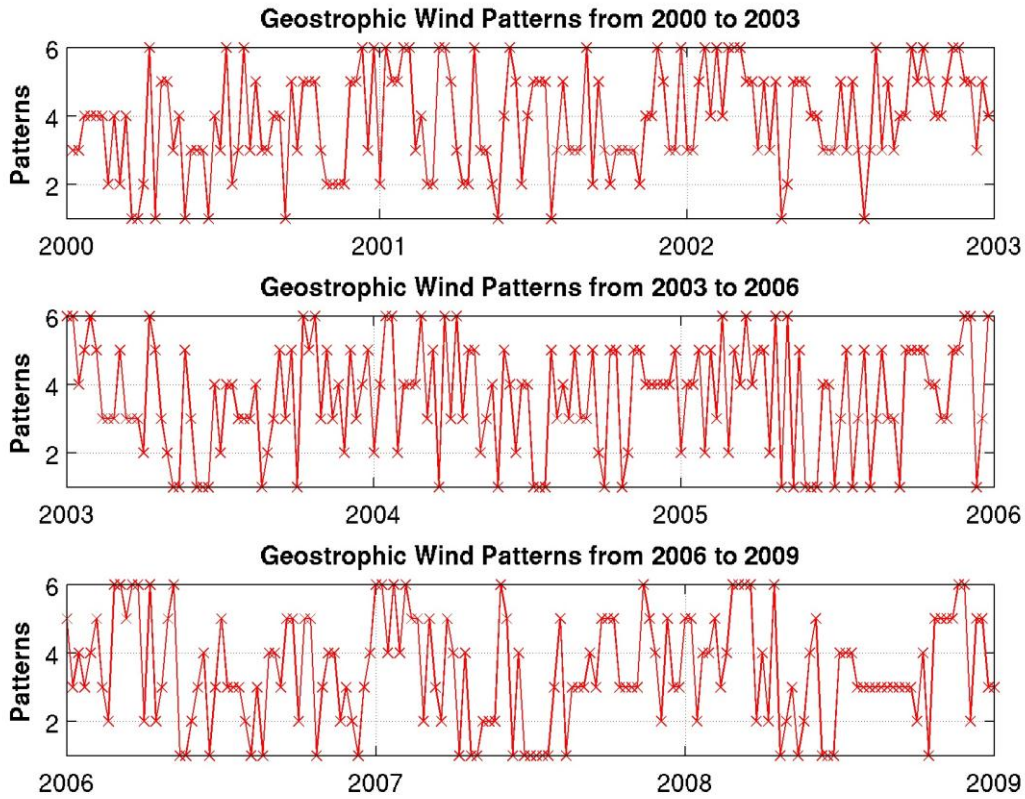


Figure 81. The inter-annual variability of the six wind patterns

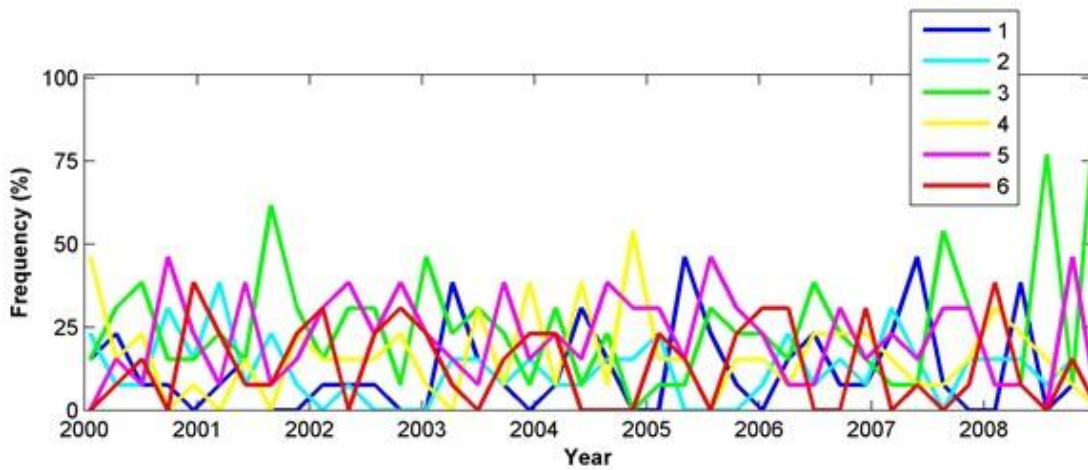


Figure 82. Evolution of the duration and the frequency of the six patterns of the winds shown in Figures 74-79. For instance, the SOM Pattern 3 lasted more than 6 months and dominated approximately 2 months between years 2008 and 2009 with more than 50%.

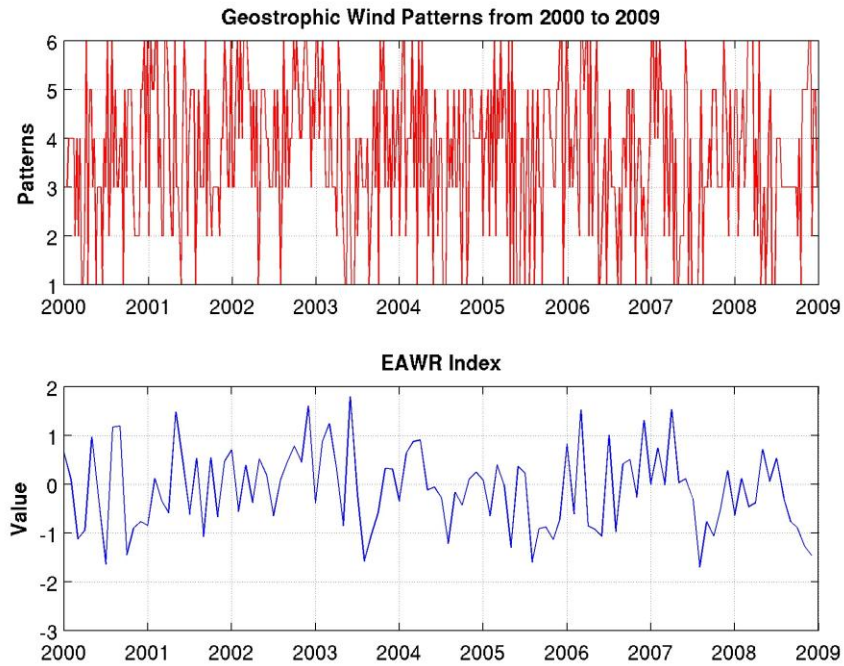


Figure 83. Comparison between the inter-annual variability of the six wind patterns and the EAWR index

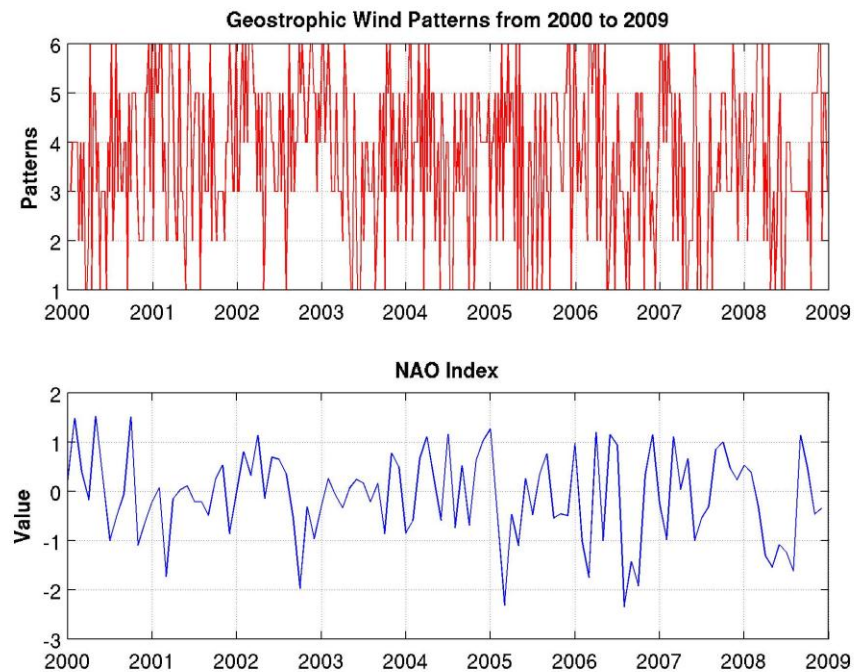


Figure 84. Comparison between the inter-annual variability of the six wind patterns and the NAO index

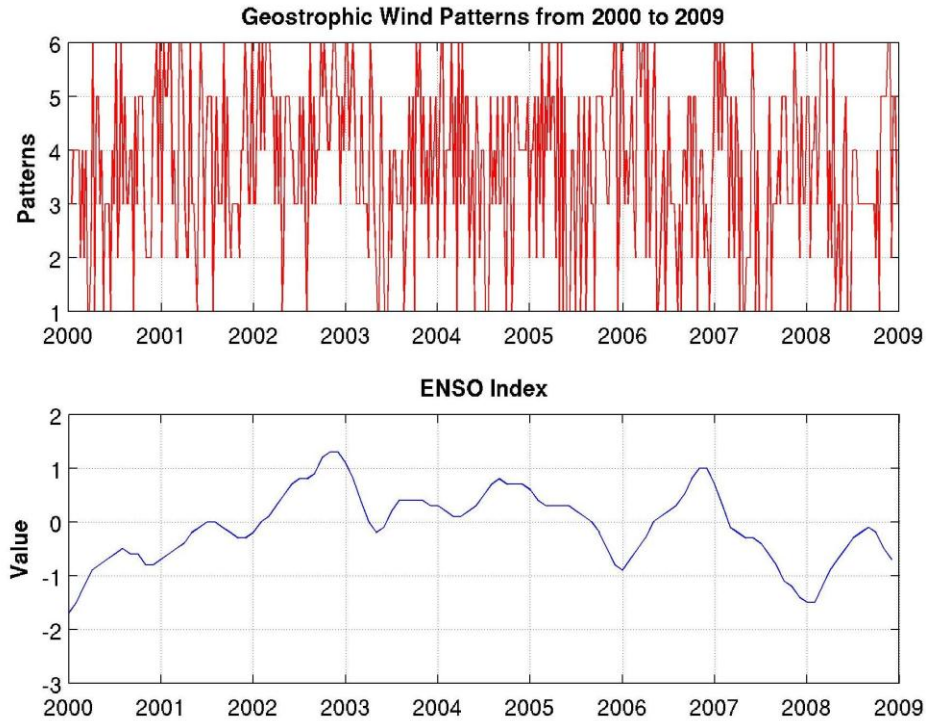


Figure 85. Comparison between the inter-annual variability of the six wind patterns and the ENSO index

Table 9. The percentages of the six wind patterns with respect to the large-scale phenomena. For example, when the NAO index is positive, Pattern 3 has the highest possibility to form among the six patterns at 32%. On the other hand, when the EAWR index is positive, Pattern 2 has the smallest possibility of occurring at 7%.

GEOS. WIND						
	(+) <i>NAO</i>	(-) <i>NAO</i>	(+) <i>EAWR</i>	(-) <i>EAWR</i>	(+) <i>ENSO</i>	(-) <i>ENSO</i>
<i>Pattern 1</i>	11 %	12 %	10 %	13 %	11.5 %	12.5 %
<i>Pattern 2</i>	11 %	12 %	7 %	15 %	10 %	14 %
<i>Pattern 3</i>	32 %	18 %	26 %	23 %	23 %	26 %
<i>Pattern 4</i>	21 %	13 %	24 %	11 %	19 %	14 %
<i>Pattern 5</i>	19 %	25 %	21 %	24 %	25 %	21 %
<i>Pattern 6</i>	6 %	19 %	12 %	14 %	11.5 %	12.5 %

Table 10. The percentages of the six wind patterns with respect to the six patterns of the surface currents. For example, when Pattern 3 of the winds occurs, Pattern 2 of the surface currents has the highest possibility to form at 5.54%. On the other hand, when Pattern 1 of the winds occurs, Pattern 4 has the smallest possibility of occurring at 0.43%.

		GEOS. WIND						
		1	2	3	4	5	6	TOTAL
GEOS. VELOCITY	1	0.43 %	3.2 %	3.62 %	3.62 %	2.99 %	3.2 %	17.06 %
	2	2.56 %	1.92 %	5.54 %	2.56 %	4.9 %	2.35 %	19.83 %
	3	3.62 %	1.49 %	3.2 %	1.28 %	2.99 %	1.07 %	13.65 %
	4	0.43 %	2.35 %	4.69 %	3.2 %	4.69 %	4.48 %	19.83 %
	5	2.77 %	1.92 %	4.26 %	2.56 %	4.05 %	1.49 %	17.06 %
	6	2.35 %	0.85 %	2.99 %	3.2 %	2.56 %	0.64 %	12.57 %
	TOTAL	12.15 %	11.73 %	24.31 %	16.42 %	22.17 %	13.22 %	100 %

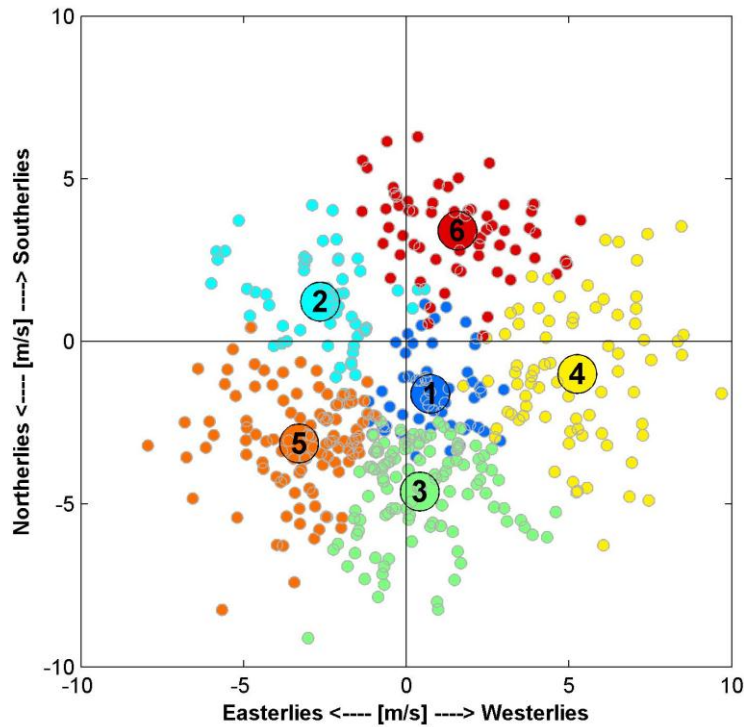


Figure 86. Monthly anomalies of the components of zonal and meridional winds. The six wind patterns provided by the SOM analysis are distinguished by the large circles. The smaller circles, on the other hand, depict the basin scale averages for all the months from January 2000 to January 2009.

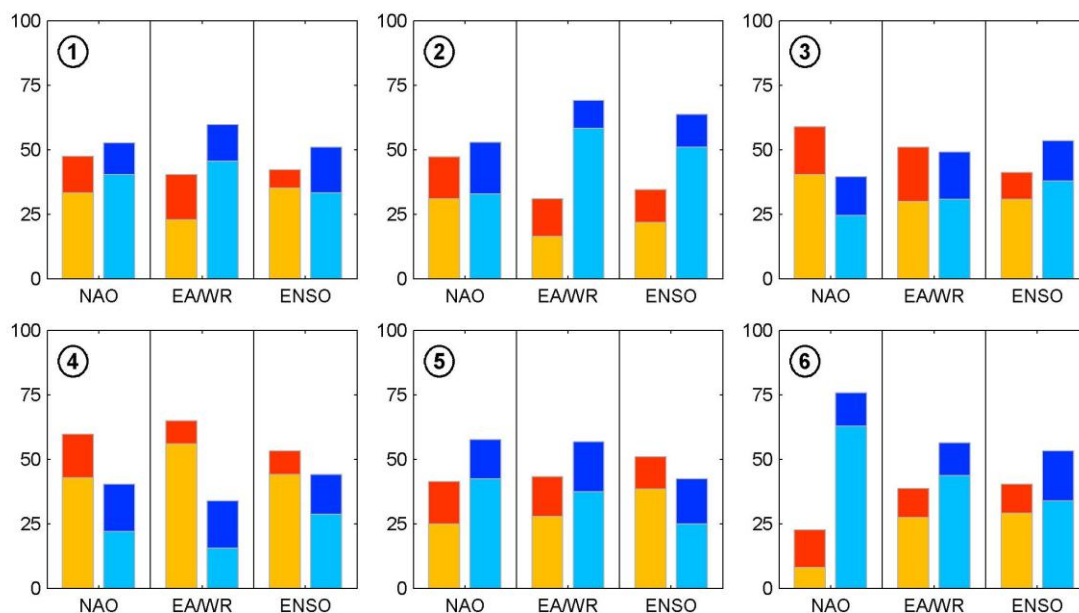


Figure 87. Distribution for each pattern of the surface currents between positive (red) and negative (blue) phases of the teleconnection indices. The areas with darker colors represent the strong phases for which the index's absolute value is greater than a standard deviation. Monthly average values of the climate are obtained through the NOAA Climate Prediction Center (Available at <http://www.cpc.ncep.noaa.gov/data/teledoc/telecontents.shtml>).

THIS PAGE INTENTIONALLY LEFT BLANK

VII. CHLOROPHYLL

Monthly mean climatological chlorophyll-a concentration is plotted logarithmically and these results are displayed in Figures 88 to 99. Additionally, Figure 100 presents the climatological average of the chlorophyll-a concentration from 1999 to 2009. In January, the concentration in most of the open basin stays around 1 mg/m^3 . Higher values up to 6 mg/m^3 are observed in the coastal region of the northwestern shelf where the Danube, Prut, and Dniester rivers flow to the sea. Likewise, a concentration level up to $5\text{-}6 \text{ mg/m}^3$ is evident in the north region of the Turkish coast where the Kizilirmak and Yesilirmak rivers flow. At the Crimean Peninsula coasts, the concentration slightly decreases and values stay between 0.5 and 1 mg/m^3 (see Figure 88). The eastern shelf of the basin maintains a steady concentration level in February, but the values at the Western shelf generally drop slightly except in the coastal region at the northwest where the river outflows take place. In this particular region, higher values up to 5 mg/m^3 are detected and the area of this higher concentration spreads out compared to January. Meanwhile, high concentration levels at the Turkish coast almost completely disappear (see Figure 89). Figure 90 shows the climatological average of the chlorophyll-a concentration for March. The chlorophyll-a concentration detected is approximately 0.5 mg/m^3 basin-wide. Small regions in the open basin reach a concentration level up to 1 mg/m^3 . The northwest region, which is influenced by the river outflows, exhibits high concentrations up to 4 mg/m^3 off the coast and up to 10 mg/m^3 right along the coast. In April, in the region south of the western shelf and in the central eastern shelf region, concentration levels of 1 mg/m^3 are detected. The river outflows affect a larger area of the northwestern corner of the basin, but the highest values decrease slightly (they are detected at 6 mg/m^3) (see Figure 91). In May, the concentration levels decrease dramatically and remain at approximately 0.2 mg/m^3 at the eastern shelf and at the central western shelf. The river outflow region at the northwestern corner of the basin elongates to the south and reaches up to the Bulgarian coast (see Figure 92). Figure 93 shows the climatological average of the chlorophyll-a concentration during June. It is very similar to May with the exception of the large area at the northwestern corner that is influenced

by the river outflows. During June, higher concentration levels (up to 14 mg/m^3) are detected in that region. The chlorophyll-a concentration levels are almost identical in July, August and September. The concentration level at the northwestern corner begins to shrink, yet the maximum chlorophyll-a level in this particular region is still very high as it remains around 10 mg/m^3 (see Figure 94, Figure 95, and Figure 96, respectively). Figure 97 presents the climatological average of the chlorophyll-a concentration for October. The uniform structure of the basin dissolves and a chaotic distribution in terms of the concentration levels takes place. Both in November and December, the chaotic distribution of the chlorophyll-a concentration increases in intensity and scale. The river outflow region at the northwestern corner elongates and reaches up to the Bosphorus. The central coast of Turkey exhibits higher than average values as well, especially where the rivers flow to the Black Sea (see Figure 98 and Figure 99, respectively). Finally the climatological average of the chlorophyll-a concentration from 1999 to 2009 is shown in Figure 100.

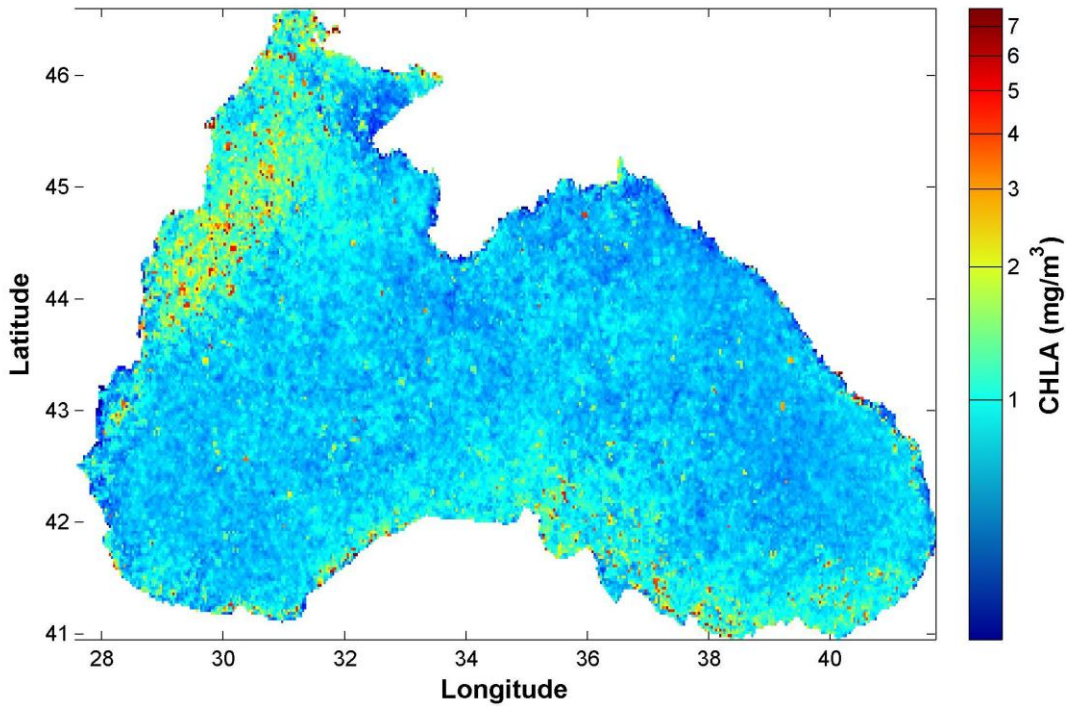


Figure 88. The climatological average of the chlorophyll-a concentration for January

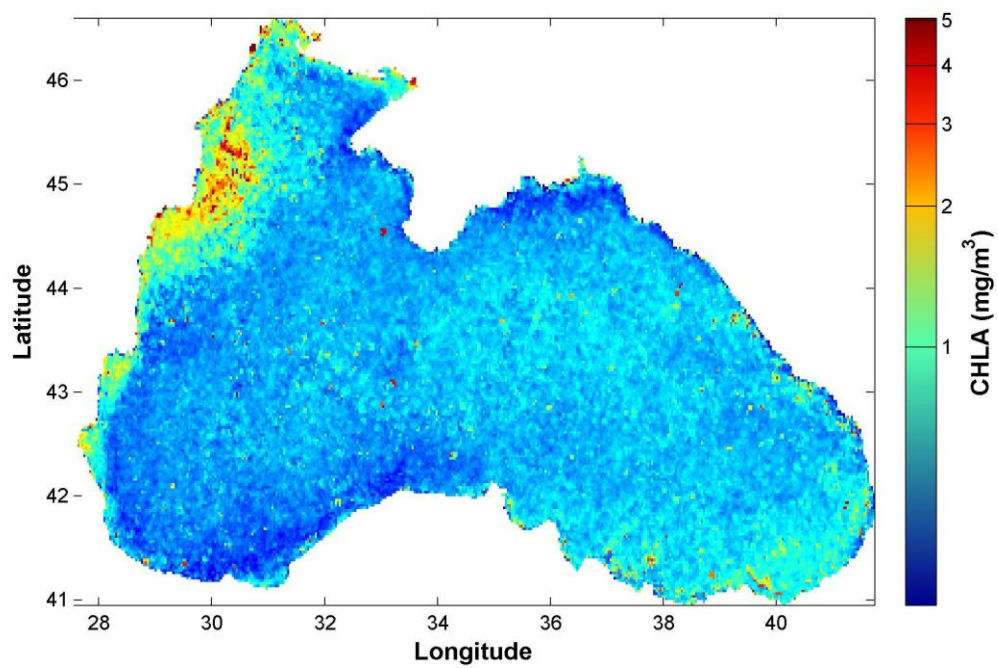


Figure 89. The climatological average of the chlorophyll-a concentration for February

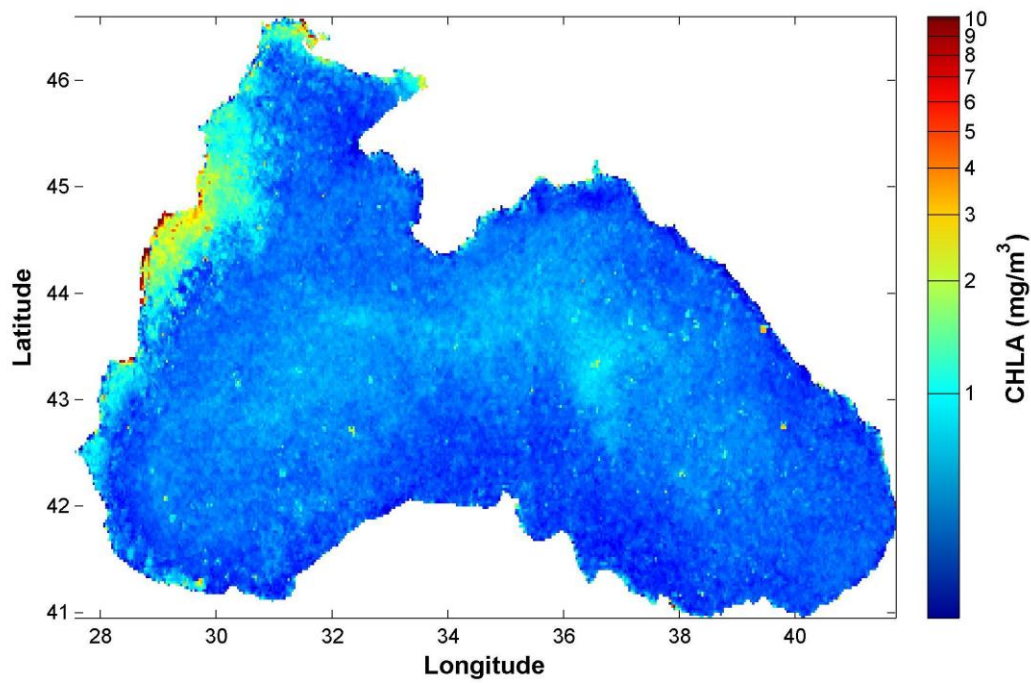


Figure 90. The climatological average of the chlorophyll-a concentration for March

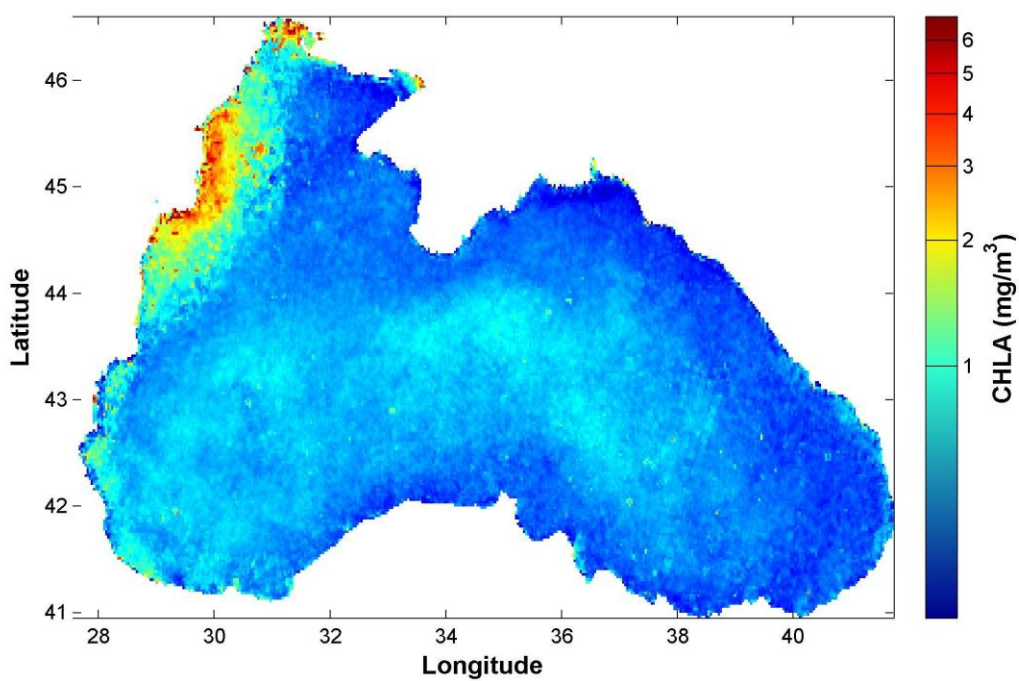


Figure 91. The climatological average of the chlorophyll-a concentration for April

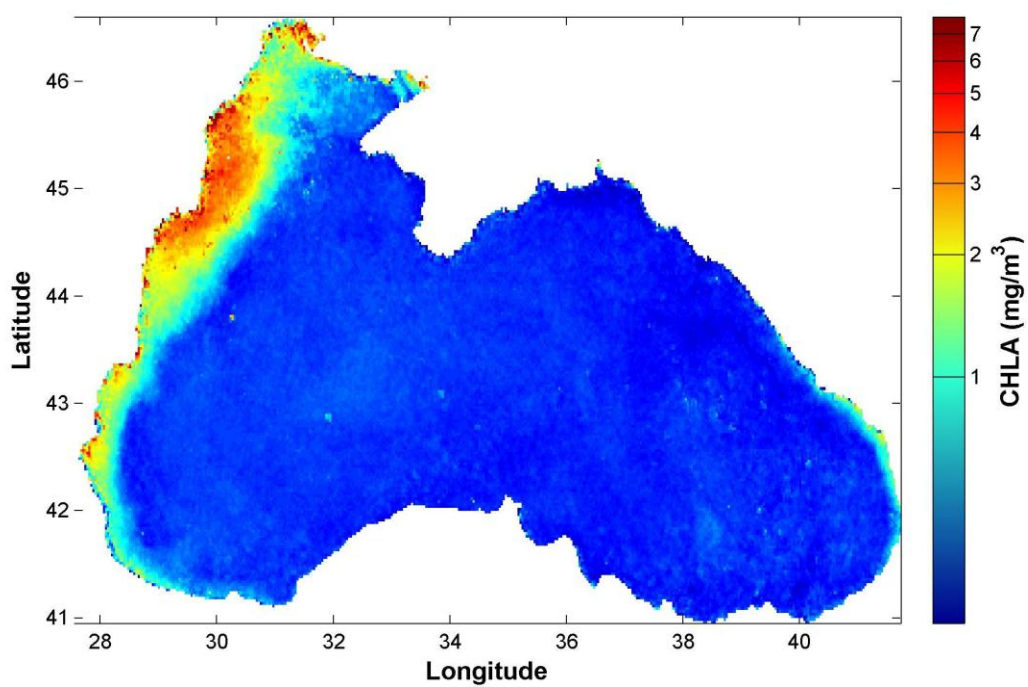


Figure 92. The climatological average of the chlorophyll-a concentration for May

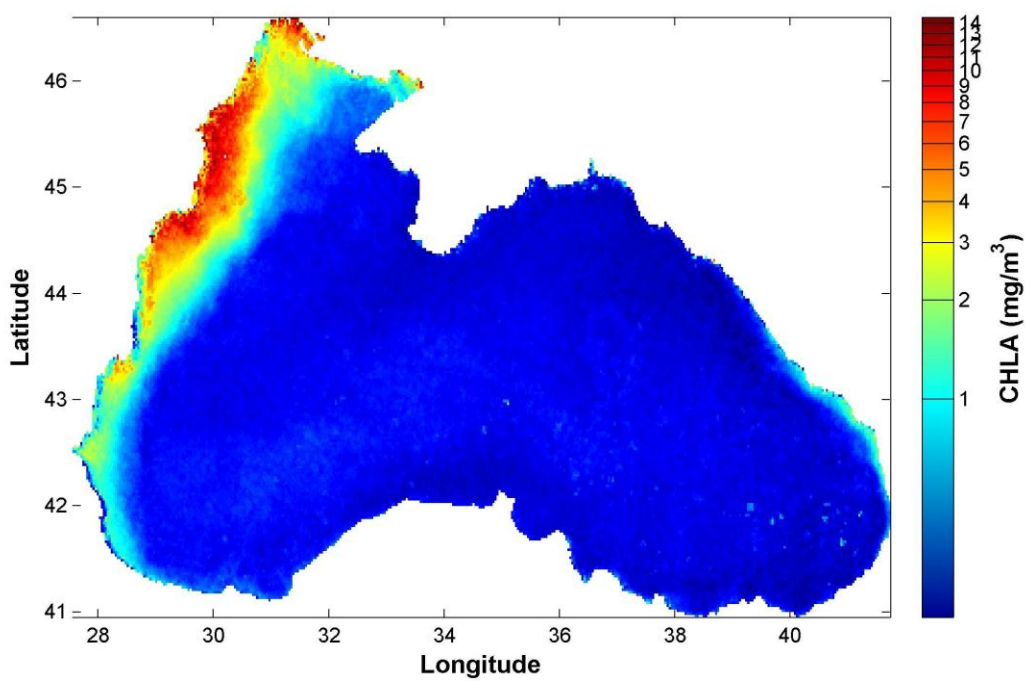


Figure 93. The climatological average of the chlorophyll-a concentration for June

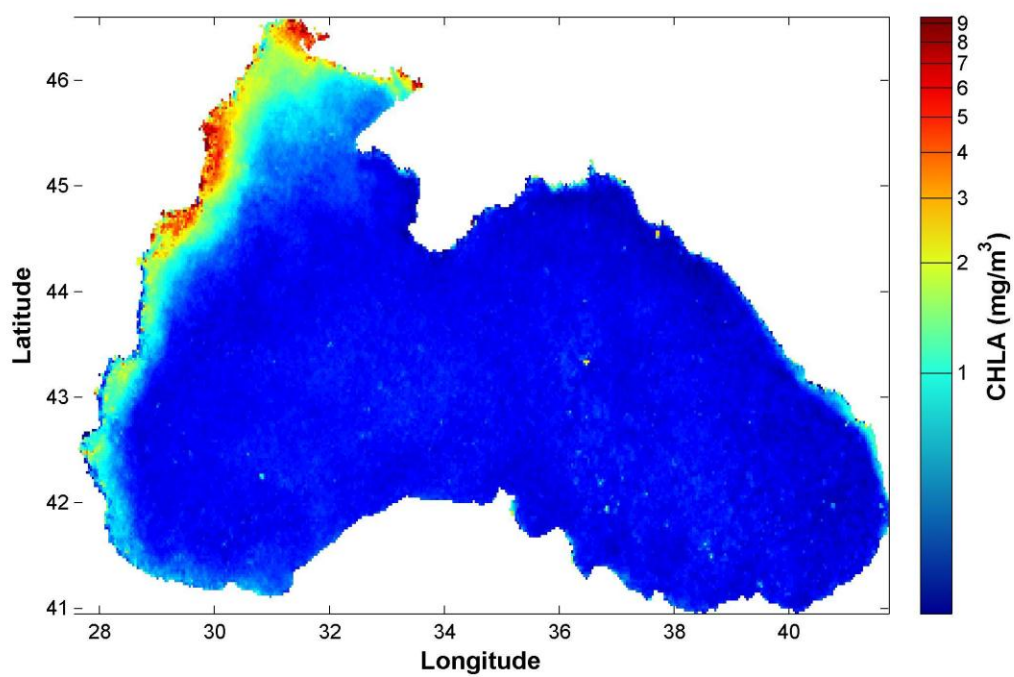


Figure 94. The climatological average of the chlorophyll-a concentration for July

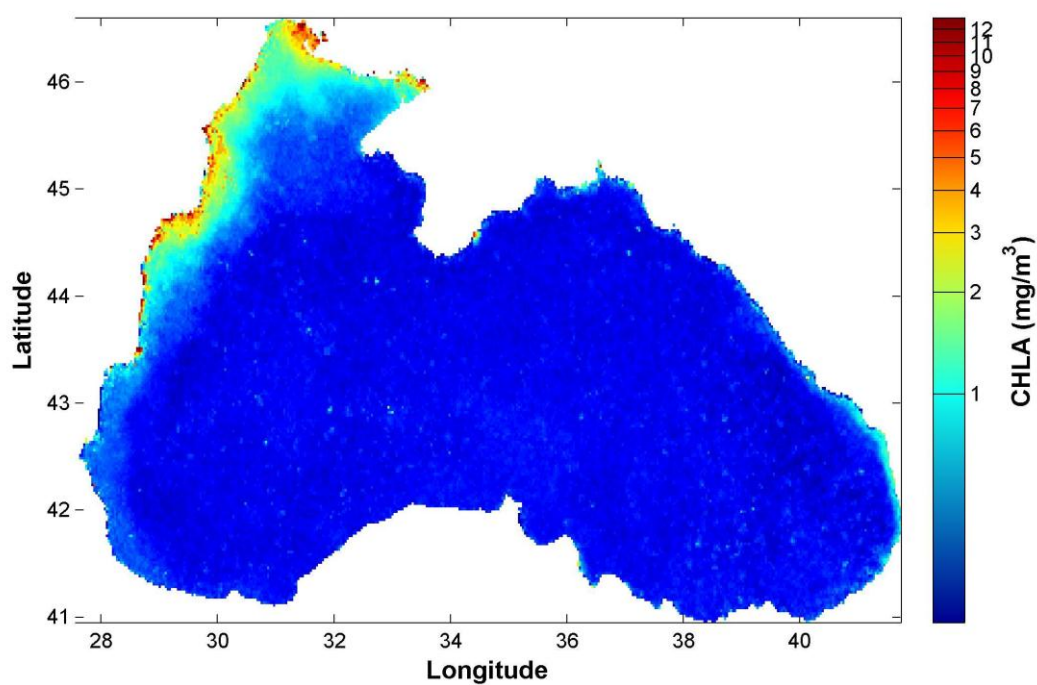


Figure 95. The climatological average of the chlorophyll-a concentration for August

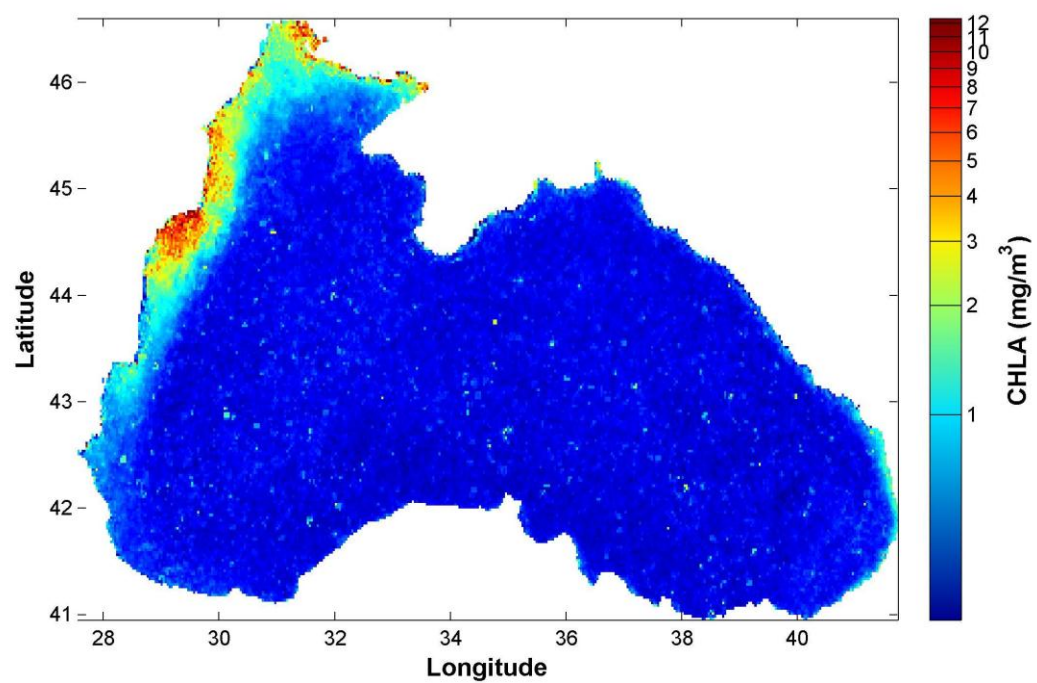


Figure 96. The climatological average of the chlorophyll-a concentration for September

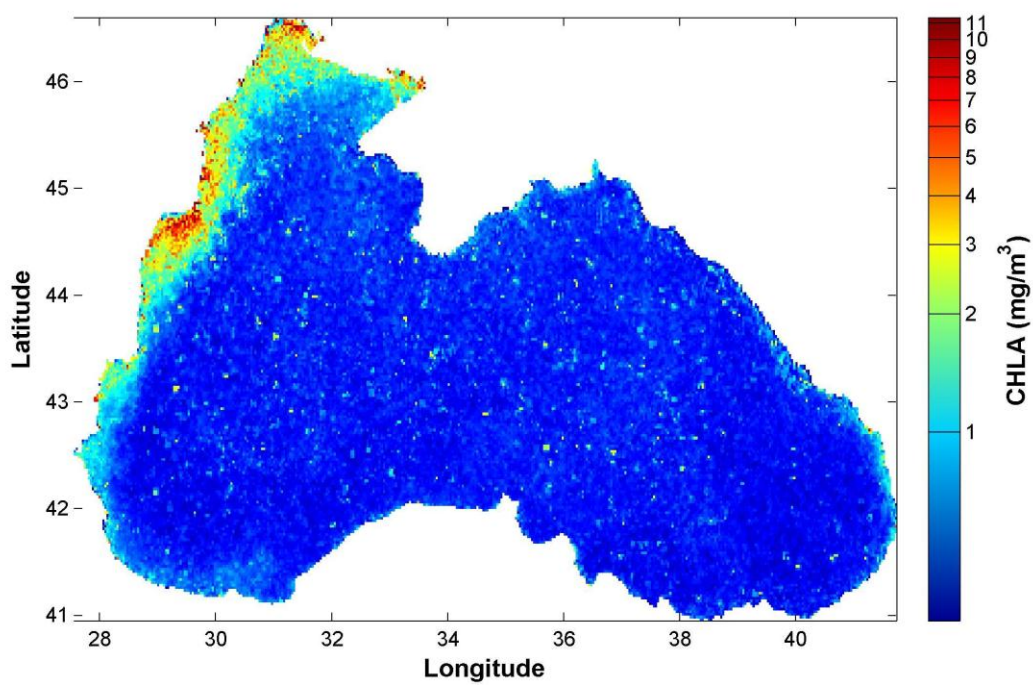


Figure 97. The climatological average of the chlorophyll-a concentration for October

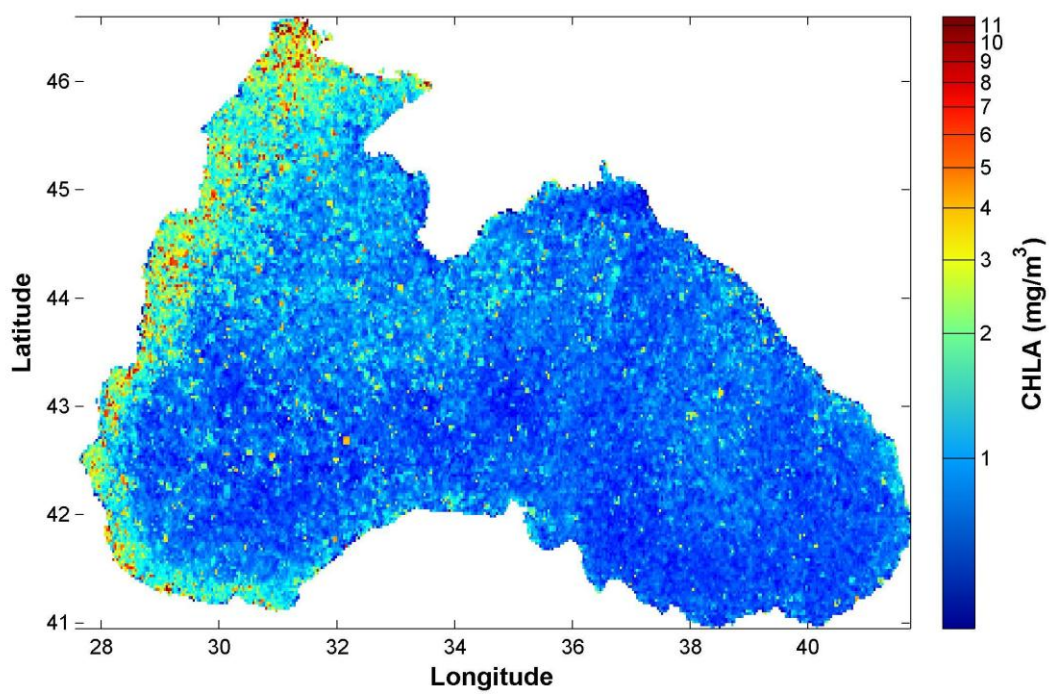


Figure 98. The climatological average of the chlorophyll-a concentration for November

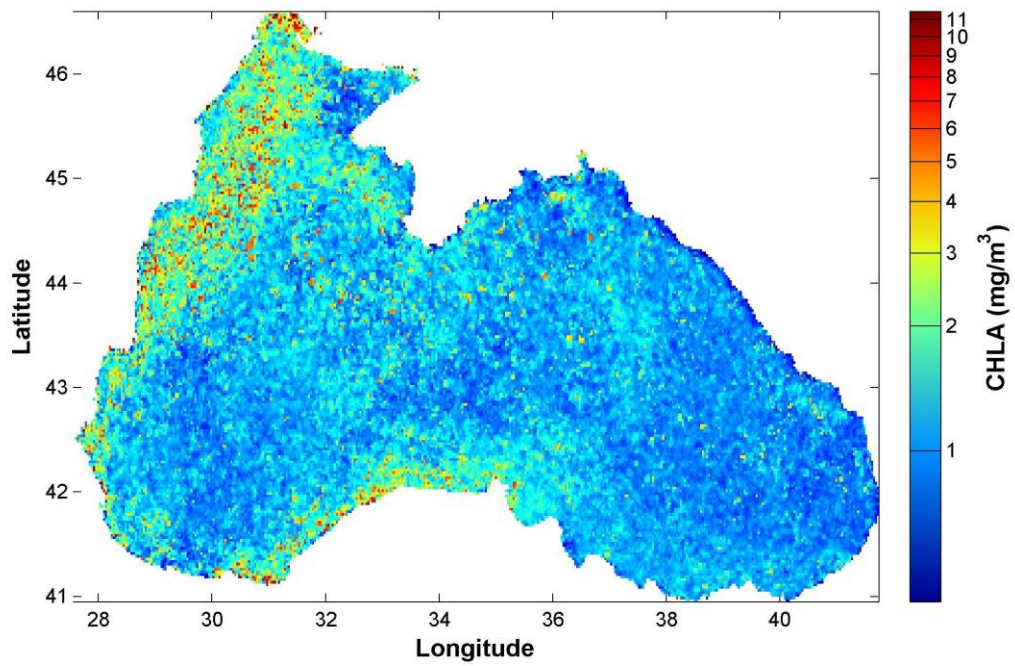


Figure 99. The climatological average of the chlorophyll-a concentration for December

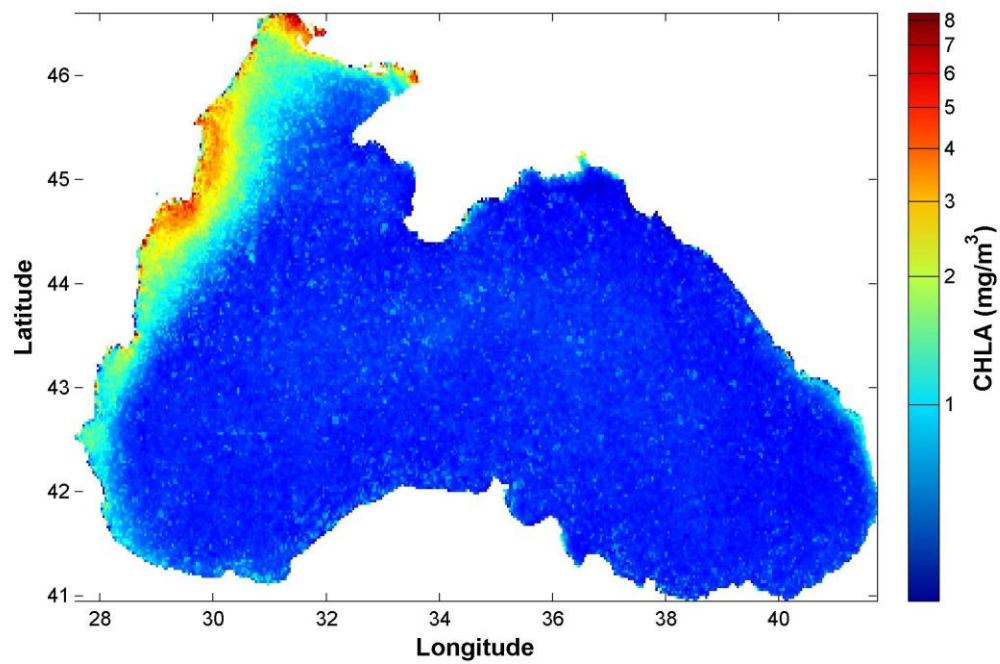


Figure 100. The climatological average of the chlorophyll-a concentration from 2000 to 2009

Figure 101 shows the horizontally averaged East and West relative vortices, with the chlorophyll-a concentration superimposed. As seen in the figure, Pattern 6 is characterized by low chlorophyll-a concentration levels. Aside from this relation, there is no indication of any influence of the vorticity of recurrent surface patterns on chlorophyll-a concentrations. Likewise, Figure 103 shows monthly anomalies in the components of zonal and meridional winds, with the chlorophyll-a concentration superimposed. Bahamon et al. (2010) state that there is no significant correlation between the wind and the chlorophyll-a level, and this research confirms that result. There is no significant separation of the recurrent patterns of the wind with chlorophyll-a concentration superimposed.

Figure 102 and Table 11 are provided to allow a deeper understanding of the correlation between the recurrent patterns in relation to both spring and fall blooms of chlorophyll-a concentrations. According to the figure and table, Pattern 4 (Cyclonic RIM Current and Cyclonic Batumi Eddy) dominates most of the fall blooms. Apart from that, there is no indication of any correlation concerning the spring blooms. Similarly, Figure 104 and Table 12 show the same kind of relation between the recurrent patterns of the surface wind and the chlorophyll-a concentration. But this time, none of the recurrent patterns stand out and the distribution is random.

Chu et al. (2005) used the optimal spectral decomposition (OSD) to reconstruct seasonal variability of the Black Sea's horizontally averaged chlorophyll-a concentration from data collected during the NATO SfP-971818 Black Sea Project in 1980-1995. According to their study, there are two blooms in the Black Sea. The first bloom is the winter/spring bloom which takes place in February and March, and terminates at the end of April. The second bloom is the fall bloom which occurs due to an increase in the surface chlorophyll-a concentration during late September. The fall bloom reaches its maximum in October and has half the intensity of the winter/spring bloom. Chu et al.'s finding contradicts the results of this research, which determined that each year the fall bloom is significantly more intense than the winter/spring bloom. These varying findings can be explained either by the difference in the data sets used (in situ data versus satellite data) or the difference in the time periods during which each study occurred. Figure 105

shows the two-bloom structure of the surface chlorophyll-a concentration Chu et al. discovered, and Figure 106 shows the distribution of the observational stations they used during their study.

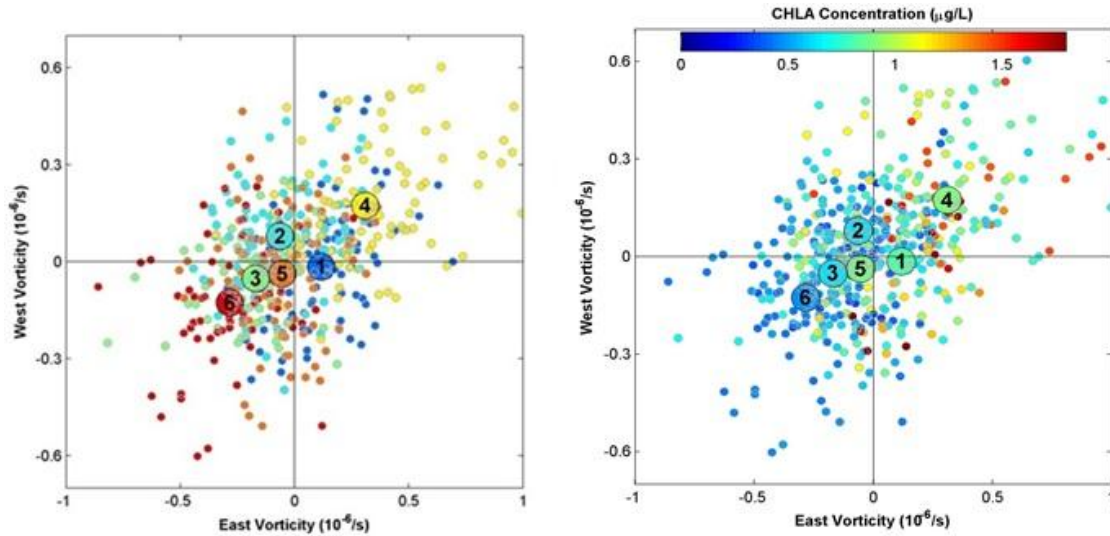


Figure 101. (a) Horizontally averaged East and West relative vorticities, with (b) chlorophyll-a concentration superimposed. Small circles represent the monthly anomalies of the basin scale averaged zonal component of the vorticity of the surface currents from 2000 to 2009. Larger circles indicate the recurrent spatial patterns identified by the SOM analysis that are illustrated in Figures 46 – 51. The basin average chlorophyll-a anomaly is superimposed.

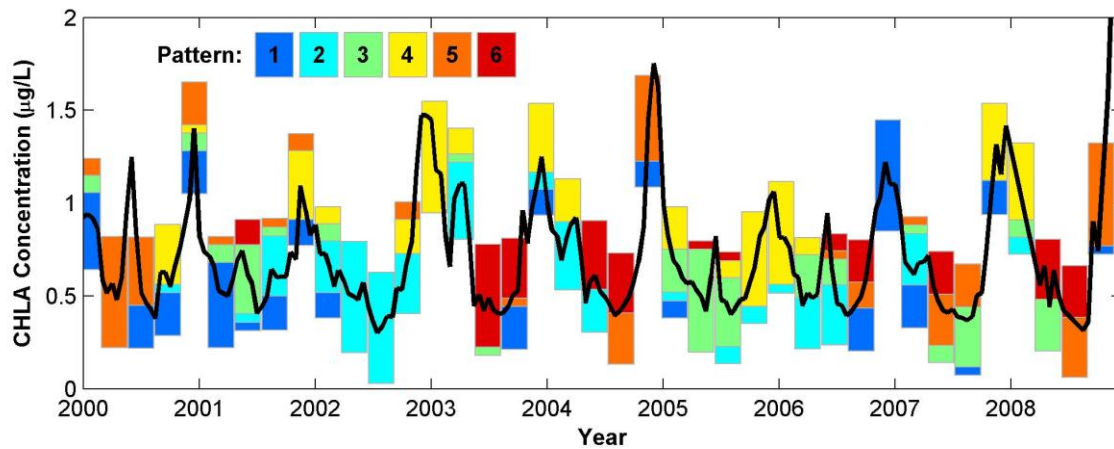


Figure 102. Temporal evolution of the chlorophyll-a concentrations from 1999 – 2009. In order to assess the correlation with the surface currents, the bars represent the contribution of the recurrent patterns for each three-month period.

Table 11. Distribution of the occurrence rates of the surface current patterns with respect to the spring and fall blooms of the chlorophyll-a concentrations

YEAR	BLOOM	SURFACE CURRENT PATTERNS					
		1	2	3	4	5	6
2000	<i>Spring</i>	20 %	-	-	-	80 %	-
	Fall	40 %	-	15 %	5 %	40 %	-
2001	<i>Spring</i>	5 %	5 %	65 %	-	-	25 %
	Fall	20 %	-	-	65 %	15 %	-
2002	<i>Spring</i>	-	100 %	-	-	-	-
	Fall	-	-	-	100 %	-	-
2003	<i>Spring</i>	-	70 %	5 %	25 %	-	-
	Fall	25 %	15 %	-	60 %	-	-
2004	<i>Spring</i>	-	65 %	-	35 %	-	-
	Fall	20 %	-	-	-	80 %	-
2005	<i>Spring</i>	-	-	95 %	-	-	5 %
	Fall	-	5 %	-	95 %	-	-
2006	<i>Spring</i>	-	55 %	25 %	-	5 %	15 %
	Fall	100 %	-	-	-	-	-
2007	<i>Spring</i>	40 %	50 %	5 %	-	5 %	-
	Fall	30 %	-	-	70 %	-	-
2008	<i>Spring</i>	-	-	45 %	-	-	55 %
	Fall	5 %	-	-	-	95 %	-

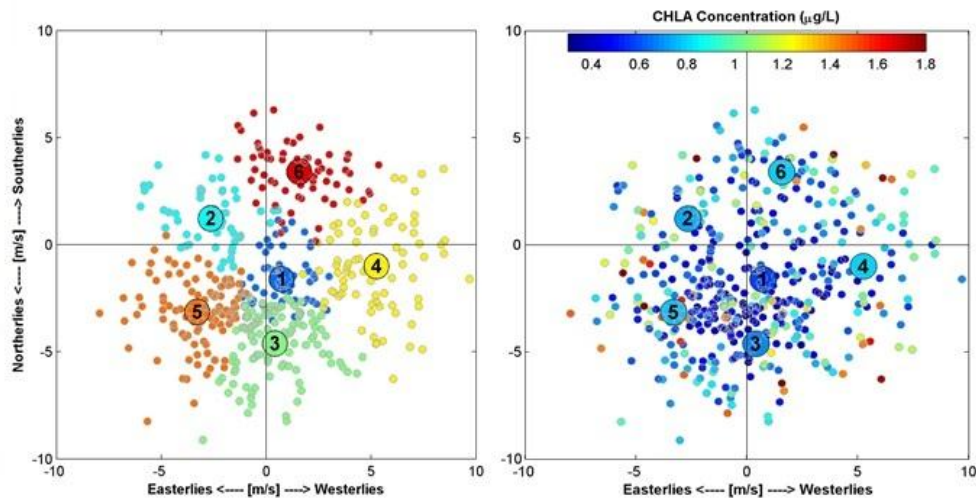


Figure 103. In the right panel, small circles represent the monthly anomalies of the basin scale averaged meridional and zonal components of the winds from 2000 to 2009. Larger circles indicate the recurrent spatial patterns identified by the SOM analysis that are illustrated in Figures 74 – 79. The basin average chlorophyll anomaly is superimposed.

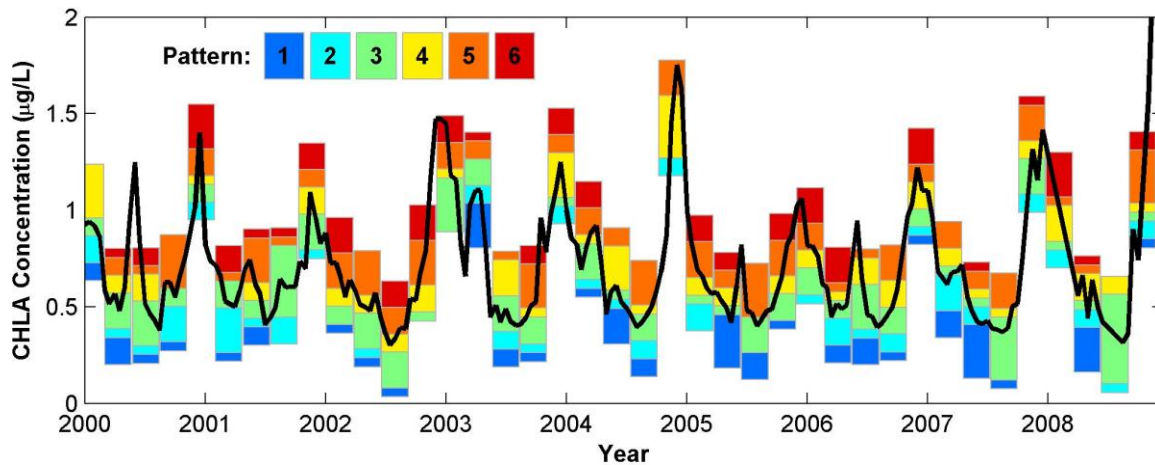


Figure 104. Temporal evolution of the chlorophyll-a concentrations from 1999 – 2009. In order to assess the correlation with the surface winds, the bars represent the contribution of the recurrent patterns for each three-month period.

Table 12. Distribution of the occurrence rates of the recurrent patterns with respect to the spring and fall blooms of the chlorophyll-a concentrations.

YEAR	BLOOM	RECURRENT PATTERNS					
		1	2	3	4	5	6
2000	Spring	20 %	5 %	35 %	20 %	10 %	10 %
	Fall	-	15 %	15 %	5 %	25 %	40 %
2001	Spring	15 %	5 %	15 %	15 %	45 %	5 %
	Fall	-	5 %	35 %	25 %	15 %	20 %
2002	Spring	10 %	10 %	30 %	20 %	30 %	-
	Fall	-	-	50 %	5 %	25 %	20 %
2003	Spring	40 %	15 %	25 %	-	15 %	5 %
	Fall	-	15 %	5 %	40 %	15 %	25 %
2004	Spring	5 %	5 %	45 %	5 %	20 %	20 %
	Fall	-	15 %	-	55 %	30 %	-
2005	Spring	45 %	-	5 %	20 %	15 %	15 %
	Fall	-	5 %	35 %	10 %	20 %	30 %
2006	Spring	25 %	5 %	40 %	25 %	5 %	-
	Fall	5 %	5 %	15 %	25 %	15 %	35 %
2007	Spring	20 %	45 %	-	15 %	20 %	-
	Fall	-	15 %	35 %	15 %	30 %	5 %
2008	Spring	40 %	20 %	5 %	25 %	5 %	5 %
	Fall	5 %	25 %	5 %	5 %	45 %	20 %

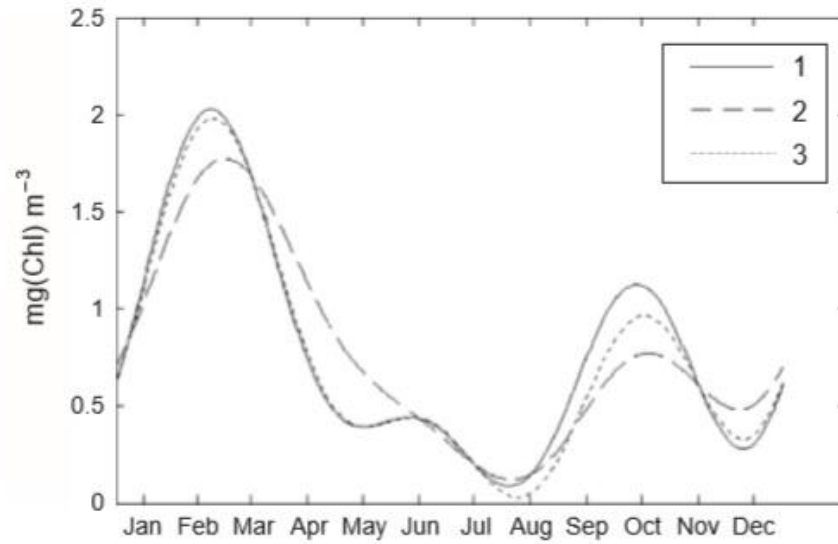


Figure 105. Sensitivity of the temporal interruption on chlorophyll-a concentration using (1) all data, (2) all data except April, and (3) all data except August (from Chu et al. 2005).

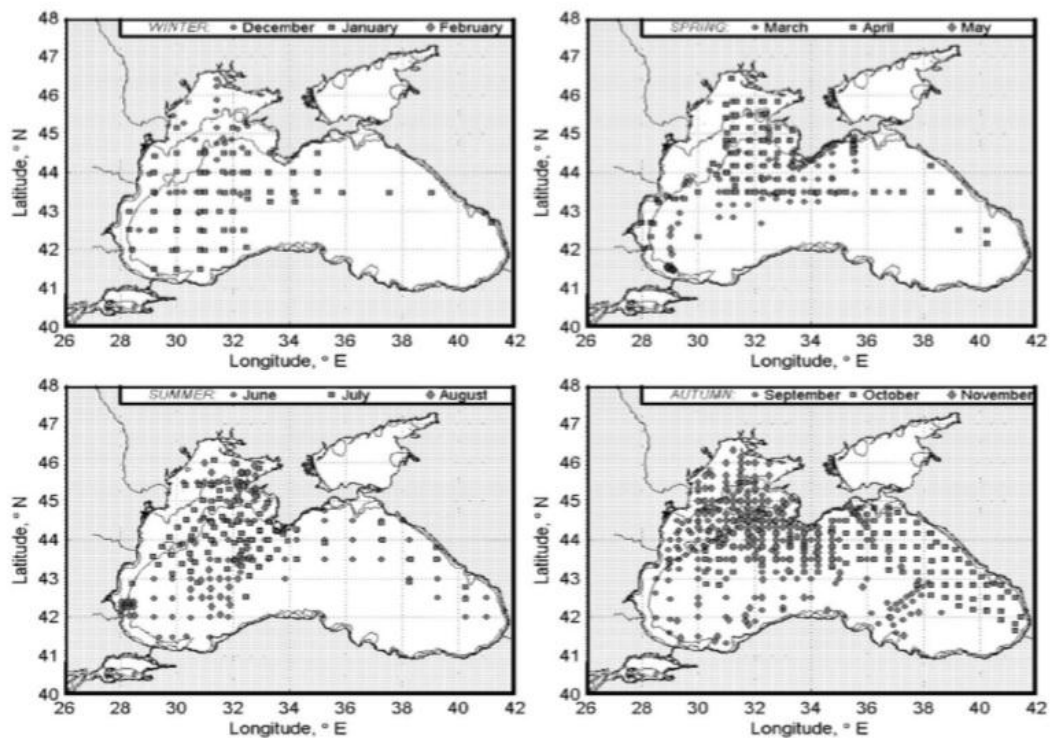


Figure 106. Distribution of observational stations: (a) winter, (b) spring, (c) summer, and (d) fall (from Chu et al. 2005).

THIS PAGE INTENTIONALLY LEFT BLANK

VIII. CONCLUSIONS

Surface geostrophic velocity data from 1999 to 2009 were obtained from AVISO to provide data on the surface currents. Their monthly means show the seasonal variation of the surface currents. Six patterns were found after conducting the SOM. The inter-annual variability of the surface currents was also obtained. The first pattern (Sevastopol Cyclonic and Batumi Dipole Eddies) represents more than 20% of the whole data set. In this pattern, the Batumi dipole eddies are located at the southeastern corner of the basin. At the northwestern corner of the basin, the cyclonic Sevastopol eddy is evident. The general circulation is comprised of two main gyres. The western main gyre is anti-cyclonic and weak. The eastern main gyre, on the other hand, is cyclonic and strong. The northerly boundary current forms in the west. No eddy formation is observed in the open parts of the basin. More than 16% of the data set is represented by the second pattern (Cyclonic RIM Current and Anti-cyclonic Batumi Eddy). The main feature of this pattern is the strong, anti-cyclonic Batumi eddy. Apart from the Batumi eddy, no other eddy structure, including the major Sevastopol eddy, is observed. The general circulation is formed by the strong and cyclonic RIM current. The open parts of the basin are relatively calm as opposed to the coastal regions. Therefore, this particular pattern is mostly dominated by the RIM current. The third pattern (Anti-cyclonic Sevastopol and Batumi Eddies) also represents almost 16% of the whole data set. The major eddies of the basin are the Batumi and Sevastopol eddies. Both of these major eddies are strong and anti-cyclonic. The RIM current does not appear which means that the general circulation is formed by the western and eastern main gyres. In the northeastern corner, the weak Caucasus eddy exists, while the strong northerly boundary current is present in the west. The fourth pattern (Cyclonic RIM Current and Cyclonic Batumi Eddy) comprises more than 20% of the whole representation of the data set. In this pattern the Black Sea basin is almost entirely dominated by the strong cyclonic RIM current. The open parts of the sea stay relatively calm and the very weak cyclonic Batumi eddy is detected but it is nearly absorbed by the RIM current. The fifth pattern (Anti-cyclonic RIM Current and Batumi Dipole Eddies) represents 15% of the whole data set and it demonstrates a basin-wide,

chaotic environment. At the southeastern corner the Batumi dipole eddies occur. The weak, anti-cyclonic Crimea eddy is observed in the north, whereas the Sevastopol eddy disappears. The general circulation is formed by the strong, anti-cyclonic RIM current. More than 10% of the total representation for the data set is covered by the sixth pattern (Anti-cyclonic RIM Current and Multi Eddies). The southeastern corner of the basin is entirely dominated by the strong, anti-cyclonic Batumi eddy. At the north of the Batumi eddy, the cyclonic Suchumi eddy is detected. The weak, anti-cyclonic Kerch eddy is observed in the north. At the northwestern corner the strong anti-cyclonic Sevastopol eddy forms. The general circulation is comprised of the strong, anti-cyclonic RIM current.

The rate of occurrence of the six patterns was computed. Pattern 1 is one of the two patterns that dominate during winter-like and fall-like months. Its maximum contribution is in January with ~45% and it disappears completely in June. Pattern 2 is more likely to be observed during the spring. Its maximum contribution is detected in April with more than 50%. It declines in winter-like months, and it completely disappears in June. Pattern 3 tends to appear towards the end of the spring and the beginning of the summer. It reaches its maximum in May and becomes the pattern most likely to appear during that time of the year. The first three months of the year are dominated by the Pattern 4. It tends to appear strongly during cold periods, whereas during warm periods it exhibits a weak contribution. Pattern 4 disappears in May and doesn't appear again until September. Despite the fact that Pattern 5 shows maximum percentages in fall-like months and dominates in October, it has no significant seasonality and occurs occasionally throughout the year. Pattern 6 completely disappears from November to April, and appears only five months during the year. It dominates the period from June to September and reaches its maximum in July. With more than 40% contribution, it becomes the pattern most likely to be detected in July. The EAWR index and the ENSO index are detected significantly negative during months mapped towards pattern 5, which indicates that the occurrence of pattern 5 is promoted by these indices. On the other hand, ENSO index is detected significantly positive during months mapped towards pattern 2 and therefore influence the surface current structure.

The wind data from 1992 to 2012 were obtained from QuikSCAT. This data is representative of the winds near the surface of the Black Sea. The data provides monthly means that show the seasonal variation of the surface currents. After conducting the SOM, six patterns were found. Five out of these six recurrent patterns perfectly match with the results of the study of Arthur et al. (2012). Additionally, the inter-annual variability of the winds was obtained. This research focused on the time frame from 1999 to 2009.

The first pattern (The Northerly Winds and the Cyclonic Curve in the Western Shelf) represents more than 13% of the whole data set. In this pattern, westerly winds are observed north of the western shelf. The winds curve anti-cyclonically and become northeasterly south of the western shelf. At the eastern self, on the other hand, the winds blow from the northwest with a slight cyclonic curve south of the eastern shelf. More than 13% of the total representation for the data set is covered by the second pattern (The Easterly Winds and the Anti-cyconic Curve in the Western Shelf). The main feature of this pattern is the anti-cyclonic curve of the winds in the western shelf. The winds blow from the east, starting at the eastern shelf, and from the central Black Sea region. The winds are stronger to the west and they are strongest north of the western shelf. The third pattern (The Dominance of the Strong Northerly Winds) represents 23% of the whole data set. The strong northerly winds almost completely dominate the Black Sea region. The winds lose their strength to the south of the eastern shelf and they exhibit a cyclonic curve in this region. The fourth pattern (The Northerly Winds in the West and the Westerly Winds in the East) comprises more than 16% of the whole representation of the data set. The western and eastern shelves exhibit two different wind characteristics. The strong northwesterly winds occur in the western shelf with a little anti-cyclonic curve to the south, whereas, starting from the central Black Sea, the winds blow from the west and the whole eastern shelf is dominated by the relatively weak easterly winds. The fifth pattern (The Dominance of the Strong Northeasterly Winds) represents more than 21% of the whole data set. The northeasterly winds dominate the whole Black Sea region with the exception of the southeastern corner of the basin. The winds become weaker to the southeast and almost disappear completely close to the coast. Almost 12% of the total

representation for the data set is covered by the sixth pattern (The Strong Southwesterly Winds). The southwesterly winds dominate the whole Black Sea region with the exception of the southeastern corner of the basin. The winds blowing from the southeast become weaker and they have a slight anti-cyclonic curve.

The rate of occurrence of the six patterns is computed. Pattern 1 clearly dominates during the summer when the weather warms up. Its maximum contribution is in June and it disappears completely in January and February. Pattern 2 is more likely to be observed during spring-like and fall-like months. Its maximum contribution is detected in May. This pattern declines in extreme weather conditions like the cold weather in winter and the warm weather in the summer. Pattern 3 tends to appear mostly during the second six-month period of the year. It reaches its maximum in August and becomes the pattern most likely to appear during that time of the year. It never disappears completely. Pattern 4 comprises the highest portion of the data set during the winter-like and summer-like months. It is the most dominant pattern in February. Pattern 4 gets very weak during the spring and shows an oscillatory pattern of contribution during the fall. Pattern 5 contributes significantly during the spring and fall. It reaches its maximum percentages in fall-like months and dominates in October. Pattern 6 has no significant seasonality and occurs occasionally throughout the year. It contributes the least among the six patterns from May to September. Pattern 6 is the pattern most likely to be detected in March. The EAWR index and the ENSO index are detected significantly negative during months mapped towards pattern 2, which indicates that the occurrence of pattern is promoted by these indices. On the other hand, NAO and EAWR indices are detected significantly positive during months mapped towards pattern 4 and therefore influence the wind anomaly.

According to the horizontally averaged East and West relative vortices, with the chlorophyll-a concentration superimposed, Pattern 6 is characterized by low chlorophyll-a concentration levels. Aside from this relation, there is no indication of any influence of the vorticity of recurrent surface patterns on chlorophyll-a concentration. On the other hand, the monthly anomalies in the components of zonal and meridional winds, with the chlorophyll-a concentration superimposed show no significant separation, hence no

significant correlation between the wind and the chlorophyll-a level. This finding confirms the study of Bahamon et al. (2010). Pattern 4 of the surface current data set dominates most of the fall blooms. Apart from that, there is no indication of any correlation concerning the spring blooms. On the other hand, none of the recurrent patterns of the wind data set stands out; therefore the distribution is determined as random.

Chu et al. (2005) found two blooms in the Black Sea using in-situ measurements in 1980-1995. The first bloom is the winter/spring bloom which takes place in February and March, and terminates at the end of April. The second bloom is the fall bloom which occurs due to an increase in the surface chlorophyll-a concentration during late September. The fall bloom reaches its maximum in October and has half the intensity of the winter/spring bloom. Our study shows the change of the bi-modal characteristics in 1999-2009 with the fall bloom being more significant than the spring bloom. The surface circulation Pattern 4 (cyclonic RIM current and Batumi eddy) is associated with the occurrence of the fall bloom. Evident connection of negative NAO and negative ENSO to the Pattern 4 circulation implies the large-scale atmospheric effect.

THIS PAGE INTENTIONALLY LEFT BLANK

LIST OF REFERENCES

- AI Junkie, cited 2013: Kohonen's Self Organizing Feature Maps. [Available online at <http://www.ai-junkie.com/ann/som/som1.html>.]
- Ainsworth, E.J., 1999: Visualization of ocean colour and temperature from multispectral imagery captured by the Japanese ADEOS satellite. *Journal of Visualization*, **2**, 195-204, ISSN: 1343-8875.
- Ainsworth, E.J. and Jones, I.S.F., 1999: Radiance spectra classification from the ocean color and temperature scanner on ADEOS. *IEEE Transaction on Geosciences Remote Sensing*, **37**, 1645-1656, ISSN: 0196-2892.
- Alpers, W., Ivanov, Y.A., and Dagestad, K.F., 2010: Investigation of coastal wind fields over the Black Sea using Envisat Synthetic Aperture radar images. ESA Living Planet Symposium, *ESA publication SP-686*, Bergen, June 28 – July 2, 2010.
- Alpers, W., Ivanov, A., and Horstmann, J., 2009: Observations of bora events over the Adriatic Sea and Black Sea by spaceborne synthetic aperture radar. *Mon. Wea. Rev.*, **137**(3), 1154-1165, DOI: 10.1175/2008MWR2563.1.
- Alpers, W., Pahl, U., and Gross, G., 1998: Katabatic wind fields in coastal areas studied by ERS-1 synthetic aperture radar imagery and numerical modeling. *J. Geophys. Res.*, **103**, 7875 -7886.
- Archiving, Validation, and Interpretation of Satellite Oceanographic data, cited 2013: What is AVISO? [Available online at http://www.aviso.oceanobs.com/no_cache/en/newsstand/newsletter/newsletter01/what-is-aviso/.]
- Archiving, Validation, and Interpretation of Satellite Oceanographic data, cited 2013: Altimetry. [Available online at <http://www.aviso.oceanobs.com/en/altimetry.html>.]
- Archiving, Validation, and Interpretation of Satellite Oceanographic data, cited 2013: Missions. [Available online at <http://www.aviso.oceanobs.com/en/missions.html>.]
- Archiving, Validation, and Interpretation of Satellite Oceanographic data, cited 2013: Black Sea (M)SLA – (Map of) Sea Level Anomalies and Geostrophic Velocity Anomalies. [Available online at <http://www.aviso.oceanobs.com/en/data/products/sea-surface-height-products/regional/msla-black-sea.html>.]

- Annas, S., Kanai, T., and Koyama, S., 2007: Principal component analysis and self-organizing map for visualizing and classifying fire risks in forest regions. *Agricultural Information Research*, **16**, 44-51, ISSN: 1881-5219.
- Astel, A., Tsakouski, S., Barbieri, P., and Simeonov, V., 2007: Comparison of self-organizing maps classification approach with cluster and principal components analysis for large environmental data sets. *Water Research*, **41**, 4566-4578, ISSN: 0043-1354.
- Bação, F., Lobo, V., and Painho, M., 2005: Self-organizing maps as substitutes for k-means clustering. *Lecture Notes in Computer Science*, V. S. Sunderam, G. v. Albada, P. Sloot, and J. J. Dongarra (Eds.), **3516**, 476-483, ISSN: 0302-9743, Springer-Verlag.
- Bahamon, N., Cruzado, A., Velasquez, Z., Bernardello, R., and Donis, D., Patterns of phytoplankton chlorophyll variability in the mediterranean and black seas.
- Berseneva, G.P., 1993: Sezonnaya dinamika kontsentratsii khlorofilla-a (Seasonal dynamics of chlorophyll-a concentration). In: Kovalev, A.V. and Finenko, Z.Z. (Eds.), *Plankton Chernogo Morya*, 92-109.
- Black Sea Scene, cited 2013: Unique Body of Water. [Available online at http://www.blackseascene.net/content/content.asp?menu=0040032_000000.]
- Borges, C., Gómez-Carracedo, M.P., Andrade, J.M., Duarte, M.F., Biscaya, J.L., and Aires-de-Sousa, J., 2010: Geographical classification of weathered crude oil samples with unsupervised self-organizing maps and a consensus criterion. *Chemometrics and Intelligent Laboratory Systems*, **101**, 43-55, ISSN: 0169-7439.
- Burman, E. A., 1969: *Local Winds (in Russian)*. Gidrometeoizdat, 342 p.
- Chu, P.C., Leonid M.I., and Tatyana M.M., 2005: Seasonal variability of the Black Sea chlorophyll-a concentration. *Journal of Marine Systems*, **56.3**, 243-261.
- Corchado, E., Baruaque, B., Mata, A., and Corchado, J.M., 2008: A WeVoS-CBR approach to oil spill problem. *Lecture Notes in Computer Science*, **5271**, 378-384, DOI: 10.1007/978-3-540-87656-4_47, ISSN : 0302-9743, Springer-Verlag.
- Davies, D.L., and Bouldin, D.W., 1979: A Cluster Separation Measure, *IEEE Transactions on Pattern Analysis and Machine Intelligence*. **2**, 224–227, doi:10.1109/TPAMI.1979.4766909.
- Dr. Saed Sayad, cited 2013: Self-organizing Map. [Available online at http://www.saedsayad.com/clustering_som.htm.]

- Eggermont, J., 1998: Rule-Extraction and Learning in the BP-SOM Architecture. Internal Report IR-98-16 (Master's Thesis), Leiden University.
- Fitzpatrick, D.W. (1997), cited 2013: Neural Net Primer: A Brief Introduction to the Use of Neural Networks Suitable for Futures Forecasting. [Available at <http://www.jurikres.com/down/nnprimer.txt>.]
- Geography, cited 2013: A Black Sea Journey [Available online at <http://www.ceoe.udel.edu/blacksea/geography/index.html>.]
- Ginzburg, A.I., Kostianoy, A.G., Soloviev, D.M., and Stanichny, S.V., 2000: Remotely sensed coastal/deep-basin water exchange processes in the Black Sea surface layer. In: Halpern, D. (Ed.), *Satellites, Oceanography and Society, Elsevier Oceanography Series*, **63**, 273-287, Elsevier Sciences.
- Gregoire, M., Soetaert, K., Nezlin, N., and Kostianoy, A., 2004: Modelling the nitrogen cycling and plankton productivity in the Black Sea using a three-dimensional interdisciplinary model. *Journal of Geophysical Research*, **109** (C05007), DOI: 10.1029/2001JC001014.
- Gusev, A.M. (Ed.), 1959: Novorossiyskaya Bora (in Russian). *Proceedings of Marine Hydrophysical Institute ANUSSR*, **14**, 157.
- Guthikonda, S.M., 2005: Kohonen Self-Organizing Maps. Wittenberg University.
- Hardman-Mountford, N.J., Richardson, A.J., Boyer, D.C., Kreiner, A., and Boyer, H. J., 2003: Relating sardine recruitment in the northern Benguela to satellite-derived sea surface height using a neural network pattern recognition approach. *Progress in Oceanography*, **59**, 241-255, ISSN: 0079-6611.
- Iskandar, I., 2009: Variability of satellite-observed sea surface height in the tropical Indian Ocean: comparison of EOF and SOM Analysis. *Makara Seri Sains*, **13**, 173-179, ISSN: 1693-6671.
- James Matthews, cited 2013: Self Organizing Map AI for Pictures. [Available online at <http://www.generation5.org/content/2004/aiSomPic.asp>.]
- Kohonen, T., 1988: *Self-Organization and Associative Memory*. Springer-Verlag, ISBN: 0-387-18314-0.
- Kohonen, T., 2001: *Self-Organizing Maps*. Springer-Verlag, ISBN: 3-540-67921-9.
- Kordzadze, A.A., Demetrashvili, D.I., and Surmava, A.A., 2007: About circulation in the Black Sea at very strong and weak winds (in Russian). *Meteorologiya i Gidrologiya*, **9**, 58-64.

- Kopelevich, O.V., Sheberstov, S.V., Yunev, O., Basturk, O., Finenko, Z.Z., Nikonov, S., and Vedernikov, V.I., 2002: Surface chlorophyll in the Black Sea over 1978–1986 derived from satellite and in situ data. *Journal of marine systems*, **36**(3), 145-160.
- Korotaev, G., Oguz, T., Nikiforov, A., and Koblinsky, C., 2003: Seasonal, interannual, and mesoscale variability of the Black Sea upper layer circulation derived from altimeter data. *Journal of Geophysical Research*, **108** (C4), 3122.
- Korotaev, G.K., Saenko, O.A., and Koblinsky, C.J., 2001: Satellite altimetry observations of the Black Sea level. *Journal of Geophysical Research*, **106** (C1), 917–933.
- Lin, G.F., and Chen, L.H., 2006: Identification of homogeneous regions for regional frequency analysis using the self-organizing map. *Journal of Hydrology*, **324**, 1-9, ISSN: 0022-1694.
- Liu, Y., and Weisberg, R.H., 2005: Patterns of ocean current variability on the West Florida Shelf using the self-organizing map. *Journal of Geophysical Research*, **110**, C06003, DOI: 10.1029/2004JC002786, ISSN: 0148-0227.
- Liu, Y., and Weisberg, R.H., 2007: Ocean currents and sea surface heights estimated across the West Florida Shelf. *Journal of Physical Oceanography*. **37**, 1697-1713, ISSN: 0022-3670.
- Liu Y., and Weisberg R.H., 2011: *A Review of Self-Organizing Map Applications in Meteorology and Oceanography, Self-Organizing Maps, Applications and Novel Algorithm Design*. InTech, Dr. Josphat Igadwa Mwasiagi (Ed.), ISBN: 978-953-307-546-4, DOI: 10.5772/13146.
- Liu, Y., MacCready, P., and Hickey, B.M., 2009: Columbia River plume patterns in summer 2004 as revealed by a hindcast coastal ocean circulation model. *Geophysical Research Letters*, **36**, L02601, DOI: 10.1029/2008GL036447, ISSN: 0094-8276.
- Liu, Y., Weisberg, R.H., and Mooers, C.N.K., 2006: Performance evaluation of the self-organizing map for feature extraction. *Journal of Geophysical Research*, **111**, C05018, DOI: 10.1029/2005JC003117, ISSN: 0148-0227.
- Liu, Y., Weisberg, R.H., and Yuan, Y., 2008: Patterns of upper layer circulation variability in the South China Sea from satellite altimetry using the Self-Organizing Map. *Acta Oceanologica Sinica*, **27**(Supp.), 129-144, ISSN: 1869-1099.

- Lobo, V.J.A.S., 2009: Application of Self-Organizing Maps to the Maritime Environment, In: Information Fusion and Geographic Information Systems. *Lecture Notes in Geoinformation and Cartography*, 19-36, Popovich et al, (Eds.), ISSN: 1863-2246, Springer-Verlag.
- Mata, A., Corchado, E., and Baroque, B., 2009: Solving the Oil Spill Problem Using a Combination of CBR and a Summarization of SOM Ensembles. *Advances in Soft Computing*, **50**, 658-662, DOI: 10.1007/978-3-540-85863-8_78, ISSN: 1860-0794.
- Maung, P.P., 2012: Augmented Reality using a Neural Network. Ripon College.
- Minsky, M., and Papert, S., 1969: *Perceptrons*. MIT Press, Cambridge.
- National Aeronautics and Space Administration, cited 2013: Background. [Available online at http://oceancolor.gsfc.nasa.gov/seawifs/background/seawifs_background.html.]
- National Aeronautics and Space Administration, cited 2013: Detailed Description. [Available online at http://oceancolor.gsfc.nasa.gov/seawifs/background/seawifs_970_brochure.html.]
- National Aeronautics and Space Administration, cited 2013: An Overview of SeaWiFS and the SeaStar Spacecraft. [Available online at <http://oceancolor.gsfc.nasa.gov/seawifs/seastar/spacecraft.html>.]
- National Aeronautics and Space Administration, cited 2013: Introduction. [Available online at <http://winds.jpl.nasa.gov/aboutScat/index.cfm>.]
- National Aeronautics and Space Administration, cited 2013: A History of Scatterometry. [Available online at <http://winds.jpl.nasa.gov/aboutScat/history.cfm>.]
- National Aeronautics and Space Administration, cited 2013: Missions – SeaWinds on QuikSCAT. [Available online at <http://winds.jpl.nasa.gov/missions/quikscat/#mission>.]
- National Aeronautics and Space Administration, cited 2013: A History of Scatterometry. [Available online at <http://winds.jpl.nasa.gov/aboutScat/history.cfm>.]
- Nezlin, N.P., Kostyanoy, A.G., and Gregoire, M., 1999: Patterns of seasonal and interannual changes of surface chlorophyll concentration in the Black Sea revealed from the remote sensed data. *Remote Sens. Environ.*, **69**, 43-55.
- Niang, A., Gross, L., Thiria, L., Badran, F., and Moulin, C., 2003: Automatic neural classification of ocean colour reflectance spectra at the top of the atmosphere with introduction of expert knowledge. *Remote Sensing of Environment*, **86**, 257-271, ISSN: 0034-4257, DOI: 10.1016/S0034-4257(03)00113-5.

- NOAA Climate Prediction Center, cited 2013: Northern Hemisphere Teleconnection indices. [Available online at <http://www.cpc.ncep.noaa.gov/data/teledoc/telecontents.shtml>.]
- Noyes, J.L., 1992: *Artificial Intelligence with Common Lisp: Fundamentals of Symbolic and Numeric Processing*. D.C. Heath, Lexington, MA.
- Oguz, T.V., Aubrey, D.G., Latun, V.S., Demirov, E., Koveshnikov, L., Sur, H.I., Diaconu, V.S., Besiktepe, S., Duman, M., Limeburner, R., and Ereemeev, V., 1994: Mesoscale circulation and thermohaline structure of the Black Sea observed during HydroBlack '91. *Deep-Sea Research I*, **41**, 603-628.
- Oguz, T., La Violette, P.E., and Unluata, U., 1992: The upper layer circulation of the Black Sea: its variability as inferred from hydrographic and satellite observations. *Journal of Geophysical Research*, **97 (C8)**, 12569-12584.
- Oguz, T.V., Latun, V.S., Latif, M.A., Vladimirov, V.V., Sur, H.I., Markov, A.A., Ozsoy, E., Kotovshchikov, V.V., Ereemeev, V.V., and Unluata, U., 1993: Circulation in the surface and intermediate layer of the Black Sea. *Deep-Sea Research I*, **40**, 1597-1612.
- Oguz, T., Malanotte-Rizzoli, P., and Aubrey, D., 1995: Winds and thermohaline circulation of the Black Sea driven by yearly mean climatology forcing. *Journal of Geophysical Research*, **100 (C4)**, 6845-6863.
- Petrou, M., 2004: Special issue – Pattern Recognition for Remote Sensing (PRRS 2002) Preface. *Pattern Recognition Letters*, **25**, 1459, ISSN: 0167-8655.
- Poulain, P.M., Barbanti, R., Motyzhev, S., and Zatsepin, A., 2005: Statistical description of the Black Sea near-surface circulation using drifters in 1999–2003. *Deep Sea Research Part I: Oceanographic Research Papers*, **52**, Issue 12, 2250-2274, ISSN: 0967-0637, 10.1016/j.dsr.2005.08.007. [Available at <http://www.sciencedirect.com/science/article/pii/S0967063705002293>]
- Pyle, D., 1999: *Data Preparation for Data Mining*. Morgan Kaufmann Publishers.
- Rachev, N.H., and Stanev, E.V., 1997: Eddy processes in semienclosed seas: a case study for the Black Sea. *Journal of Physical Oceanography*, **27**, 1581-1600.
- Reusch, D.B., Alley, R.B., and Hewitson, B.C., 2005: Relative performance of self-organizing maps and principal component analysis in pattern extraction from synthetic climatological data. *Polar Geography*, **29**, 188-212, ISSN: 1939-0513.

- Richardson, A.J., Risien, C., and Shillington, F. A., 2003: Using self-organizing maps to identify patterns in satellite imagery. *Progress in Oceanography*, **59**, 223-239, ISSN: 0079-6611.
- Risien, C.M., Reason, C.J.C., Shillington, F.A., and Chelton, D.B., 2004: Variability in satellite winds over the Benguela upwelling system during 1999-2000. *Journal of Geophysical Research*, **109**, C03010, DOI: 10.1029/2003JC001880, ISSN: 0148-0227.
- Rosenblatt, F., 1957: The Perceptron - a perceiving and recognizing automaton. Report 85-460-1, Cornell Aeronautical Laboratory.
- Saraceno, M., Provost, C., and Lebbah M., 2006: Biophysical regions identification using an artificial neuronal network: A case study in the South Western Atlantic. *Advances in Space Research*, **37**, 793-805, ISSN: 273-1177.
- Shushkina, E.A., and Vinogradov, M.E., 1991: Izmeneniya planktonnogo soobshchestva otkrytykh raionov Chernogo morya i vozdeistvie na nego grebnevika Mnemiopsis (1978-1989), In: Vinogradov, M.E. (Ed.), *Izmenchivost ekosistemy Chernogo morya: Estestvennye i antropogennye factory*. Nauka, Moscow, pp. 248-261 (in Russian with English Abstract).
- Stanev, E.V., 1990: On the mechanisms of the Black Sea circulation. *Earth-Science Reviews*, **28**, 285-319.
- Stanev, E.V., and Beckers, J.M., 1999: Numerical simulations of seasonal and interannual variability of the Black Sea thermohaline circulation. *Journal of Marine Systems*, **22**, 241-267.
- Stanev, E.V., and Staneva, J.V., 2001: The sensitivity of the heat exchange at sea surface to meso and sub-basin scale eddies, Model study for the Black Sea. *Dynamics Atmospheres And Oceans*, **33**, 163-189.
- Stanev, E.V., Le Traon, P.Y., and Peneva, E.L., 2000: Sea level variations and their dependency on meteorological and hydrological forcing: analysis of altimeter and surface data for the Black Sea. *Journal of Geophysical Research*, **105 (C7)**, 17203-17216.
- Stanev, E.V., Roussenov, V.M., Rachev, N.H., and Staneva, J.V., 1995: Sea response to atmospheric variability, Model study for the Black Sea. *Journal of Marine Systems*, **6**, 241-267.
- Sur, H.I., Ozsoy, E., and Unluata, U., 1994: Boundary current instabilities, upwelling, shelf mixing and eutrophication processes in the Black Sea. *Progress in Oceanography*, **33**, 249-302.

- Telszewski, M., Chazottes, A., Schuster, U., Watson, A.J., Moulin, C., Bakker, D.C.E., Gonzalez-Davila, M., Johannessen, T., Kortzinger, A., Luger, H., Olsen, A., Omar, A., Padin, X.A., Rios, A.F., Steinhoff, T., Santana-Casiano, M., Wallace, D.W.R., and Wanninkhof, R., 2009: Estimating the monthly pCO₂ distribution in the North Atlantic using a self-organizing neural network. *Biogeosciences*, **6**, 1405-1421, ISSN: 1726-4170.
- Ulger, F., 2006: Euro-Atlantic Strategy for the Black Sea Region. *Yale J. Int'l Aff.*, **2**, 57.
- Vedernikov, V.I., and Demidov, A.B., 1993: Primary production and chlorophyll in deep regions of the Black Sea (English Translation). *Oceanology*, **33** (2), 193-199.
- Vesanto, J., Himberg, J., Alhoniemi, E., and Parhankangas, J., 2000: SOM toolbox for Matlab 5. Helsinki, Finland: Helsinki University of Technology.
- Yacoub, M., Badran, F., and Thiria, S., 2001: A topological hierarchical clustering: Application to ocean color classification. In Artificial Neural Networks — ICANN 2001, *Lecture Notes in Computer Science*, **2130**, 492-499, ISSN: 0302-9743.
- Yilmaz, A.O., Yunev, O.A., Vedernikov, V.I., Moncheva, S., Bologa, A.S., Cociasu, A., and Ediger, D., 1998: Unusual temporal variations in the spatial distribution of chlorophyll a in the Black Sea during 1990-1996. In: Ivanov, L.I. and Oguz, T. (Eds.), Ecosystem Mod, Kopelevich et al., *Journal of Marine Systems*, **36** (2002), 145-160, *Modeling as a Management Tool for the Black Sea*, **1**, 105-120.
- Yunev, O.A., Burlakova, Z.P., Krupatkina, D.K., Berseneva, G.P., and Churilova, T.Y., 1987: Seasonal variability of chlorophyll in the western Black Sea surface layer, The Sea Remote Sensing Taking Into Account of Atmosphere (in Russian). *Program of Intercosmos*, **2**, Part 2, 181-197.
- Yunev, O.A., Vedernikov, V.I., Basturk, O., Yilmaz, A., Kideys, A.E., Moncheva, S., and Konovalov, S.K., 2002: Long-term variations of surface chlorophyll a and primary production levels in the open Black Sea, Changes of the pelagic ecosystem over the last three to four decades. *Mar. Ecol. Prog. Ser.*, **230**, 11-28.
- Zatsepin, A.G., Ginzburg, A.I., Kostianoy, A.G., Kremenetskiy, V.V., Krivosheya, V.G., Stanichny, S.V., and Poulain, P.M., 2003: Observations of Black Sea mesoscale eddies and associated horizontal mixing. *Journal of Geophysical Research*, **108** (C8), 3246.

INITIAL DISTRIBUTION LIST

1. Defense Technical Information Center
Ft. Belvoir, Virginia
2. Dudley Knox Library
Naval Postgraduate School
Monterey, California
3. Professor Peter C. Chu
Chairman of Oceanography
Naval Postgraduate School
Monterey, California
4. Doctor Ming-Jer Huang
Deputy Director, Costal Water and Environment Center
College of Ocean Engineering
National Kaohsiung Marine University
Taiwan R.O.C.
5. Deniz Harp Okulu Kutuphanesi
Deniz Harp Okulu Komutanligi
Tuzla, Istanbul, Turkey (TURKIYE)
6. Istanbul Teknik Universitesi
Ayazaga Kampusu Fen Bilimleri Enstitusu
Maslak, Istanbul, Turkey (TURKIYE)
7. Emre Gulher
Seyir, Hidrografi ve Osinagrafi Dairesi Baskanligi
Cubuklu, Istanbul, Turkey (TURKIYE)